REAL-TIME MULTIMODAL SENSING IN NANO/BIO ENVIRONMENT

By

Bo Song

A DISSERTATION

Submitted to
Michigan State University
in partial fulfillment of the requirements
for the degree of

Electrical Engineering - Doctor of Philosophy

2016

ABSTRACT

REAL-TIME MULTIMODAL SENSING IN NANO/BIO ENVIRONMENT

By

Bo Song

As a sensing device in nano-scale, scanning probe microscopy (SPM) is a powerful tool for exploring nano world. Nevertheless two fundamental problems tackle the development and application of SPM based imaging and measurement: slow imaging/measurement speed and inaccuracy of motion or position control. Usually, SPM imaging/properties measuring speed is too slow to capture a dynamic observation on sample surface. In addition, Both SPM imaging and properties measurement always experience positioning inaccuracy problems caused by hysteresis and creep of the piezo scanner. This dissertation will try to solve these issues and proposed a SPM based real-time multimodal sensing system which can be used in nano/bio environment. First, a compressive sensing based video rate fast SPM imaging system is shown as an efficient method to dynamically capture the sample surface change with the imaging speed 1.5 frame/s with the scan size of 500 nm×500 nm. Besides topography imaging, a new additional modal of SPM: vibration mode, will be introduced, and it is developed by us to investigate the subsurface mechanical properties of the elastic sample such as cells and bacteria. A followed up study of enzymatic hydrolysis will demonstrate the ability of in situ observation of single molecule event using video rate SPM. After that we will introduce another modal of this SPM sensing system: accurate electrical properties measurement. In this electrical properties measurement mode, a compressive feedbacks based non-vector space control approach is proposed in order to improve the accuracy of SPM based nanomanipulations. Instead of sensors, the local images are used as both the input and feedback of a non-vector space closed-loop controller. A followed up study will

also be introduced to shown the important role of non-vector space control in the study of conductivity distribution of multi-wall carbon nanotubes. At the end of this dissertation, some future work will be also proposed to fulfill the development and validation of this real-time multimodal sensing system.

ACKNOWLEDGMENTS

I would like to express my most sincere appreciation to my advisor, Dr. Ning Xi, and Dr. Lixin Dong for their expert guidance, generous encouragement and support for my research.

In addition, I would like to thank all my PhD committee members: Dr. Hassan K. Khalil, Dr. Donna H. Wang and Dr. Xiaobo Tan. They offered me timely help and unfailing support that improve the technical soundness and the presentation of this dissertation.

Furthermore, I would like to express my gratitude to all my colleagues, especially to Dr. King Wai Chiu Lai, Dr. Carmen Kar Man Fung, Dr. Hongzhi Chen, Dr. Ruiguo Yang, Mr. Zhiyong Sun, Mr. Liangliang Chen, Mr. Andy Tomaswick, Dr. Yongliang Yang, Dr. Jianguo Zhao, and Dr. Yunyi Jia, for their support in the experiments and discussion.

Last but not the least, I want to thank my wife Lin Ren, my daughter Meeya Song and my parents. This dissertation would not have been possible without their years of encouragement and continuous support. With love and gratitude, I dedicate this dissertation to them.

TABLE OF CONTENTS

LIST OF FIGURES

Chapter 1

Introduction

1.1 Background and Motivation

The nano world was revolutionized the recent advancement of technology, enabling imaging, manipulation and measurement from nano and molecular level. Targeted nano particle imaging and sensing have introduced nanotechnology to the biomedicine, material science and physics studies. The laboratory-level testing and experiment of nano scale requires instruments that can provide nanoscale imaging and operation. As one of the centerpieces in nanotechnology, The scanning probe microscopy (SPM) is a suitable candidate for such needs as it could scan and manipulate nano particles or single molecular at nano scale. The scanning probe microscopies (SPMs) such as atomic force microscopy (AFM) and scanning tunneling microscopy (STM) have been frequently used to image and manipulate nano matters [1][2]. Usually this kind of microscopy are equipped with a probe which has a very sharp tip (tip apex is approximately 10 nm or less) and it can delicately scan on top of sample surface to get the topography image. Besides imaging, the sharp tip can be considered as an end effector of nano-robot which is capable of manipulating nano-objects and modifying sample surfaces [3][4].

Although AFM has many advantages in imaging, it still has a very significant negative point and that is the slow imaging speed. This is due to the working principle of AFM. Unlike other micro and nano level observer such as Scanning Electron Microscope (SEM),

AFM obtains the images by scanning line by line on the surface of sample. Usually it takes several minutes to scan hundreds lines to generate a high resolution image. Therefore the frame rate is about ten frames per hour. However, with the development of biology and physic, more and more researchers have the willing to observe the dynamic change in sample such as the deformation change of cell, DNA shape change and so forth [5] [6]. Although there are other available observations such as SEM which may also be used in many experiments, it demands the vacuum working environment which would make the live samples such as cell dead. AFM has the nature ability to work in a vacuum free condition, but the issue is the low imaging frame rate. Therefore, there is an increasing demands on the AFM based fast imaging system that could observe the continually change happens in seconds.

Besides imaging AFM also plays an important role of providing accurate topography image and near-filed mechanical properties measurement in the nanoscale. AFM enables the biomedical studies have a tremendous development from bull experiment to single molecule studies. Mechanical properties of single cell have been known as an important indicator or reporter to estimate or predict the state of the cells. Numerous methods have been introduced to obtain sample properties such as elasticity, viscosity and energy dissipation [7][8][9].

Regularly, the contact mode in AFM is also used as the indentation measurement in the "force curve function". During this measurement, a well controlled indentation is generated by AFM probe, and the tip-sample interaction force is recorded through the PSD sensor. Through the calculation based on Hertz model, an effective Young's modules can be estimate as the mechanical properties of the measured martial. Since mechanically indentation is necessary in this mode, the mechanical damage may happen during the measurement process. In addition, because the tip-sample indentation only emphasize the near-filed properties of the material, the internal mechanical properties are out of scope during the traditional force-

curve measurement. This may not be a serious issue for homogenous material, however, for biological samples such as cell and bacterial, the internal structures are quite complicated, and the near-filed properties is very likely to be significant different with the internal ones. Therefore, a and noninvasive mechanical mechanical properties measurement method is needed to efficiently map the mechanical properties of samples.

Besides imaging speed, conventional scanning probe microscopy (SPM) based nanomanipulations always have to face scanner accuracy problems such as hysteresis, nonlinearity and thermal drift. Although some scanners consist of internal position sensors, the sensitivity is not high enough to monitor high resolution nanomanipulations. Additionally, once the scan size decreases to nano level such as less than 100 nm, the noise brought by sensors is large enough to affect the performance of the closed-loop motion control system.

In this study, we proposed a novel sensing method in nano/bio environment for AFM (which is one of most useful SPMs with atomic resolution imaging and manipulating abilities) based fast imaging and electrical/mechanical properties measurement [3][4], which aims to provide the operator with video rate visualization information about sample surface changes in molecular level, as well as the ability to precisely characterize surface properties with high spatial accuracy. Through this multimodal system, AFM could serve as a multi-functional nanomanipulation system. It has many applications such as nano-surgery on a live cell [2], nano-device fabrication [10][11][12], fast imaging on dynamic change [13], and so forth.

1.1.1 Video Rate Imaging System

In 1993, the scan speed limit of AFM was described [14]. Although we found no publications, some studies aiming at increasing the AFM scan speed must have been initiated at least before 1995. In fact, we started to develop high-speed scanners in 1994 and small cantilevers

in 1997. Hansmas group also started to develop devises for high-speed AFM around 1995. They presented the first report on short cantilevers (23 m by 12m) in 1996 [15] and then a report on fast imaging in 1999, in which small cantilevers and an optical deflection detector designed for the small cantilevers were used to take a DNA image in 1.7 s. Next year, they imaged the formation and dissociation of the GroES-GroEL complexes [16]. However, due to the limited feedback bandwidth, this molecular process was traced by scanning the sample stage only in the x and z directions. A more complete high-speed AFM system was reported by us in 2001 and 2002 [17], in which a high-speed scanner and fast electronics were introduced in addition to small cantilevers (resonant frequencies 600 kHz in water) and an optical deflection detector for the small cantilevers. The imaging rate of 12.5 frames/s was achieved and therefore the swinging lever-arm motion of myosin V molecules was filmed as successive images with a scan range of 240 nm. This study inspired the study on high-speed AFM and seemed to bring about a groundswell towards the full-scale development of high-speed AFM and its application to biological issues that were difficult to solve by other techniques.

Devices for High-speed AFM

A. Small Cantilevers:

For a given spring constant, the resonant frequency increases with decreasing mass of the cantilever. The total thermal noise depends only on the spring constant and the temperature. Therefore, a cantilever with a higher resonant frequency has a lower noise density. In tapping mode, the frequency region used for imaging is the imaging bandwidth (its maximum is the feedback bandwidth) centered around the resonant frequency. Thus, a cantilever with a higher resonant frequency is less affected by thermal noise.

B. High-speed Scanner:

The scanner is the device most difficult to optimize for high-speed scanning. High-speed scan of mechanical devices with macroscopic dimensions tends to produce unwanted vibrations. Three techniques are required to minimize unwanted vibrations; (a) a technique to suppress the impulsive forces that are produced by quick displacement of the actuators, (b) a technique to increase the resonant frequencies.

The first issue was solved by a counterbalancing technique [17]. For example, for the z-scanner that moves at much higher frequencies than the x and y-scanners, two identical piezoactuators are placed to their supporting base in the counter directions and displaced simultaneously with the same length. An alternative way is to support a piezoactuator at both the ends with flexures. This way was applied to the x-scanner and worked very well (unpublished data).

The resonant frequency of a piezoactuator is determined almost solely by its maximum displacement (in other words, by its length). However, it can be effectively extended by an inverse compensation method as described later. The structural resonant frequency is enhanced by the use of a compact structure and a material that has a large ratio of the Youngs modulus to the density. However, a compact structure tends to produce interferences between the three-scan axes. A ball-guide stage [18] is one choice to avoid the interferences. An alternative way is to use flexures (blade springs) that are flexible enough to be displaced but stiff enough in the directions perpendicular to the displacement axis [19]. It should be noted that the scanner mechanics except for piezoacutators has to be produced by monolithic processing in order to minimize the number of resonant elements. An asymmetrical x-y configuration has been employed to gain a high resonant frequency for the x-scanner (the fast scan direction) [20]. However, a symmetrical x-y configuration has an advantage of being capable of rotating the scan direction [19]. As a material for the scanner, aluminum

or duralumin is often used.

1.1.2 Sensing of Electrical Properties in Nano Environment with Accurate Position Control

With the development of synthesis techniques of nano-materials, including nanotubs and nanowire [21], nanopolymers [22], quantum wells and quantum dots [23], the electrical characterization of these materials, albeit more challenging, attracted strong attention. Nano-materials have unique electrical properties due to quantum confinement. Not only do the electrical characterizations reveal the underlying physical, mechanical, and electrical properties of the nano-materials, but they can also be utilized to fabricate high performance sensors and devices, such as field effect transistors (FETs) [24][25], infrared sensors [26], gas sensors [27], and solar cells [28].

The conventional electrical characterization setup for nanotubes was measuring global resistance by connecting a nanotube to two metals [29]. However, such a setup is only capable to measure the overall resistance of the devices, which cannot distinguish the conductance of contacts and nano-materials. What is more, it lacks the capability to investigate the local conductance, which reflects underlying properties of the nano-materials.

SPMs, conventional imaging tools with nanometer-resolution, have been proposed to study the local conductance of nano-materials. They employed the conductive SPM probe as a movable electrode to conduct local conductance measurements [30][31][32][21]. Despite the feasibility of this measurement technique, only a few attempts have been implemented, let alone the low reliability and resolution. The reason is the difficulties in accurate SPM tip motion and force control during the measurement.

Although the imaging precision with SPMs can be up to subnanometer [33], it is challenging, if not impossible, to achieve such a precision for nanoscale motion control due to the spatial uncertainty of the probe's tip [34]. The main reason for such a deficiency is the piezoelectric actuation method for SPM systems. The inherent nonlinearities of piezo actuators such as hysteresis, creep, vibration, and thermal drift make precise position control (in the nanometer) extremely difficult [35]. Additionally, the modeling errors include parameter variation, unmodeled dynamics, and coupling effects also exert extra difficulties in position control [36].

The accurate point-to-point position control or motion control in nanoscale is a critical requirement for SPM based nanomanipulations because they rely on precisely moving the probe tip from one position to a desired position. For example, in AFM based nano-sensor fabrication, carbon nanotubes were pushed to a desired position by a nano-manipulator to form photodetectors [37]. The position accuracy of the manipulation should be within sub-10-nanometers to facilitate the integration to a nano-antenna that has a gap of 30 nanometers [38, 39].

The accuracy of AFM measurement and manipulation highly depends on accurate motion control of the probe (which is equipped at the end of the piezo-tube scanner). The piezo-tube scanner with advantages of nanometer scale resolution, high stiffness, and fast response, has been widely used in nano-manipulation field to control the relative position between the probe and samples. Nevertheless, the significant drawbacks affecting the precision of piezo actuators are the inherent hysteresis, creep and system drift characteristics [40]. The creep can affect the magnitude of the output of the actuators which can be compensated by the linear method. The hysteresis problem is a nonlinear one which can cause serious position error during nanomanipulation. The hysteresis problem might be sustainable for

AFM imaging with a fixed scan pattern. However, it is fatal for AFM based arbitrary manipulation.

To date, the hysteresis and creep problems in piezo actuators have been studied by many researchers, and various solutions have been proposed. Typical compensation model such as the Preisach method [41][42] which include a feed-forward controller for solving hysteresis problem. It cannot, however, reduce the on-line error because of lacking feedback. A Preisach operator based hysteresis compensator was developed with an indirect feed-back adaptive controller in order to reduce the positioning error in AFM imaging system [43]; a control strategy which integrates the Kalman observer as well as a vibration compensator with the LQG controller was proposed to alleviate the hysteresis, creep, vibration and cross coupling [44]. These methods above belong to the category of feedback controllers, which were designed to use sensors to capture the real-time output information of the system. Based on the information, specific control strategies can be developed to achieve precise motion positioning during nanomanipulations. However, the precision of the closed-loop scanner has been limited by the performance of these sensors (such as strain gauge [45], capacitive sensor [46], and optical sensor [47]). For sensors, high accuracy and bandwidth usually make them expensive and bulky. Moreover, integrated sensors are highly sensitive to noises [48]. This is the reason why high resolution AFMs are usually equipped with open-loop piezo tube scanners.

They have several drawbacks needed to be solved. First, sensors usually increase the system noise. Second, the displacement measured by sensors is the output of piezo-tube which is not the exact position of the tip (at the end of probe), because the cantilever of probe might be bending during nanomanipulations.

Different from the traditional approaches, we propose an image based closed-loop control

method to address the nanoscale motion control problem. The tip can be considered as a single pixel camera with two translational degree of freedoms. By moving the tip locally in a small area, a local scan image can be obtained [49]. Since the image is obtained from the local scan, it can accurately reflect the tip's true position. If a desired local scan image around a desired tip position is given, then a controller can be designed to steer the tip position to the desired position based on the image feedback. The advantage of such an image-based control method is that it eliminates external sensors for position feedback.

The image based control method presented in this research belongs to the literature of visual servoing, which utilizes vision information to control the motion of a mechanical system. For traditional image based visual servoing methods, prominent features are first extracted from the image, and then a controller is designed to make the vector of feature positions converge to a desired value [50]. Two possible issues associate with this feature based vector control method. On the one hand, robust feature extraction and tracking are difficult in natural environments. In fact, most visual servoing experiments are based on artificial fiducial markers [51]. On the other hand, feature extraction suffers from information loss because only the feature information is used for control.

Recently, the direct or featureless visual servoing method is proposed to address the above two issues. For such methods, the feature extraction and tracking are eliminated because the controllers are designed directly based on all the image intensities instead of some features extracted from the image. Three variations exist for such direct servoing methods. The first variation processes the original image with a spatial sampling function to derive a kernel measurement. A controller is designed to make the measurement error converge to zero [52]. The second variation forms the error as the sum-of-squared-difference of intensities between two images, and then makes this error approach zero [53, 54]. The third variation employs

an information theoretical approach to compare the distribution of the information between two images and design the control law to maximize the mutual information [55].

In such a condition, the experimental results of local conductance measurement from previous studies showed a large measurement variance [32][21], and this was possibly due to inaccurate tip position control which means during the measurement, the conductive probe may not reach the desired measurement points. Next, the spatial resolution of measurement (typical 100 nm in traditional measurement methods) is not fine enough to investigate local electric properties in nano scale [31]. Additionally, contact resistance between conductive probe and nanowires is load-dependent [30]. In other words, in order to characterize the local conductance uniformly at each location, constant contact force should be maintained which is another difficulty in practice. The non-vector space control strategy has the potential to overcome these difficulties by improving the spatial resolution of probe motion control through which the position error can be controlled within several nanometers. In addition, contact force between conductive probe and sample surface can be controlled by the force feedback system [56] and that ensures the constant contact resistance between the probe and sample. Therefore, the non-vector space control system has the potential to conduct delicate and complicated manipulation and measurement. In this study, we illustrate the efficiency of the non-vector control strategy by integrating the nanomanipulation with electrical characterization system to study local electrical property of a carbon nanotube.

1.1.3 Near-filed Surface Mechanical Properties Characterization using AFM

Morphological and mechanical properties analysis in nanoscale of cell is becoming increasingly important in various biomedical studies. Differences in topography and stiffness between normal and malign cells were found and established as a marker for the change in metastatic potential. The changes in cellular stiffness and morphology also reveals the different status of cell migration, which benefits the studies of the progression of various diseases including cancer, atherosclerosis and arthritis.

To date, it has been extremely challenging to study the morphology of cells by standard light microscopy in living cells because of their small size and complex structure. While immunofluorescence and electron microscopy have provided insight into the fine structure of cell adhesion molecules, a model system for addressing dynamic changes due to physiological mechanisms has been lacking. AFM offers the advantage of requiring minimal sample preparation, so that biomolecular structures can be directly studied in situ on viable samples that recapitulate biological conditions. AFM provides three-dimensional images of surface topography and quantitative measures of biological properties (e.g. stiffness) in unparalleled resolution allowing for the illumination of structural modifications after antibody treatment at a scale that cannot be revealed by standard light microscopy.

Regular contact mode and non-contact mode provide topography images, and non-contact mode is also used as the indentation measurement in the "force curve function". During this measurement, a well controlled indentation is generated by AFM probe, and the tip-sample interaction force is recorded through the psd sensor. Through the calculation based on Hertz model, an effective Young's modules can be estimate as the mechanical prop-

erties of the measured martial. Since mechanically indentation is necessary in this mode, the mechanical damage may happen during the measurement process. In addition, because the tip-sample indentation only emphasize the near-filed properties of the material, the internal mechanical properties are out of scope during the traditional force-curve measurement. This may not be a serious issue for homogenous material, however, for biological samples such as cell and bacterial, the internal structures are quite complicated, and the near-filed properties is very likely to be significant different with the internal ones. Recent development of ultrasonic AFM (UAFM) seems provide an alternative way to solve this issue. The UAFM is a modification of the original AFM set-up working in contact mode and constant normal force [57]. The main idea is to work at frequencies far above the cantilever primary resonance in the inertial regime of an AFM cantilever and sense the nonlinearity of the tipsurface interaction. In preliminary studies, UFM has already demonstrated sensitivity to surface elastic properties of stiff materials and also to subsurface defects [58].

UFM is based on a standard AFM operating in CM with the additional application of an ultrasonic vibration to the substrate, well above the AFM cantilever resonance. In this way, the friction force can be eliminated because the tip-sample contact is broken several times while the tip is laterally moved during the imaging process. Any possible damage to the sample or the tip is thus minimized [59]. Another alternative method to measure the internal structure of samples is using quartz crystal microbalance (QCM). QCM is a nanogram sensitive technique that utilizes acoustic waves generated by oscillating a piezoelectric, single crystal quartz plate to measure mass. The basis of QCM operation relates to quartz's inherent property of piezoelectricity. QCMs became widely used as mass balances only after the theory and experiments relating a frequency change of the oscillating crystal to the mass adsorbed on the surface was demonstrated by Sauerbrey in 1959 [60].

Liquid application of QCM technology expanded the number of potential applications dramatically including biotechnology applications and in particular biosensor applications. In practical biomolecular applications the dissipation parameter and the subsequently extracted viscoelastic parameters are critical for many applications. In cellular adsorption applications, the simple QCM frequency and Sauerbrey relationship would greatly underestimate the adsorbed mass of cells, since the shear wave of the oscillating quartz is dampened out before even reaching the middle of the cell. The frequency penetration depth (in the z direction away from the sensor surface) depends on the material in question and typically is on the order of 250 nm in water (rigid materials may strongly couple to the sensor surface and thus permit monitoring thicker films, but viscoelastic materials will be limited to within this range). When the adsorbed mass is viscous and sufficiently soft that it does not follow the sensor oscillation perfectly (such as in the case of cell adsorption), this leads to internal friction (due to the deformation) in the adlayer and thus to dissipation. This mass is the dynamic mass (incorporating associated water) and not the rest mass. The more viscous the adsorbate the more the oscillation will induce deformation, and thus the coupled mass will deviate more and more from the rest mass. Therefore, monitoring cell adsorption requires using the dissipation parameter to fully characterize the adsorption of a viscoelastic cellular structure. On the other hand, the adsorption of a small, rigid protein may be accurately measured by monitoring only frequency changes and fitting these to the Sauerbrey relation, although associated coupled water may again give an underestimation of the adsorbed mass. Although the QCM has the ability of monitoring mass/adhesion changes, the spatial detection is the main limitation of this technique which makes the quantitative analysis is impossible.

1.2 Objectives and Challenges

The objectives for this dissertation are to develop a multimodal AFM system with the ability of real-time sensing in nano/bio environment. The main challenges can be summarized in three aspects. First, in order to make the system have the function of fast imaging, a video-rate fast scan system is needed. The video-rate system should be able to work at the average frame rate of 1 frame/second, such that the rapid changes in biomedical samples can be captured in in situ observations. Second, The accuracy of the AFM tip motion and positioning should be well controlled within couple nanometers, which assure the accurate manipulation in nanoscale and molecular level. The last one is the function of subsurface imaging/mechanical properties mapping ability. Since most of reaction or interaction of molecules in biomedical study happens inside the cell or bacteria, there is an increasing demands on the AFM with the additional function of subsurface imaging and measurement other than regular topography imaging and near-filed surface mechanical properties characterization.

In order to meet the first challenge about the imaging speed, a compressive scanning is developed based on compressive sensing theory. The goal is to minimize scanning trajectory/time by eliminating unnecessary scanning. There are three major steps in applying compressive sensing to AFM imaging: to model an image for compressive sensing, to obtain compressive scanning pattern by a measurement matrix in compressive sensing, and to reconstruct original image based on compressive data.

For the second challenge, a non-vector space position control method is presented in this study. The general idea is to form a set from an image and formulate the image dynamics in the space of sets. This space is called the non-vector space because the linear structure

in the vector space does not exist. Based on the dynamics formulation, a controller can be designed directly on the image sets for visual servoing. This non-vector space control method is different from existing direct visual servoing methods because the problem formulation is different.

For the last challenge, we plan to use a special designed "vibration mode" AFM to solve the current issue of subsurface measurement. The vibration mode has a combination of the advantage of conventional tapping mode imaging with nanoscale resolution, and the nanomechanical mapping using the additional deformation induced by vibrating near the resonance frequency of the measured sample to recovery the spring constant map of the internal structure of the sample.

1.3 Contributions

The contributions for this thesis can be summarized in two aspects: design and development for real-time multimodal sensing system; followup application research to study the physics and mechanisms behind the physical and biomedical phenomenal using this system.

First, a compressive sensing based video rate fast AFM imaging system has been designed as an efficient method to dynamically capture the sample surface change with the imaging speed 1.5 frame/s. we proposed a concept called "compressive scan", in which the compressive sensing is used to compress the scan trajectory and reconstructed original AFM image frames. The video rate fast AFM imaging system does not require any hardware upgrades but also can achieve the high imaging speed with commercially fast scan AFM in the same level. A followed up study of enzymatic hydrolysis demonstrated the ability of in situ observation of single molecule event using video rate AFM. Second, a compressive

feedbacks based non-vector space control approach will be proposed in order to improve the accuracy of AFM based nanomanipulations. Instead of sensors, the local images are used as both the input and feedback of a non-vector space closed-loop controller. The position error of this non-vector space system can be controlled with in two nanometers. A followed up study will also be introduced to shown the important role of non-vector space control in the study of electrical breakdown of multi-wall carbon nanotubes. Moreover, a new additional function of the nanorobot: vibration mode, will be introduced. Different with conventional point and shooting signal measurement, vibration measurement is a more efficiency method to evaluate the mechanical properties of internal structure of elastic material. The basic idea of this method is to vibrate vertically using the AFM scanner to drive the measured sample vibrate up and down. The additional vibration amplitude on the upper surface of sample, other than the driving vibration can be considered as the result of sample deformation which depends on the mechanical properties, such as the spring constant. Vibration mode is potentially a useful AFM function to investigate the subsurface mechanical properties of the elastic sample such as cells and bacteria.

1.4 Outline of this Dissertation

The dissertation can be mainly divided into two aspects: system design and application study.

Chapter 2, 3 discuss the system design about video rate AFM and real-time sensing of electrical/mechnical properties; Chapter 4 and 5 present followup application research using this multimodal sensing system.

Chapter 2 presents the theoretical foundation of real-time imaging: compressive sensing.

The mathematical model of compressive sensing will be firstly discussed. After that, the design for the measurement matrix and scan trajectory will be elaborated. Then a knowledge based image recover algorithm to obtain the best reconstructed images. Finally, we present the implementation details and experimental results.

Chapter 3 introduces design and development of vibration mode AFM which is used for mechanical properties measurement in nano/bio environment. First of all, we will introduction of subsurface imaging and mechanical properties measurement. After that, a mathematic model of elastic object is discussed. Finally, we use compressive sensing to increase the sampling time to measure the subsurface mechanical properties map using vibration mode.

Chapter 4 discusses the follow-up study using video rate AFM to investigate single molecule behavior of enzymatic hydrolysis. First, in situ single molecule observation of cellulase using video-rate AFM is presented. Then, we perform in situ observation of cellulose surface changes as an indicator of hydrolysis rate. Finally, we plan to discuss the data and investigate the mechanism of enzymatic inactivation during hydrolysis interaction.

Chapter 5 introduces the real-time sensing method for electrical properties measurement in nano environment. First of all, a new technique named "non-vector space control" is proposed in order to increase the spatial positioning accuracy of AFM probing ability. After that a followed up study of carbon nanotube local electrical property characterization experiment is given to both validate the system and better understanding the mechanism of electron transport in multiwall carbon nanotube.

Chapter 6 concludes the main results and finding of this study and proposals the future work.

Chapter 2

Compressive Sensing for Real-time Sensing in Nano/Bio Environment

2.1 Introduction

Atomic Force Microscopy is a powerful instrument for studying and exploring nano world [61]. AFM can obtain ultra high resolution image in sub-nano scale. The basic working principle of AFM is accurately scanning line by line on the sample surface. AFM has an outstanding performance on imaging both in air and liquid. In addition, with the help of the AFM sharp tip, it could also be served as a measuring tool to measure the mechanical properties such as, Young's modulus and roughness [62] [63]. However, AFM has a very significant negative aspect-the slow imaging speed. It is due to the working principle of AFM. Usually it scans hundreds lines to generate a high resolution image. Therefore the frame rate is significantly low at five to ten frames per hour. This is impossible for dynamic observation in studying biological and physical behaviors such as the deformation and roughness change of cells, carbon nanotube shape change and so forth [5] [6]. In addition, for AFM based manipulations, the low frame rate make it difficult to realize a realtime visual guide manipulation system. Due to the low imaging speed, operators normally has to wait several minutes to visualize the manipulating results. Although some other microscopes such as SEM might also be used in many applications, they demand vacuum observation environment which is

not suitable for live samples such as cells. AFM naturally suits for working in a vacuum free condition, but the issue is the significant low imaging frame rate. Therefore, there is an increasing demands on fast imaging AFM system which could capture the continuously changes occurring in seconds.

In order to solve the problem of low frame rate, hardware upgrade is one possible option. Using uncoupled piezoactuators to drive the movement in each direction separately is one way to speed up the scan speed. Currently, a fast scan imaging AFM named Fastscan Dimension (Bruker Nano, Santa Barbara, CA) could reach as high as 3 frame per minute. For conventional AFM, hardware upgrade might not be an option, this is not only economic problem but the new scanners and controllers can not be directly implanted on a conventional AFM.

Another solution for imaging speed problem is not just gearing up the scan speed but also use novel scan strategy-compressive scan. For conventional AFM, the scanner scans the entire area for an image, but for compressive scan, a random scan pattern is delicately designed to achieve a shorter scan trajectory which decreases the time spent on scanning. Once the AFM gets the partial topography information, another issue is how to use this compressive data to reconstruct the original image.

Considering a compressible signal (image), there are some methods to directly sample the compressed data instead of the huge one with less information. Compressive sensing first came to solve this problem. In 2006, the fundamental mathematic proof for reconstructing sparse signal using fewer measurements had been established [64]. Compressive sensing realizes compressing in sampling step. Instead of sampling original signal point by point, compressive sensing only samples a sum of random projections from original signal to a projection matrix (measurement matrix). After a few measurements which are fewer

than traditional sampling method, the original signal can be reconstructed by signal reconstruction algorithm [65]. Because the number of measurements are fewer than the dimension of original signal, if the signal is sparse and the measurement matrix has been well selected, the compressive sensing could reconstruct the exact original signal with overwhelming probability.

For AFM based compressive scan, it largely decreases the time spent on scanning, and the reconstructed image is obtained after image recovering algorithms have been applied. In addition, in order to obtain a better reconstructed image with even less measurements, and realize AFM based dynamic observation, a special compressive scan based on previous knowledge is proposed. It could merge the information obtained by previous frame image and the compressive data obtained by current frame. This approach could largely increase the AFM imaging rate, enhance image quality and realize dynamic observation.

In this study, we propose a new approach for using compressive scan to achieve a fast imaging AFM. For this approach, there are four steps as follows: (1) Theoretical analysis of compressive scan based on compressive sensing. (2) Random measurement matrix design for AFM implementation. Because of the working principle of AFM, random measurement matrix can not be directly applied, the methodology to implement random measurement matrix into AFM scan trajectory will be discussed. (3) Image reconstruction algorithms investigation. Due to special designed measurement matrix, different image reconstruction methods will be discussed. (4) In order to dynamically capture continuous surface change, a knowledge based compressive scan strategy is developed for AFM dynamic observation.

2.2 Theoretical Foundation of Compressive Sensing

Introducing compressive sensing into AFM imaging system is a convenient and efficient way for reducing time spent on scanning. The goal is to decrease the scan trajectory which samples fewer than conventional measurements. There are three major sections in compressive sensing: signal sparse representation, measurement matrix design and signal reconstruction algorithms. Compressive sensing prefers the sparse signal. Although most signals are not sparse naturally, it is not difficult to find the efficient sparse representation methods. The transforms such as wavelet and Fourier have the ability to make signal sparse from time domain into frequency domain. In this section we will briefly introduce the basic idea of compressive sensing and the signal sparsify approaches. The design of measurement matrix and signal reconstruction algorithms will be discussed in next sections.

2.2.1 General Idea of Compressive Sensing

Given an unknown signal x which $x \in \mathbb{R}^N$, and use M times linear measurements to sample the original signal x (as shown in Fig.2.1). If $M = N$, the original signal x will be perfectly captured by solving the linear algebra equations. However, it becomes interesting when $M \ll N$, and in words fewer measurements might be enough for sampling and reconstructing the original signal.

$$y = \Phi x \tag{2.1}$$

where Φ is called measurement matrix. Every measurement is a sum of linear projection from the original signal x to measurement matrix Φ. y is the measurement results which $y \in \mathbb{R}^M$. Eq.(5.11) is obviously an under-determined equation. There is no unique solution

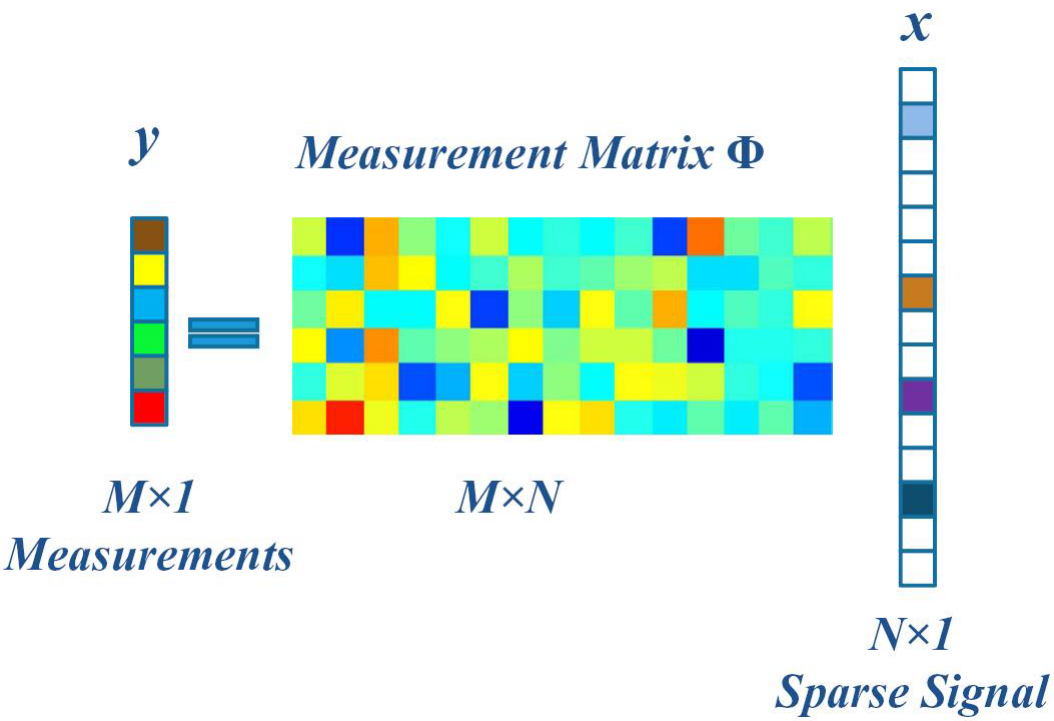

Figure 2.1 General idea of compressive sensing

for this equation. However if it is under some constraints such as that the original signal is sparse and measurement matrix is properly designed, we can find an optimization solution for x by solving the minimization l_0 problem [64].

$$\hat{x} = \arg\min ||x||_0 \quad \text{s.t.} \quad \Phi x = y \tag{2.2}$$

Since solving l_0+ minimization problem is a NP-hard question, people would like to use l_1 minimization instead[66]. Then the Eq.(5.12) could be modified as

$$\hat{x} = \arg\min ||x||_1 \quad \text{s.t.} \quad \Phi x = y \tag{2.3}$$

where $\hat{x}$ is the reconstructed signal.

2.2.2 Signal Sparse Representation

A signal is called sparse if only a small amount of elements have the significant value while all the others are zero. Hence K-sparse means the signal only has K significant values. One of the assumptions for the compressive sensing is that the observed signal must be sparse. Actually most signals are not sparse in time domain. Therefore we must find the signal sparse representation in other domains or basis such as

$$x = \Psi s \tag{2.4}$$

where s is the sparse representation of signal x in basis Ψ. Many transform basis such as wavelet, curvelet and Fourier have the ability to make signal sparse by transforming it from time domain to the frequency domain. Under these basis, Eq.(2.4) becomes

$$y = \Phi\Psi s \tag{2.5}$$

$$y = \tilde{\Phi} s \tag{2.6}$$

Now new measurement matrix can be considered as $\Phi\Psi$, and here we use $\tilde{\Phi} = \Phi\Psi$ to denote this new measurement matrix. Then under the same basis, Eq.(5.13) becomes

$$\hat{s} = \arg\min ||s||_1 \quad \text{s.t.} \quad \Phi\Psi s = y \tag{2.7}$$

where $\hat{s}$ is the coefficients under basis Ψ of the original signal. Obviously, the transform basis $\Psi = I$ if the original signal is already sparse.

Because compressive sensing could use fewer measurements to obtain a high quality recovery image, we are interested in integrating compressive sensing with AFM scanning strategy to decrease the time spent on scanning. The challenge of integration is how to design a proper measurement matrix. Usually random Gaussian and Bernoulli matrixes are good choices but the difficulty for applying these random measurement matrixes to AFM is that the AFM obtains the topography through scanning line by line. It is difficult to sample random points simultaneously. Therefore, special designed random measurement matrix implementation on AFM should be discussed.

2.3 Design of Measurement Matrix for Compressive Scanning in Real-time Sensing

For compressive sensing the measurement matrix is an essential part due to the relationship between the measurement matrix and measurement efficiency. Well and properly designed measurement matrix usually lead to fewer measurements but high quality reconstruction image. However the challenge in compressive sensing in AFM is how to implement measurement matrix onto AFM scan trajectory. The physical meaning of measurement matrix in this application is the AFM tip scanning trajectory. In other words, given a designed measurement matrix, the tip moving and scanning trajectory is also determined. Because of the special working principle of AFM which uses a sharp tip to scan on top of sample surface line by line, it is really hard to use conventional random measurement matrix which samples random points in the entire sample surface simultaneously. Instead of random measurement matrix, continue and smooth AFM trajectory represented by measurement matrix might be a better choice. Therefore some special designed measurement matrixes have been

studied in previous research [13]. Moreover, how to control the movement of AFM tip is another issue. Fortunately, the system we developed for AFM based nano-manipulation, has the ability to make AFM tip scan along designed measurement matrix and obtain the topography. During the test in previous study, although each one of these matrixes has a good performance on data sampling and image recovery for the AFM sample surface, one potential problem of these measurement matrixes is that none of them is random. From the view of the Restricted Isometry Property (RIP) [64], these measurement matrixes cannot guarantee all the information of original image to be totally reconstructed. In this section, we re-design the measurement matrix which is a random sampling matrix when it associates with Fourier or wavelet basis, it satisfies the conditions of RIP. The original image will be fully reconstructed.

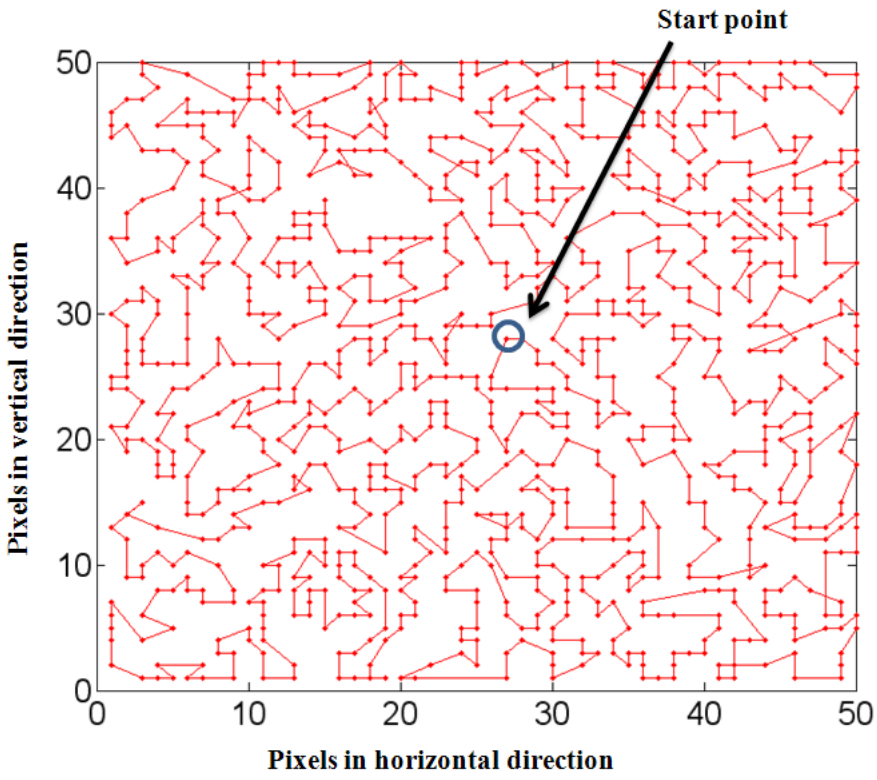

Figure 2.2 Random sampling points and TSP trajectory (800 random points in 50×50 points area with total travel distance 981.1645)

Given a measurement matrix, the scanning trajectory is also determined. In this research we prefer the random sampling in time domain (as shown in Fig. 2.2). However, the working principle of AFM is using a sharp tip to scan line by line on top of sample surface. Therefore a continuous trajectory which will cover all the random points should be developed. It is the typical traveling salesman problem (TSP) which is NP-hard. Before solving this problem, several conditions must be satisfied-AFM tip must scan each point exactly once and finally return to the starting point. Here we use Genetic Algorithm (GA) which is a popular computing paradigm based on crossover and mutation to find the near optimal solution for this trajectory [67]. This algorithm first connects each of the two points and then randomly chooses one position to cut the connection of two points. By using processes of recombination, mutation and selection, GA eventually searches a new generation points which is better (shorter distance) than its former trajectory. Here we set the imaging area with the size of 50×50 pixels and the final trajectory is shown in Fig. 2.2. The red line denotes the trajectory of AFM tip which would visit every point only once. The total distance is around 989 (the distance between two neighbor points is set as one) which is much shorter than conventional scan strategy (total distance is 2500 in raster scan). With shorter scan trajectory, we can directly save the time spent on scanning and increase the AFM imaging rate.

One important thing should be noted here, for compressive sensing, it has two basic constraints: first, the measurement matrix should satisfy the RIP condition; second, the observed signal should be sparse. For this application, neither of them could be satisfied. Good thing is we can find one basis Ψ which could transform the non-sparse signal in time domain into frequency domain (as mentioned in previous section). About the first constraint, once we apply the basis Ψ the new measurement matrix becomes $\tilde{\Phi} = \Phi\Psi$ which satisfies

the RIP and implies that we randomly sampled in time domain but reconstruct the image in frequency domain and finally transfer it back to time domain.

2.4 Knowledge based Compressive Sensing

In the previous section, we proposed the random measurement matrix design for compressive scan. Through the theoretical analysis, this sampling method could deal with the condition when the signal is sparse in frequency domain. If the signal is not sparse in frequency domain, in other words, if the observed image is sparse in time domain, this sampling method could not guarantee the observed image be well sampled and exactly reconstructed. Actually, for AFM based manipulations and observations, the observed image is quite possible to be sparse in time domain. According to uncertainty principle, If the signal is sparse in frequency domain, it can not be sparse at time domain. In this case the random sampling in time domain might not cover all the topography information.

One solution of this issue is to build up a knowledge based compressive scan strategy. In the dynamic observation, AFM continuously scans and observes the dynamic change of sample surface. In this case we can develop an approach to design the measurement matrix base on last frame information, and simultaneously use the information of last frame as a part of current measurements. Now, the problem becomes how to use the previous information and how to design the new measurement matrix for the current frame.

2.4.1 Knowledge based Measurement Matrix Design

For continuously observation, if the capture frequency is higher than nanoparticle dynamic change frequency, we can assume that the image in time t_i is similar with the previous one

t_{i-1}

$$\|x_{t_i} - x_{t_{i-1}}\|_2 \leq \gamma \tag{2.8}$$

where γ is a positive number. In this case, we can further assume that for current frame x_{t_i}, it consists of two parts among which one is from previous frame $x_{t_{i-1}}$ and the other one is from current sampling $\Phi_{t_i} x_{t_i}$.

$$x_{t_i} \approx \Phi_{t_{i-1}} x_{t_{i-1}} \oplus \Phi_{t_i} x_{t_i} = \bar{x_{t_i}} \tag{2.9}$$

where $\Phi_{t_{i-1}}$ and Φ_{t_i} are the measurement matrixes of $x_{t_{i-1}}$ and x_{t_i} respectively. In words, they could be considered as the projection matrixes which $\Phi_{t_i} \in \mathbb{R}^{M \times N} : \mathbb{R}^N \to \mathbb{R}^M$ and $\Phi_{t_{i-1}} \in \mathbb{R}^{(N-M) \times N} : \mathbb{R}^N \to \mathbb{R}^{(N-M)}$

In Eq.(2.9), $\Phi_{t_i} x_{t_i}$ is the random sampling results of current frame image. Because the length of this measurements is M which $M < N$, it still needs the information about the other $N - M$ elements information to construct current frame image. For these missing elements, we use previous frame information to fill in the blanks to generate $\bar{x_{t_i}}$.

However, this $\bar{x_{t_i}}$ could not be used directly as the current frame image, and this is because these two parts of data from different frames can not merge themselves automatically. Another compliant and predict process is needed for further estimating the current frame image $\bar{x_{t_i}}$. Here, the compressive sensing based on Bernoulli random measurement matrix and minimization total variation algorithm are used to estimate the $\bar{x_{t_i}}$.

2.4.2 Image Reconstruction

$$y_{t_i} = \Phi_{Bernoulli} \bar{x_{t_i}} \tag{2.10}$$

$$\hat{x_{t_i}} = \arg\min TV(\bar{x_{t_i}}) \quad \text{s.t.} \quad y_{t_i} = \Phi_{Bernoulli} \bar{x_{t_i}} \tag{2.11}$$

where $TV(x) = \sum_{i,j} \sqrt{(x_{i+1,j} - x_{i,j})^2 + (x_{i,j+1} - x_{i,j})^2}$.

After the further sampling and reconstruction process, the recovered current frame image $\hat{x_{t_i}}$ has been obtained. Because of applying the minimization total variation algorithm, the recovered image could achieve a gradient continuous. In this case the $\hat{x_{t_i}}$ could become sharp and smooth. Two important things should be noted here. First one is the physical meaning of $\hat{x_{t_i}}$. Here $\hat{x_{t_i}}$ is reconstructed by both the current frame x_{t_i} and previous frame $x_{t_{i-1}}$. Therefore, the recovered current frame image $\hat{x_{t_i}}$ represent the frame between t_{i-1} and t_i. Here we use this inter-frame to approximate the current frame image. Consider a dynamically continuous observation, assume that the first frame of image we have already got and through above approach we random sampled at time t_i, where $i = 1, 2, \cdots, n$ and recovered the images at the time $t_{i-\delta}$, where $i = 1, 2, \cdots, n$ and $\delta \subset (0, 1)$. The value of parameter δ depends on the number of random sampling. In other words, if random samples have N/2 measurements, the value of δ should around 0.5. Second one is about the random measurement matrixes $\Phi_{t_i} x_{t_i}$ and $\Phi_{Bernoulli}$. Both of them should be redesigned for each frame. These processes try to achieve an independent and uniform sampling which will cover the entire image across several frames.

2.5 System Implementation for SPM

In the previous sections, we proposed a knowledge based compressive scan approach for AFM dynamic imaging. This methodology is used for increasing the imaging speed of AFM in order to achieve a fast imaging system. By introducing compressive sensing, a compressive scan strategy has been developed. In order to deal with the small particles on sample surface which might be lost by random sampling, we build up a knowledge based compressive scan system which could reconstruct images better. In order to test the performance of compressive scan and knowledge based compressive scan strategies, several experiments were carried out to prove the ability of this fast imaging system.

In order to test the performance of compressive scan strategy, we implement this methodology into our AFM manipulation system (as shown in Fig. 2.3). An Multimode (Bruker Inc.) AFM with an open-loop scanner is used in this experiment. The nano-manipulation software is run on the main computer with a haptic joystick. In addition, a real-time Linux system (RT-Linux) with DAQ cards is used for control. We also developed a box named Signal Access and Control Box for applying the control signal into the AFM controller as well as reading the signal of topography of sample surface.

2.6 Experimental Testing Results

The samples we chose for these experiments are HaCaT cells and DNA. The HaCaT cell is a type of human skin cell. The HaCaT cells were grown in DMEM (Gibco-Invitrogen, Carlsbad, CA USA.) medium, and supplemented with ten percents fetal calf serum (Gemini Bio-products, Wesr Sacramento, CA USA.) [2]. DNA sample is made from Lambda Phage DNA, methylated, from Escherichia coil host strain W3110(Sigma-Aldrich.Co). DNA solution was

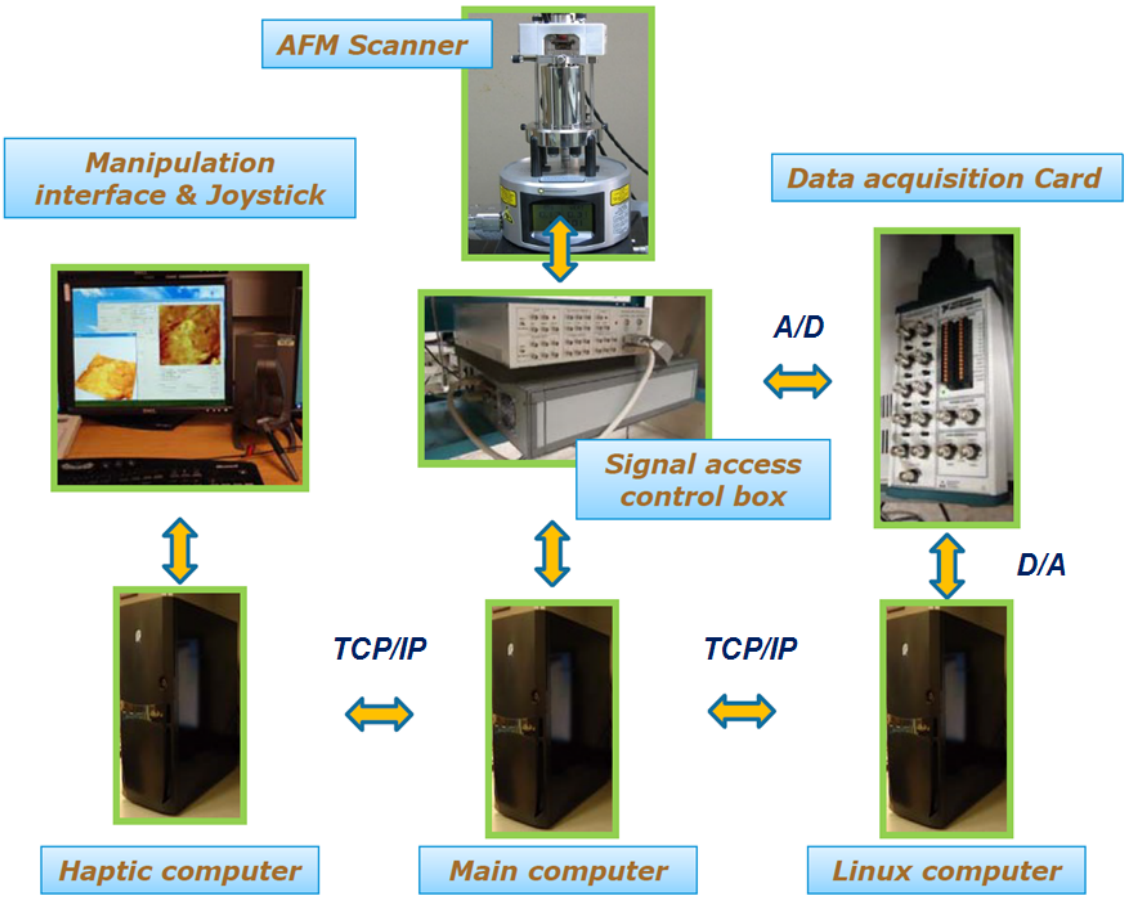

Figure 2.3 The hardware architecture of the nanomanipulation system

diluted into 1:1000 with DI water and drop on loosely bound mica surface.

2.6.1 Static Observation

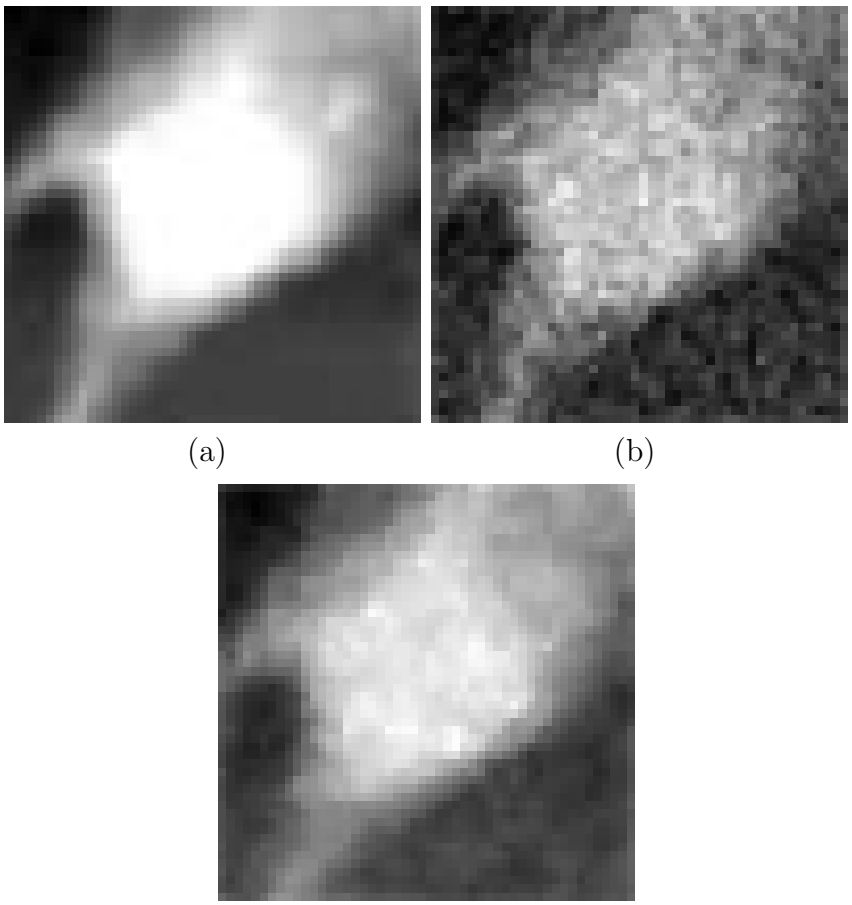

(a) (b)

(c)

Figure 2.4 Static compressive scan experiment results on HaCaT cells sample (50×50 pixels) (a): Original AFM image (scan size: $5\mu m \times 5\mu m$) (b): Reconstructed image by minimizing l_1 (c): Reconstructed image by minimizing total variance

Before compressive scan, we use conventional AFM to get a local image with the scan size of 5×5 μm on HaCaT cells (shown in Fig.2.4(a)). Firstly the AFM images were obtained for several minutes. Then in the same area, we use the compressive scan method to re-scan and use compressive sensing image reconstruction algorithms to recover the image. The recovered images are shown in Fig.2.4(b) and (c). The image reconstruction algorithms we

used here are l_1 as Eq.(2.7) the minimization total variation algorithm as Eq.(5.14).

For DNA sample, the scan size is 500 nm $\times$ 500 nm which is much smaller than previous experiment. This example tries to illustrate the imaging performance of compressive scan on very small area. The results are shown in Fig.2.5

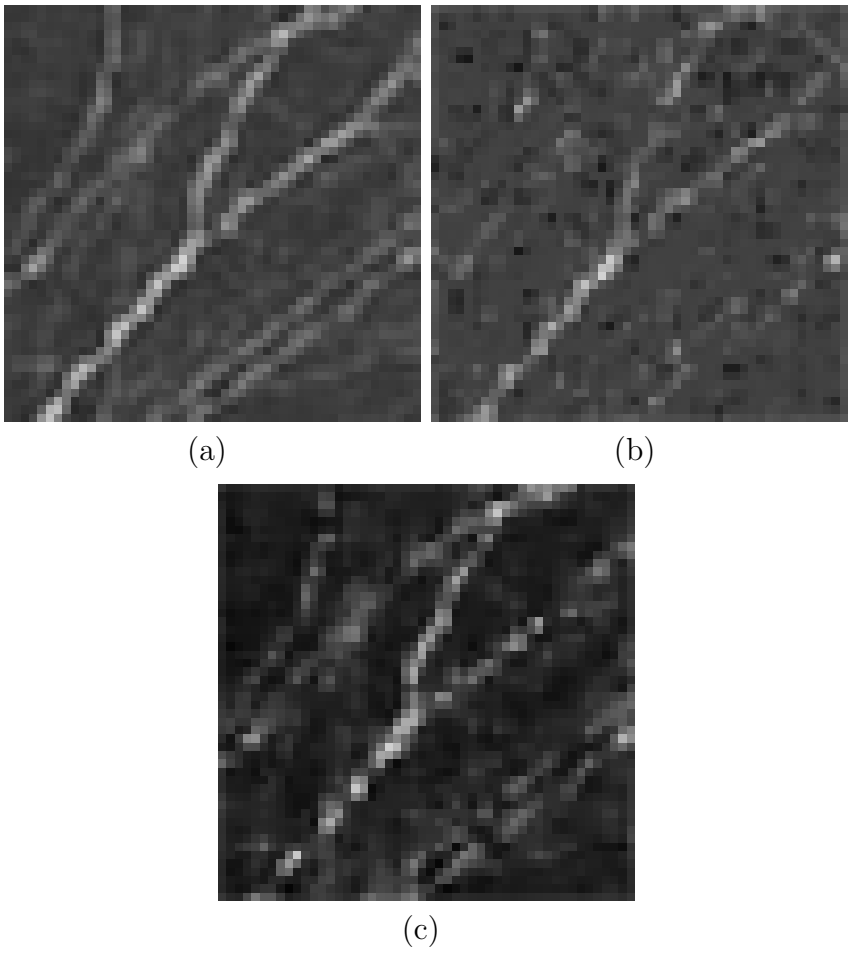

Figure 2.5 Static compressive scan experiment results on DNA sample (50×50 pixels) (a): Original AFM image (scan size: 500 nm×500 nm) (b): Reconstructed image by minimizing l_1 (c): Reconstructed image by minimizing total variance

From the static experiment results, it is clear to visualize the difference between these two samples. For the HaCaT cells images, both the image reconstruction algorithms have the good performance-both of them are similar to original image(as shown in Fig.2.4(a)). Although the l_1 algorithms seems not as good as the minimization total variation algorithm,

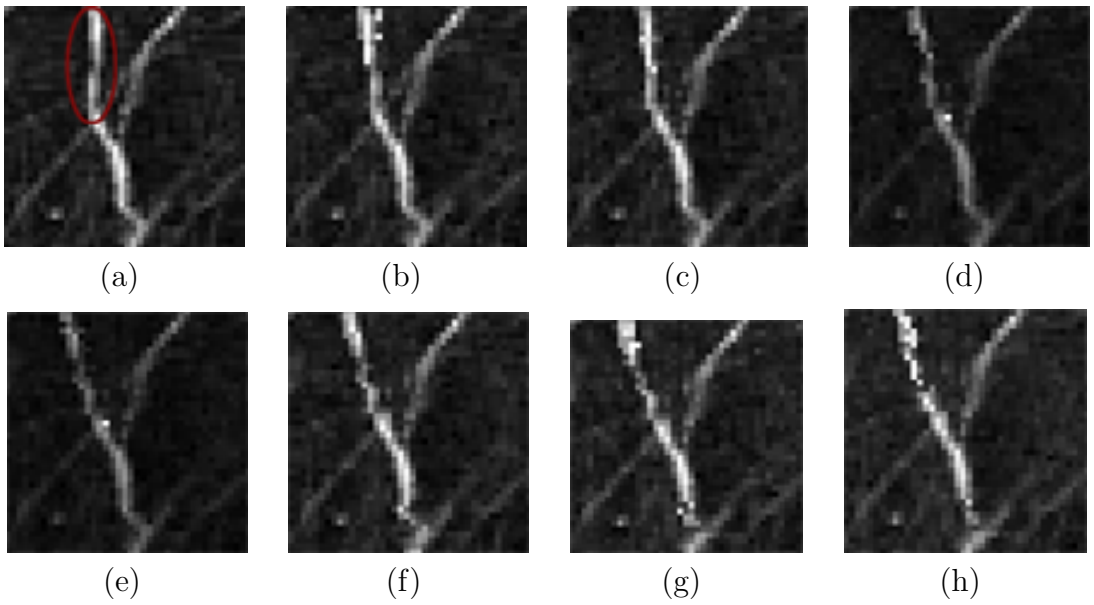

Figure 2.6 Dynamic observation of DNA on loosely bound surface using knowledge based compressive scan (50×50 pixels) (a): First frame image obtained by conventional scan (scan size: 800 nm×800 nm) (b)-(h): Reconstructed image obtained by knowledge based compressive scan with minimizing total variance

the reconstructed images are approximate to the original AFM image. Minimization total variation algorithm calculates the sparsest solution in gradient level and this is the reason why its images look more smooth. However, the DNA images (as shown in Fig.2.5) are quite different. Neither of these two image reconstruction algorithms could provide clear images. Both reconstructed images look like "partial images" which loss some information. Even if applying the minimization total variation algorithm, the image still could not become smooth. The reason for this phenomenon is the image spasifying problem.

As the discussion in previous sections, the compressive scan approach could deal with the sparse signal in frequency domain. For HaCaT cells example the image is sparse in frequency domain and after the sparsify basis-wavelet has been applied, the images could be well reconstructed. However, once applying the same process onto time domain sparse image-DNA example in this experiment, it did not work. This is because the DNA image is

not sparse in frequency domain, and the compressive scan failed to capture and reconstruct the entire images.

In order to solve this problem, we developed a knowledge based compressive scan strategy. This method can integrate the information of current frame image (got by compressive scan) and last frame image together to reconstruct a frame image which is close to current image.

2.6.2 Dynamic Observation using Knowledge based Compressive Scan

In this section, we validate our knowledge based compressive scan strategy for dynamic observation. In this experiment, we use AFM to continuously observe the dynamic change of DNA in liquid on loosely bound surface. First we get an local area AFM image with the scan size of 800 nm×800 nm (50×50 pixels). This image is set at the first frame. Then we use the compressive scan strategy to continuously scan this area and use the minimization total variation algorithm to reconstructed each frame. Note that, each frame is sampled and reconstructed by both its current frame information and its previous frame information. The experiment results are shown in Fig. 2.6 of which time interval between two neighbor frames is one second.

In this dynamic observation, the total capture time is seven seconds (one frame per second). Fig. 2.6(a) is the initial frame got by conventional scan mode which scan the entire area. From frame (b) to (h) the compressive scan has been applied to partial scan the area. In each frame the sampling ratio (the number of samples to the length of signal) is 0.3 which largely decrease the time spent on scanning. In this experiment, the moving speed of DNA is controlled by adjusting the concentration of ion in the imaging buffer. For knowledge

base compressive scan, one assumption is that the change or difference between two frames should be small just like conventional video frames. In order to satisfy this assumption, a proper DNA moving speed has been adjusted for this experiment. From this sequence of frames it is clear to see the dynamic moving of DNA. Comparing the image in Fig. 2.6 with the one in Fig. 2.5 which only uses compressive scan to sample and reconstruct image, the reconstructed image using knowledge one is much better and sharper than the one without previous knowledge.

2.7 Conclusions

In this study, a compressive scan based AFM imaging strategy is proposed for improving the AFM imaging speed to reach a high imaging frame rate. Through introducing compressive sensing, AFM scanner has the opportunity to avoid raster scan strategy which scans the entire area with hundreds of scan lines, and become a compressive scan which only randomly samples partial topography information. In addition, The entire image of partially scanned area could be well reconstructed. This compressive scan strategy prefers the sparse signal in frequency domain. However, if the image is sparse in time domain, this method might not work because of lost of detail information. In order to solve this problem, a previous knowledge based compressive scan is developed in this research. We designed a methodology to merge the information in last frame and partial information in current frame together to generate a frame which approximates to current frame in time domain. This approach could be directly applied onto the area of dynamic observation. For AFM application, the initial frame could be well scanned by conventional scan strategy to get a high resolution image. Then from second frame the compressive scan strategy could be applied to largely decrease

to time spent on scan. With the data got by compressive scan and the information in last frame an approximated current frame image could be well reconstructed. The results from static and dynamic experiments showed good performance on imaging with less scan time. This compressive scan strategy potentially could be applied to other scanning microscopies such as SEM, STM, and so forth.

Chapter 3

Sensing of Mechanical Properties in Nano/Bio Environment

3.1 Introduction

During recent several decades, AFM plays an important role of providing accurate topography image and near-filed mechanical properties measurement in the nanoscale. AFM enables the biomedical studies have a tremendous development from bull experiment to single molecule studies. Mechanical properties of single cell have been known as an important indicator or reporter to estimate or predict the state of the cells. Numerous methods have been introduced to obtain sample properties such as elasticity, viscosity and energy dissipation [7][8][9].

Regular contact mode and non-contact mode provide topography images, and non-contact mode is also used as the indentation measurement in the "force curve function". During this measurement, a well controlled indentation is generated by AFM probe, and the tip-sample interaction force is recorded through the psd sensor. Through the calculation based on Hertz model, an effective Young's modules can be estimate as the mechanical properties of the measured martial. Since mechanically indentation is necessary in this mode, the mechanical damage may happen during the measurement process. In addition, because the tip-sample indentation only emphasize the near-filed properties of the material, the internal

mechanical properties are out of scope during the traditional force-curve measurement. This may not be a serious issue for homogenous material, however, for biological samples such as cell and bacterial, the internal structures are quite complicated, and the near-filed properties is very likely to be significant different with the internal ones.

Recent development of ultrasonic AFM (UAFM) seems provide an alternative way to solve this issue. The UAFM is a modification of the original AFM set-up working in contact mode and constant normal force [57]. The main idea is to work at frequencies far above the cantilever primary resonance in the inertial regime of an AFM cantilever and sense the nonlinearity of the tipsurface interaction. In preliminary studies, UFM has already demonstrated sensitivity to surface elastic properties of stiff materials and also to subsurface defects [68][58].

UFM is based on a standard AFM operating in CM with the additional application of an ultrasonic vibration to the substrate, well above the AFM cantilever resonance. In this way, the friction force can be eliminated because the tip-sample contact is broken several times while the tip is laterally moved during the imaging process. Any possible damage to the sample or the tip is thus minimized [59].

Another alternative method to measure the internal structure of samples is using quartz crystal microbalance (QCM). QCM is a nanogram sensitive technique that utilizes acoustic waves generated by oscillating a piezoelectric, single crystal quartz plate to measure mass. The basis of QCM operation relates to quartz's inherent property of piezoelectricity. QCM-s became widely used as mass balances only after the theory and experiments relating a frequency change of the oscillating crystal to the mass adsorbed on the surface was demonstrated by Sauerbrey in 1959 [60]. Liquid application of QCM technology expanded the number of potential applications dramatically including biotechnology applications and in

particular biosensor applications.

In practical biomolecular applications the dissipation parameter and the subsequently extracted viscoelastic parameters are critical for many applications. In cellular adsorption applications, the simple QCM frequency and Sauerbrey relationship would greatly underestimate the adsorbed mass of cells, since the shear wave of the oscillating quartz is dampened out before even reaching the middle of the cell. The frequency penetration depth (in the z direction away from the sensor surface) depends on the material in question and typically is on the order of 250 nm in water (rigid materials may strongly couple to the sensor surface and thus permit monitoring thicker films, but viscoelastic materials will be limited to within this range). When the adsorbed mass is viscous and sufficiently soft that it does not follow the sensor oscillation perfectly (such as in the case of cell adsorption), this leads to internal friction (due to the deformation) in the adlayer and thus to dissipation. This mass is the dynamic mass (incorporating associated water) and not the rest mass. The more viscous the adsorbate the more the oscillation will induce deformation, and thus the coupled mass will deviate more and more from the rest mass. Therefore, monitoring cell adsorption requires using the dissipation parameter to fully characterize the adsorption of a viscoelastic cellular structure. On the other hand, the adsorption of a small, rigid protein may be accurately measured by monitoring only frequency changes and fitting these to the Sauerbrey relation, although associated coupled water may again give an underestimation of the adsorbed mass.

Although the QCM has the ability of monitoring mass/adhesion changes, the spatial detection is the main limitation of this technique which makes the quantitative analysis is impossible. In order to address these issues, we present a method called vibration mode for the study of internal mechanical properties of biomedical samples. The vibration mode has a combination of the advantage of conventional tapping mode imaging with nanoscale

resolution, and the nanomechanical mapping using the additional deformation induced by vibrating near the resonance frequency of the measured sample to recovery the spring constant map of the internal structure of the sample. One of the significance of this technology is the non-invasive measurement. The AFM tip is not mechanically touched with the sample surface, which assure the accuracy of the measurement by means of ruling out the affection by the tip-surface interactions which are the biggest issue for the nano-indentation measurement.

3.2 The State of Art of Vibration Model

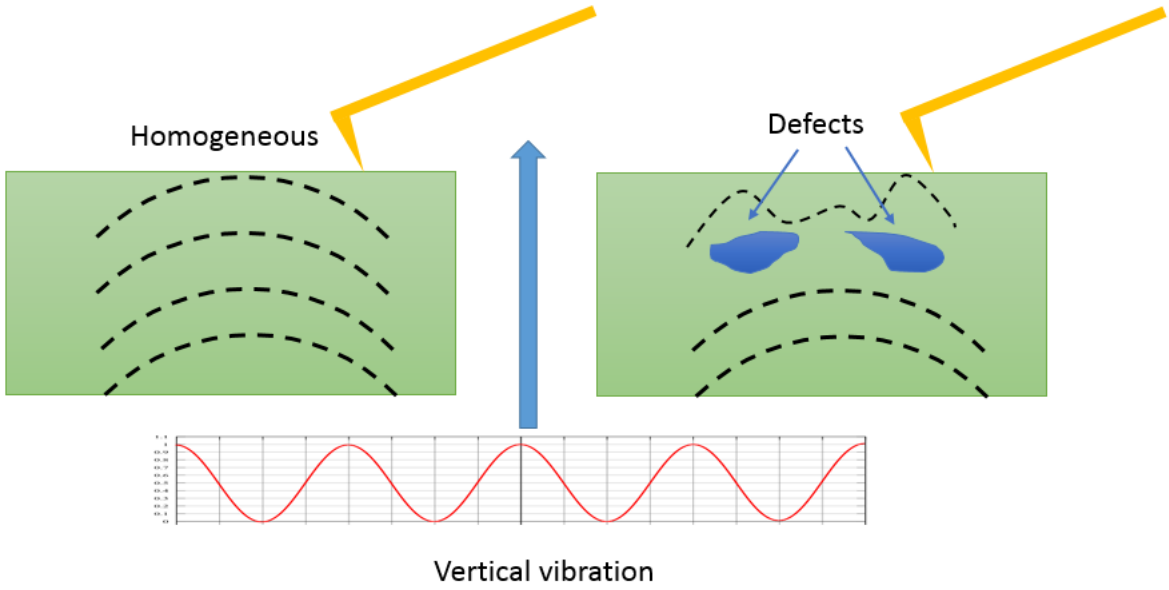

Figure 3.1 Schematic of the setup for the vibration AFM

Different with conventional point and shooting signal measurement, vibration measurement is a more efficiency method to evaluate the mechanical properties of internal structure of elastic material. The basic idea of this method is to vibrate vertically using the AFM scanner to drive the measured sample vibrate up and down. The additional vibration am-

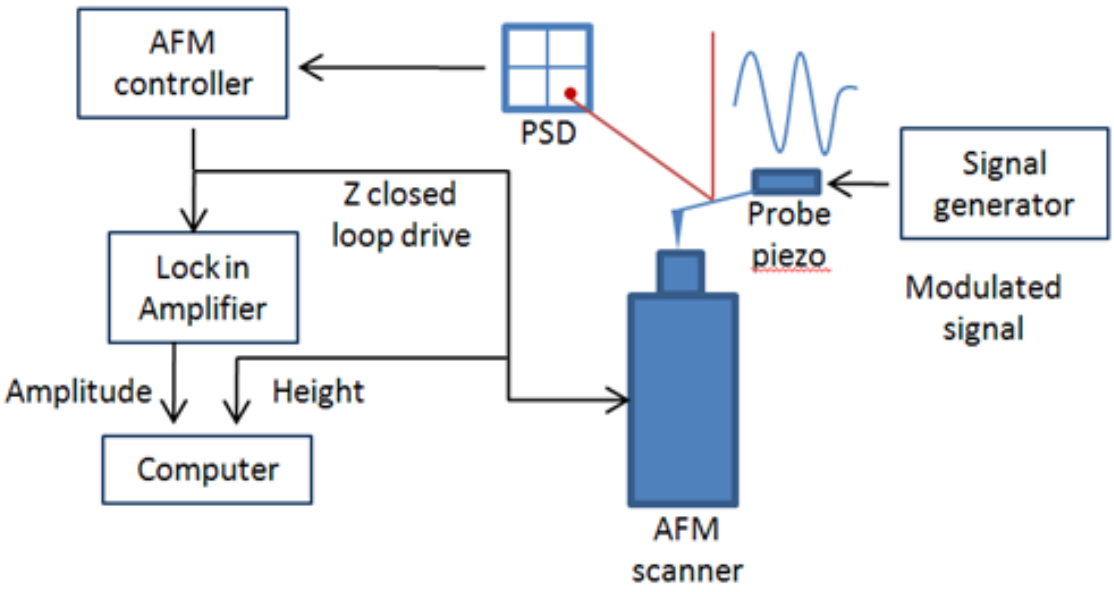

Figure 3.2 Schematic of the setup for the vibration AFM

plitude on the upper surface of sample, other than the driving vibration can be considered as the result of sample deformation which depends on the mechanical properties, such as the spring constant (as shown in Fig. 3.1). However, the spring constant and additional deformation has no directly link between each other. We have to build a mathematic model to connect the estimated spring constant with the measured amplitude.

3.3 Mathematic Model for Vibration Mode

The simplest mathematic model which can describe the vibration system is the traditional spring-mass model. A second order system can be used to build the dynamic model of the vibration system as follows:

$$m\ddot{x} + k(x - A_d \cos\omega_d t) = 0 \tag{3.1}$$

Here we make the assumption that the mass has uniformly distribution of sample. Although the driving signal has been applied in the time domain, the analysis at frequency domain can provide more information to decode the spring constant map.After Fourier transfer (at frequency $\omega = \omega_d$), Eq. (3.1) can be wrote as

$$-m\omega^2 x(\omega) + k(x(\omega) - A_d) = 0 \tag{3.2}$$

and then we have

$$k = \frac{x(\omega)\omega^2}{x(\omega) - A_d} \tag{3.3}$$

Eq. (3.3)is the easiest way to calculate the spring constant of the measured sample. If the measured sample is quit stiff, Eq. (3.3) can be directly applied to the calculation process, however, if the sample is elastic such as cells and bacterial, the conventional second order mass and spring system may not work properly. This is because the model above does not consider the inner connection of each individual points which will compromise the measurement accuracy. In order to solve this issue, we used a three dimensional spring-mass network (as shown in Fig.1) to model the elastic sample.

The second order differential equation was also used to model the behavior of elastic sample. Before the modeling, several assumptions have been made: the mass of each testing point has uniformly distribution, however, the vertical and horizontal spring constant has various distributions. Then the spring-mass network under constant vibration can be modeled as following equation:

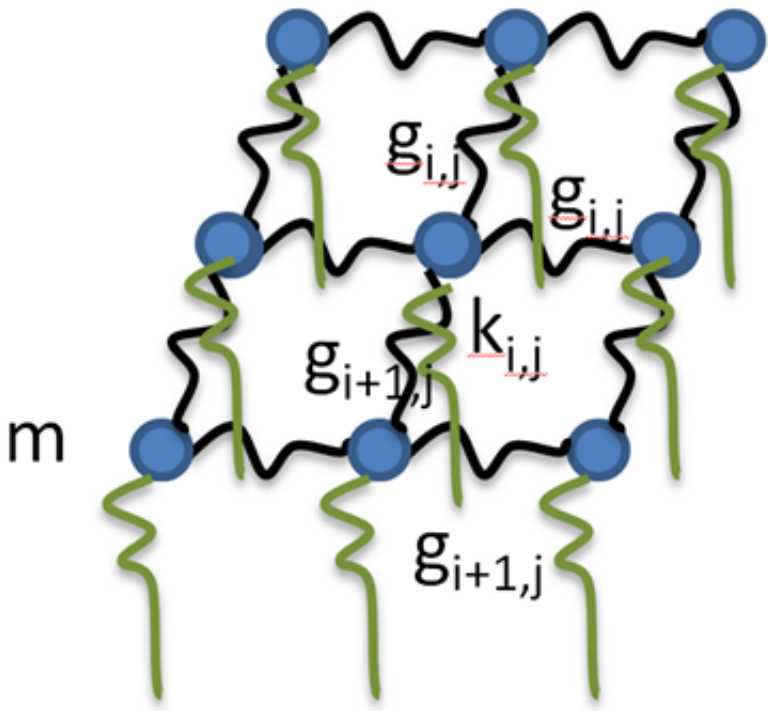

Figure 3.3 Model illustration

$$m\ddot{x}_{i,j} + k_{i,j}(x_{i,j} - A_d\cos\omega t) + g_{i,j}(x_{i,j} - x_{i+1,j}) + g_{i,j-1}(x_{i,j} - x_{i-1,j}) + g_{i,j}(x_{i,j} - x_{i,j+1}) + g_{i,j+1}(x_{i,j} - x_{i,j-1}) = 0 \tag{3.4}$$

where $x_{i,j}$ is the amplitude of at position of (i, j); A_d and ω are the driving amplitude and angular frequency, respectively; $k_{i,j}$ and $g_{i,j}$ are the vertical and horizontal spring constants of the material at position of (i, j), respectively; m is the mass at point (i, j). After Fourier transfer, Eq. (3.4) can be wrote as

$$m(2\pi f)^2 A_{i,j} + k_{i,j}(A_{i,j} - A_d) + g_{i,j}(A_{i,j} - A_{i+1,j}) + g_{i,j-1}(A_{i,j} - A_{i-1,j}) + g_{i,j}(A_{i,j} - A_{i,j+1}) + g_{i,j+1}(A_{i,j} - A_{i,j-1}) = 0 \tag{3.5}$$

where $A_{i,j}$ is the amplitude of at position of (i, j) after frequency lock-in at driving frequency f.

If we write the Eq. (3.5) into matrix form

$$m(2\pi f)^2 \begin{bmatrix} 1 & & & & \\ & 1 & & & \\ & & \ddots & & \\ & & & 1 & \\ & & & & 1 \end{bmatrix} \begin{bmatrix} A_{1,1} \\ \vdots \\ A_{i,j} \\ \vdots \\ A_{n,n} \end{bmatrix} + \begin{bmatrix} A_d - A_{1,1} & & & & \\ & \ddots & & & \\ & & A_d - A_{i,j} & & \\ & & & \ddots & \\ & & & & A_d - A_(n,n \end{bmatrix} \begin{bmatrix} k_{1,1} \\ \vdots \\ k_{i,j} \\ \vdots \\ k_{n,n} \end{bmatrix}$$
$$+ \begin{bmatrix} 2A_{1,1} & 0 & A_{2,1} & & \\ 0 & \ddots & \ddots & \ddots & \\ A_{2,1} & \ddots & \ddots & \ddots & A_{n,n-1} \\ & \ddots & \ddots & \ddots & 0 \\ & & A_{n,n-1} & 0 & A_{n,n} \end{bmatrix} \begin{bmatrix} g_{1,1} \\ \vdots \\ g_{i,j} \\ \vdots \\ g_{n,n} \end{bmatrix} = 0 \tag{3.6}$$

After matrix manipulations, Eq. (3.6) changes into following form.

$$\begin{bmatrix} m(\pi f)^2 & & & & \\ & m(\pi f)^2 & & & \\ & & \ddots & & \\ & & & m(\pi f)^2 & \\ & & & & m(\pi f)^2 \end{bmatrix} \begin{bmatrix} A_{1,1} \\ \vdots \\ A_{i,j} \\ \vdots \\ A_{n,n} \end{bmatrix} =$$

$$\begin{bmatrix} A_d - A_{1,1} & & & 0 & 2A_{1,1} & 0 & A_{2,1} & & \\ & \ddots & & & 0 & \ddots & \ddots & \ddots & \\ & & A_d - A_{i,j} & & A_{2,1} & \ddots & \ddots & \ddots & A_{n,n-1} \\ & & & \ddots & & \ddots & \ddots & \ddots & 0 \\ 0 & & & A_d - A_{n,n} & & & A_{n,n-1} & 0 & 2A_{n,n} \end{bmatrix} \begin{bmatrix} k_{1,1} \\ \vdots \\ k_{i,j} \\ \vdots \\ k_{n,n} \\ g_{1,1} \\ \vdots \\ g_{i,j} \\ \vdots \\ g_{n,n} \end{bmatrix} \tag{3.7}$$

After further manipulation, we transferred the matrix as following linear form.

$$\begin{bmatrix} A_{1,1} \\ \vdots \\ A_{i,j} \\ \vdots \\ A_{n,n} \end{bmatrix} = \frac{1}{m(\pi f)^2} \begin{bmatrix} A_d - A_{1,1} & & & & 0 & 2A_{1,1} & 0 & A_{2,1} & & \\ & \ddots & & & & 0 & \ddots & \ddots & \ddots & \\ & & A_d - A_{i,j} & & & A_{2,1} & \ddots & \ddots & \ddots & A_{n,n-1} \\ & & & \ddots & & & \ddots & \ddots & \ddots & 0 \\ 0 & & & & A_d - A_{n,n} & & & A_{n,n-1} & 0 & 2A_{n,n} \end{bmatrix} \begin{bmatrix} k_{1,1} \\ \vdots \\ k_{i,j} \\ \vdots \\ k_{n,n} \\ g_{1,1} \\ \vdots \\ g_{i,j} \\ \vdots \\ g_{n,n} \end{bmatrix} \tag{3.8}$$

However, we Eq. (3.8) is an under determined equation, which means addition measurement may be needed. If we can make a further assumption that the spring constant in horizontal direction has a uniform distribution. We may simplify the equation. Then the Eq. (3.8) changes into

$$\begin{bmatrix} A_{1,1} \\ \vdots \\ A_{i,j} \\ \vdots \\ A_{n,n} \end{bmatrix} = \begin{bmatrix} 4K+m(\pi f)^2 & 0 & k & & & \\ 0 & 4K+m(\pi f)^2 & \ddots & \ddots & & \\ k & \ddots & \ddots & \ddots & & k \\ & \ddots & \ddots & 4K+m(\pi f)^2 & & 0 \\ & & k & 0 & & 4K+m(\pi f)^2 \end{bmatrix}^{-1} \begin{bmatrix} A_d - A_{1,1} & & & & \\ & \ddots & & & \\ & & A_d - A_{i,j} & & \\ & & & \ddots & \\ & & & & A_d - A_{n,n} \end{bmatrix} \begin{bmatrix} k_{1,1} \\ \vdots \\ k_{i,j} \\ \vdots \\ k_{n,n} \end{bmatrix} \tag{3.9}$$

The Eq. (3.9) can be written as follows:

$$[A] = [Know]^{-1}[Partial - Know][K] = [\Phi_1]^{-1}[\Phi_2][K] = [\Phi] \times [K] \tag{3.10}$$

where A is the measurement results, Φ is the measurement matrix and K is the original signal. When we conduct the amplitude measurement, we can obtain the amplitude $A_{i,j}$ at the specific position (i, j). If we want to directly applied the compressive sensing to these measurement, we have to know the exactly form of measurement matrix. It is not able to directly obtain this measurement matrix, until an additional compressive sensing is applied.

There are two steps of compressive sensing needed in this spring constant measurement, In the first step, we use the partial measurement results to recover the measurement matrix, and in the second step, we use the reconstructed measurement matrix to recovery the original

signal.

In the first step, we are going to recover the Φ_2 matrix. In this matrix, the original signal is A and we also can obtain partial value of some A, in this case we can use the compressive sensing used in topography image to get an entire map of A.

$$Y = \Gamma \times A \tag{3.11}$$

Γ is the measurement matrix which is designed according to the measurement trajectory (the one we designed with TSP). In this case, once the measuring points are fixed, the measurement matrix is obtained. Y is the amplitude measurements results. In this case we can recover the A (the amplitude of every measurement point).

$$[A] = [\Phi_1]^{-1}[\Phi_2][K] = [\Phi] \times [K] \tag{3.12}$$

Now we got the Φ_2 which is generated by the amplitude of every measurement point. Φ is a $n^2 \times n^2$ matrix which is a full rank matrix. If we want to use the compressive sensing, we have to find a subset of Φ as the measurement matrix. In this application, because each row in Φ corresponding to each A, we can choose the row with known measured points. Now, the measurement equation changes to be

$$[A] = [\Phi] \times [K] = \begin{bmatrix} A_{measured} \\ \vdots \\ A_{measured} \end{bmatrix} = \begin{bmatrix} \cdots & \cdots & \cdots \\ \cdots & \cdots & \cdots \\ \cdots & \cdots & \cdots \end{bmatrix} \begin{bmatrix} k_{1,1} \\ \vdots \\ k_{i,j} \\ \vdots \\ k_{n,n} \end{bmatrix} \tag{3.13}$$

In this case, the dimension of A is $m \times 1$, and the dimension of Φ is $m \times n^2$ the dimension of K is $n^2 \times 1$. Now the measurement matrix Φ is a dense random matrix (includes other points information within one measurement) which satisfies RIP. Now, we can use compressive sensing to sample and recovery the spring constant.

Compressive sensing realizes compressing in sampling step. Instead of sampling original signal point by point, compressive sensing only samples a sum of random projections from original signal to a projection matrix (measurement matrix). After a few measurements which are fewer than traditional sampling method, the original signal can be reconstructed by signal reconstruction algorithm. Because the number of measurements is fewer than the dimension of original signal, if the signal is sparse and the measurement matrix has been well selected, the compressive sensing could reconstruct the exact original signal with overwhelming probability. In this application we can use the measurement matrix and image reconstruction designed in Section II.

3.4 Hardware Implementation of Vibration Model on SPM System

The experimental set-up for the vibration mode imaging is shown in Fig. 3.4. For vibration mode imaging, the beam is biased to an optically sensitive position, the z-piezo is actuated by a modulated tapping signal. The carrier frequency is the first order resonance frequency of the AFM probe and the modulated frequency is the vibration frequency at 50 Hz to 100 Hz. Carrier frequency works for the tapping signal for topography image. Additional modulated signal works for vertical vibration generating signal. Since the entire system employs the tapping mode for topography image, the modulated tapping signal is used both

for the topography feedback and AFM stage vibrating simultaneously. Since the carrier frequency locked at resonance frequency of the probe, and tapping signal is used for constant distance between the AFM tip and sample surface, the interaction force also maintains a constant value. The deformation contributed by vibration shows the mechanical properties information such as spring constant. Simultaneously with topography imaging, the vibration amplitude image also is shown in the AFM computer after passing to lock-in amplifier. The lock-in amplifier locks the frequency of modulated signal. As a result, the output of the z-drive signal serves as imaging channel for both the topography and amplitude. In other words, one can obtain topography (height signals) and corresponding mechanical properties signal (amplitude) for every pixel of the image.

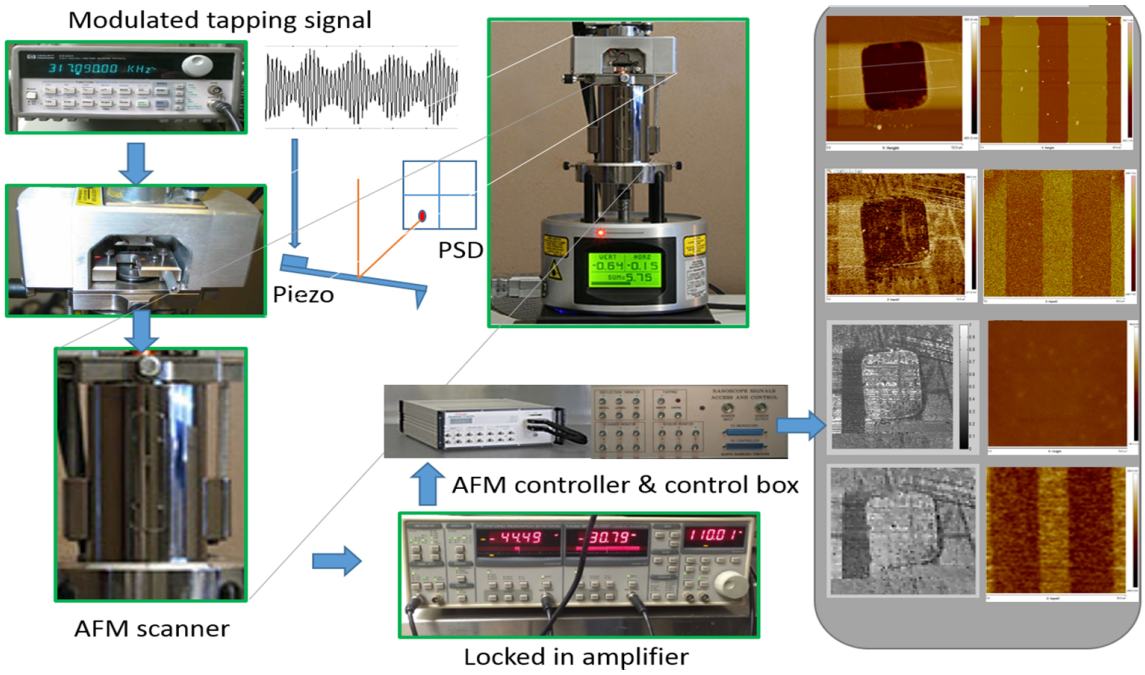

Figure 3.4 Schematic of the setup for the vibration AFM

3.5 Experimental Result

In this experiment, we validate the idea of vibration mode and test its performance compared with conventional tapping mode and contact mode imaging. In this experiment, we started with the known pattern stiff sample such as calibration grid and micro-electrode chip. The goal of these testing is to verify the height (topography) image has the same imaging ability with tapping mode or contact mode. After that we will switch to the soft and elastic samples such as cells.

3.5.1 Topography Image Comparison between Vibration Mode and Conventional Tapping and Contact Modes

The first experiment stated with calibration grid with the standard pitch depth and height. Because the AFM has been calibrated its x, y and z direction using the standard calibration grid (Bruker Nano, Santa Barbara, CA, US), we can assume the position error of conventional tapping mode image is small enough to be used as a standard to evaluate the imaging ability of vibration mode. The Topography image and its cross-section analysis are shown in Fig. 3.5. Through the cross-section analysis, the depth and step of the pitch are 4.994 μm and 0.467μm, respectively. The topography images cross-section analysis from contact mode and vibration mode for the same area are shown in Fig. 3.6 and 3.7 with the the depth and step of the pitch are 4.735 μm and 0.434μm (contact mode), and 4.926 μm and 0.473μm (vibration mode) respectively. The topography images from both tapping mode and vibration mode have the similar measurement value in vertical and horizontal directions and the small difference may come from the uniform fabrication accuracy of calibration grid.

After the testing in calibration grid, a fresh fabricated gold and silicon dioxide micro-

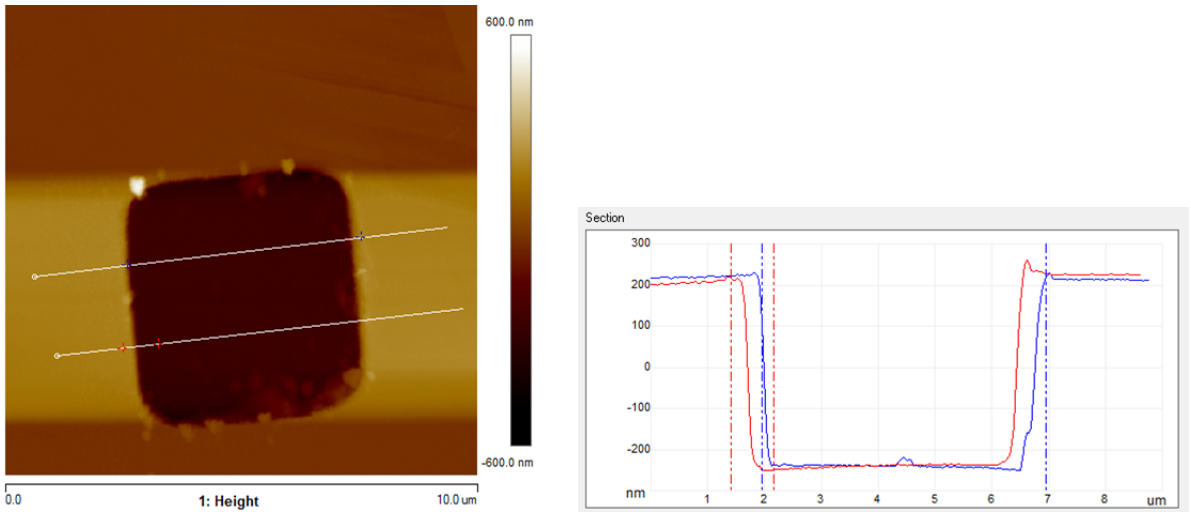

(a) (b)

Figure 3.5 Topography information of calibration grid form conventional taping mode (a): Topography imgae form conventional taping mode (b): cross-section analysis from topography image

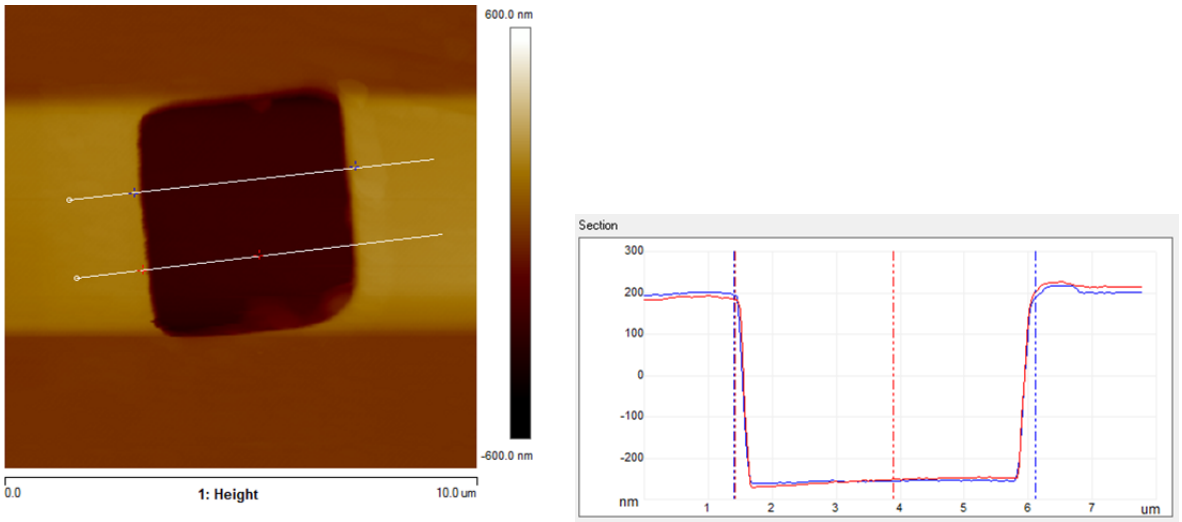

(a) (b)

Figure 3.6 Topography information of calibration grid form conventional contact mode (a): Topography image form conventional contact mode (b): cross-section analysis from topography image

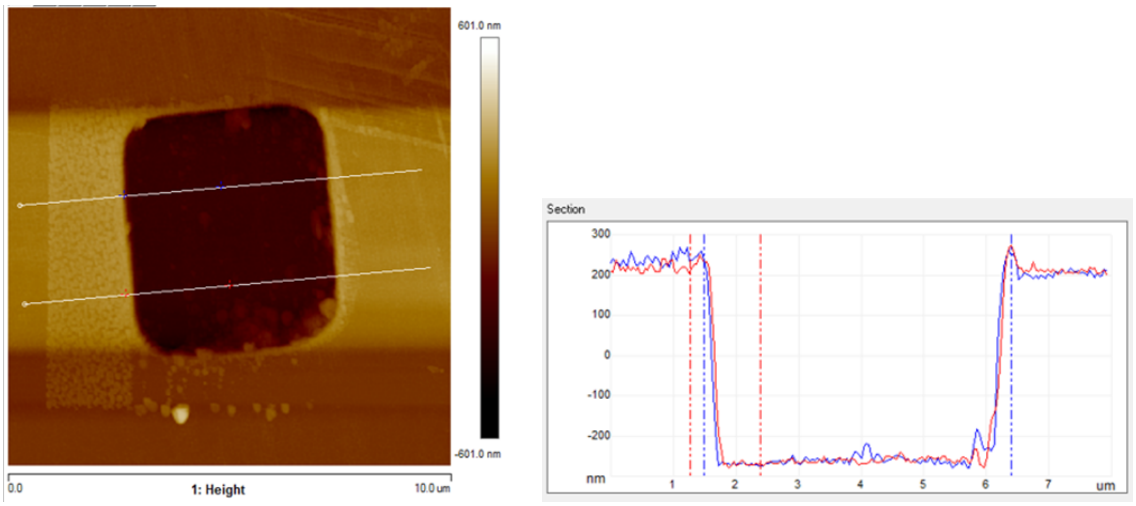

(a) (b)

Figure 3.7 Topography information of calibration grid form vibration mode (a): Topography image form vibration mode (b): cross-section analysis from topography image

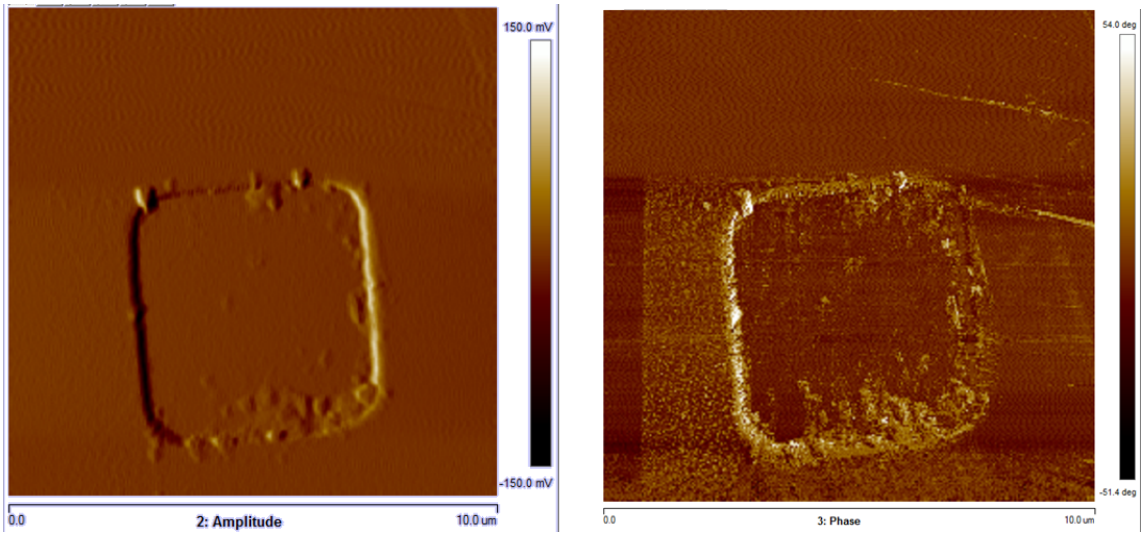

(a) (b)

Figure 3.8 Amplitude and phase images of calibration grid form conventional taping mode (a): Amplitude image form taping mode (b): Phase image form taping mode

electrodes micro chip was used as the sample to test the performance of our vibration mode. Different with the calibration grid, the micro chip has both the topography changes and material changes. The mechanical properties of silicon dioxide is quit different with the gold and which may result in different vibration amplitude in the vibration mode. The experiential results are shown in Fig 3.9 to 3.12

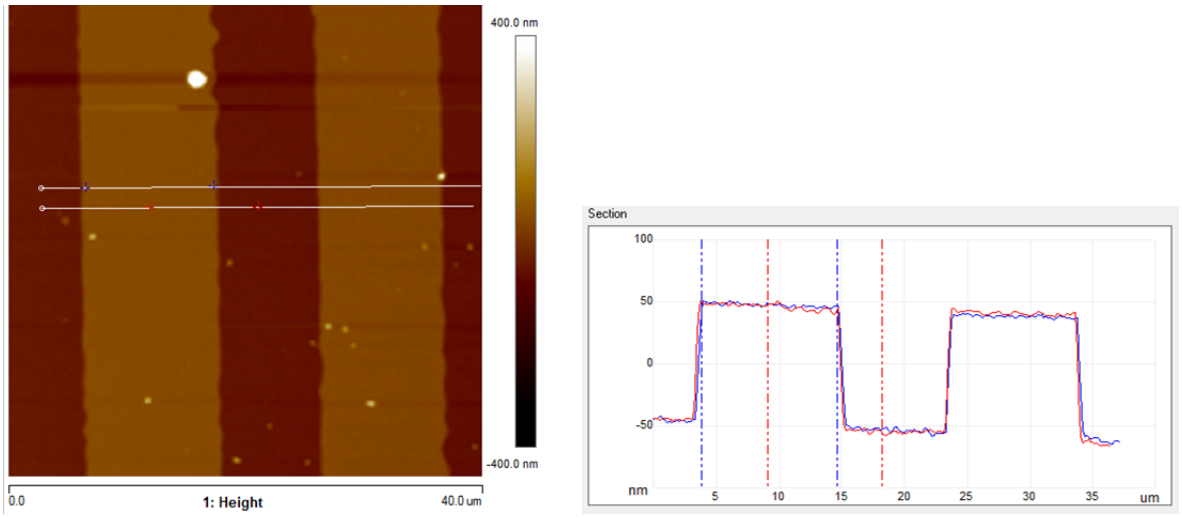

(a) (b)

Figure 3.9 Topography information of gold and silicon dioxide micro-electrodes form conventional taping mode (a): Topography image form conventional taping mode (b): cross-section analysis from topography image

The topography has the similar results with the electrode experiment. The topography images from both tapping mode and vibration mode have the similar measurement value in vertical and horizontal directions. However, the vibration locked in amplitude image in the vibration mode provide us more information other than topography. Fig 3.13(a) and 3.14(a) show the vibration locked in amplitude images of calibration grid and micro chip. Fig 3.13(b) and 3.14(b) are the spring constant map of these two samples by Eq. (3.3). For the calibration grid sample, the effective spring constant has a nonuniform distribution, although the calibration grid has been made by silicon. The reason for that could be the

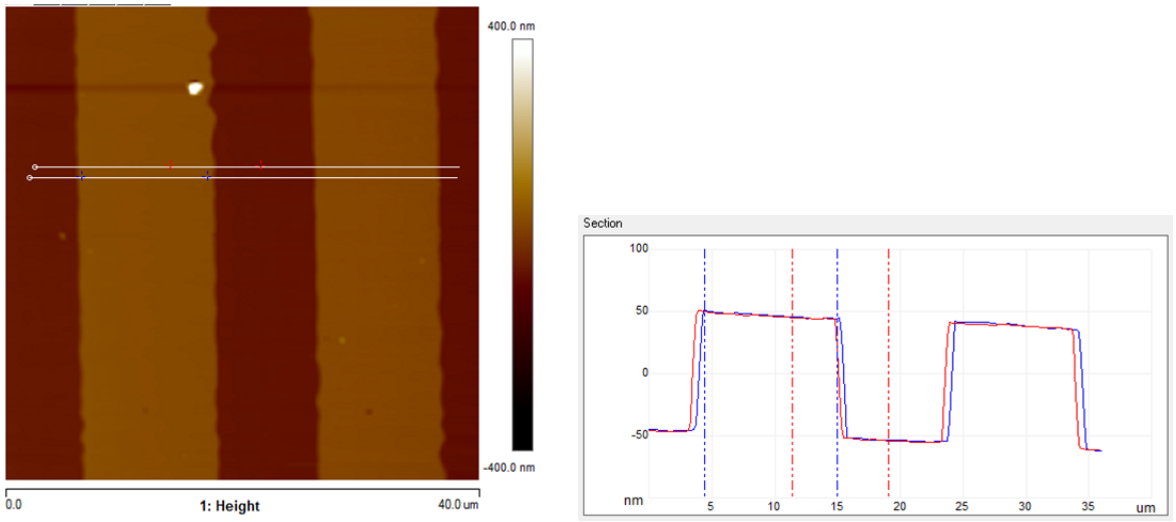

(a) (b)

Figure 3.10 Topography information of gold and silicon dioxide micro-electrodes form conventional contact mode (a): Topography image form conventional contact mode (b): Cross-section analysis from topography image

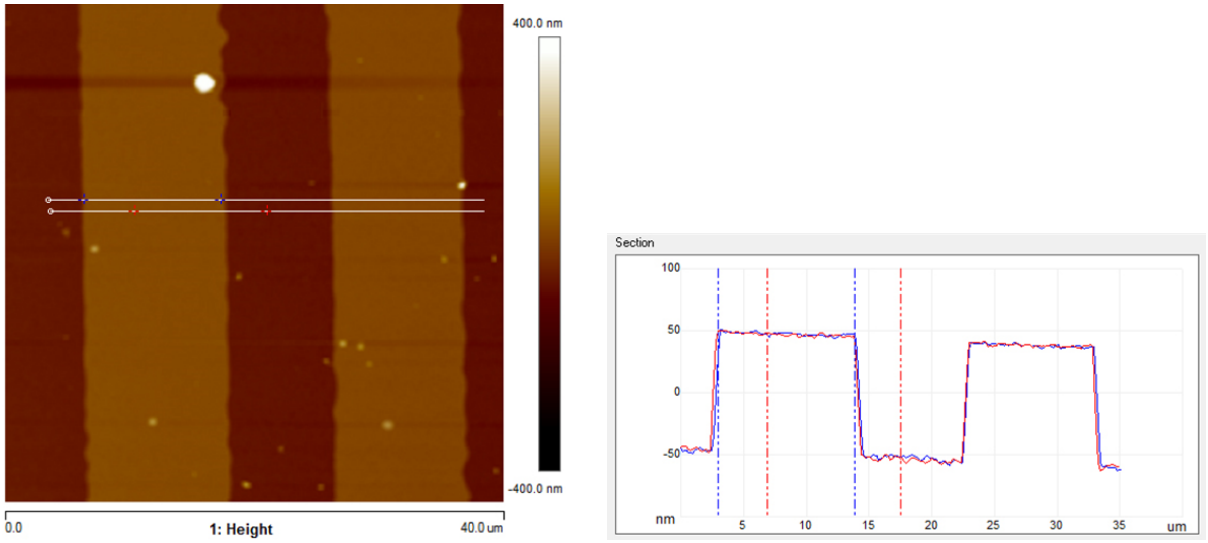

(a) (b)

Figure 3.11 Topography information of gold and silicon dioxide micro-electrodes form vibration mode (a): Topography image form vibration mode (b): Cross-section analysis from topography image

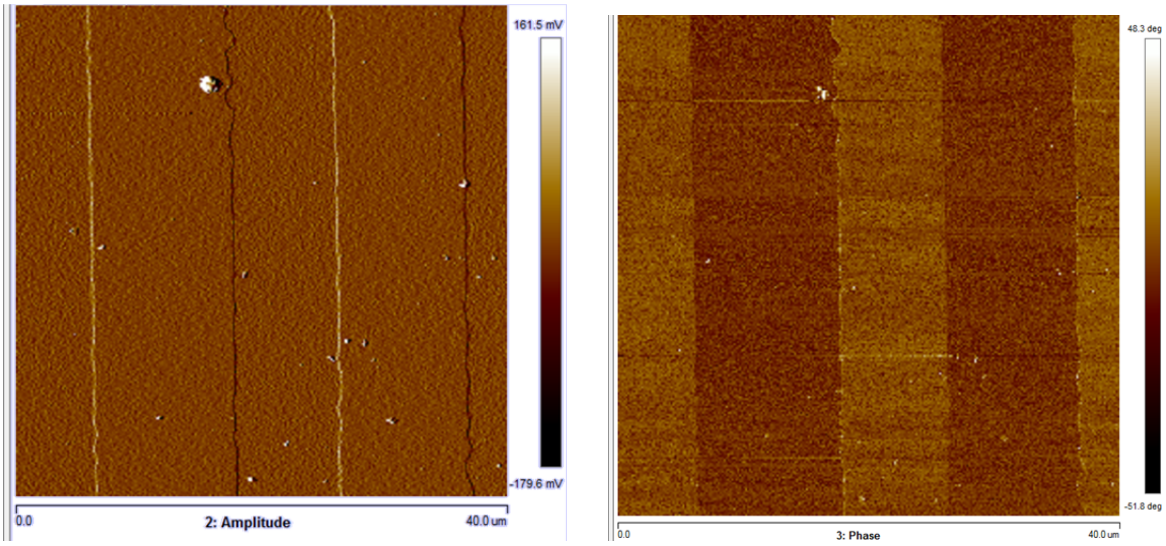

(a) (b)

Figure 3.12 Amplitude and phase images of gold and silicon dioxide micro-electrodes form conventional taping mode (a): Amplitude image form taping mode (b): Phase image form taping mode

surface containments. The topography image should be quite flat if there is no surface containments, however, the topography image in Fig 3.5(a) shows this height changes on the surface of calibration grid which refers to the containments. Since the containments are much softer that he silicon surface and that is the reason in the Fig 3.13(b), the effective spring constant of contaminated area is smaller than the one without contaminated.

3.5.2 Compressive Sensing Involved Topography and Locked-in Amplitude Imaging Test in Vibration Mode

In this section, we tested the performance of compressive sensing based vibration mode. Different with the compressive sensing strategy in Chapter 3, the compressive sensing applied to the vibration mode has the advantage of sampling coupled information within one point measurement. The measurement matrix is much denser than the measurement matrix in Chapter 3. From the theory of compressive sensing, we may achieve higher compression rate

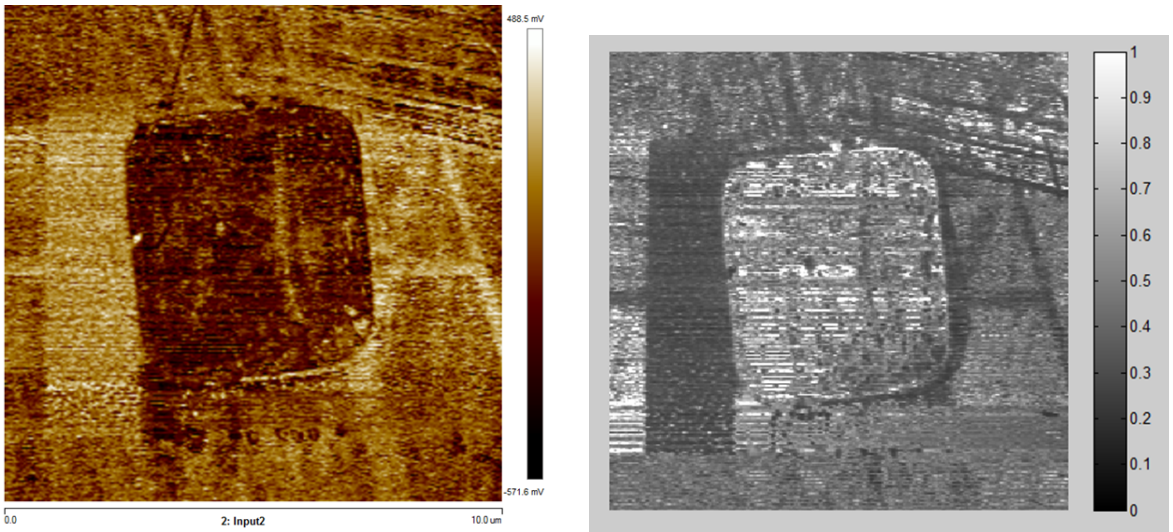

(a) (b)

Figure 3.13 Mechanical properties mapping of vibration mode on calibration grid (a): Locked in amplitude image (b): Effective spring constant map

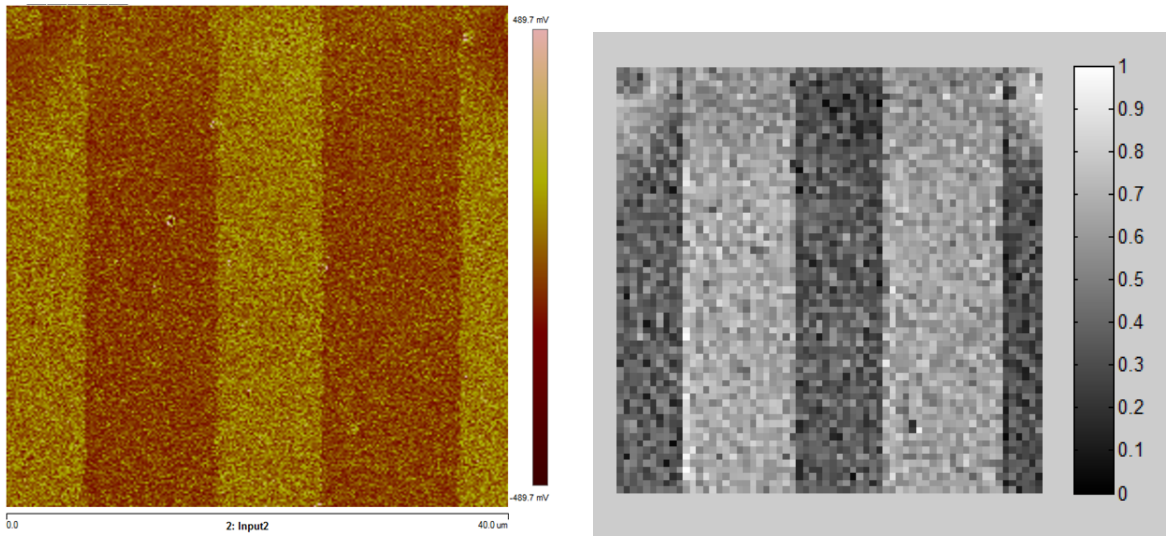

(a) (b)

Figure 3.14 Mechanical properties mapping of vibration mode on micro chip (a): Locked in amplitude image (b): Effective spring constant map

during the measurement. In this experiment we tested the imaging ability of compressive vibration made by calibration grid.

Fig. 5.4 shows the experimental results of the compressive vibration mode with different compression rate. The recovered images looks similar with the full scan image. Even if the compression rate decreased into 10 percents, the recovery image in Fig. 3.15(b) still shows the major information of spring constant map.

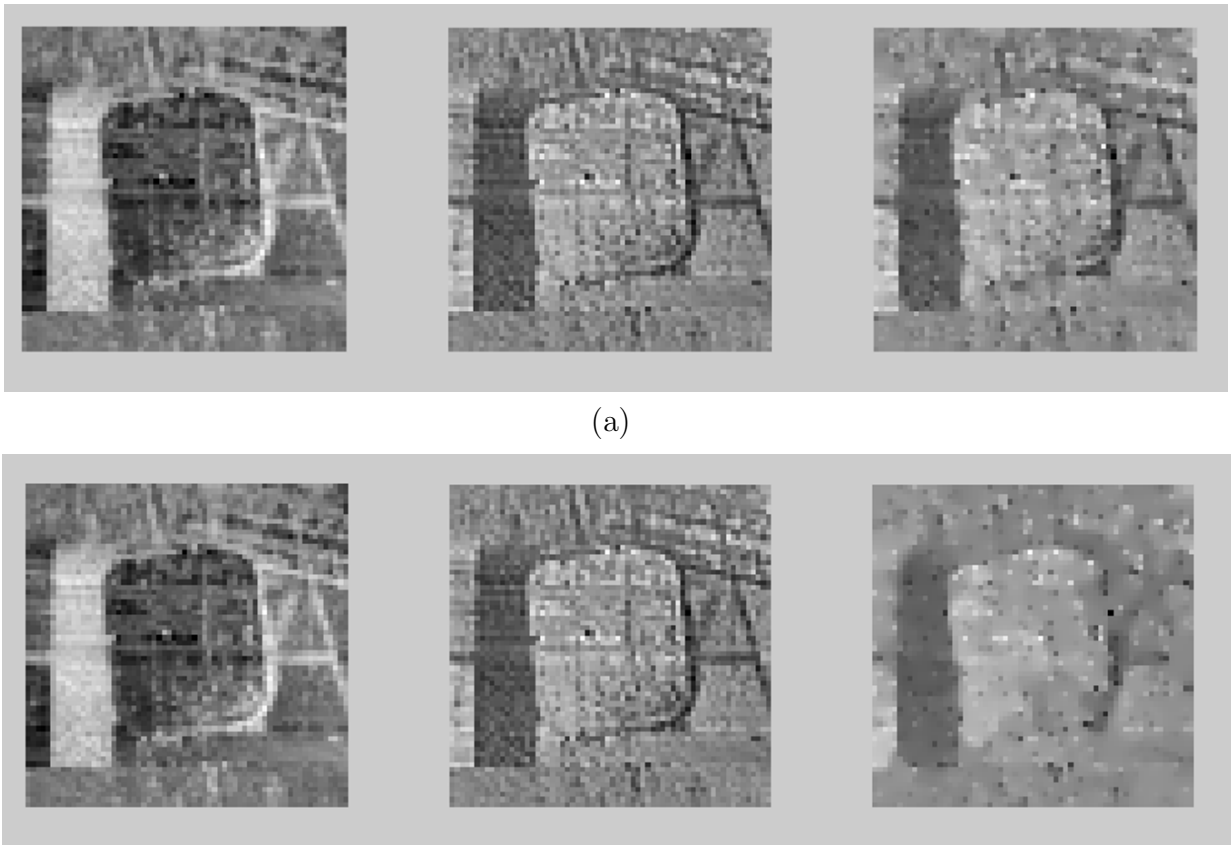

(a)

(b)

Figure 3.15 Experimental results of compressive vibration mode left: Vibration locked in amplitude image by full scan, middle: Effective spring constant map calculated by full scan data, right:Effective spring constant map calculated by compressive scan with compression ratio of (a) 50%,(b) 10%

3.5.3 Subsurface Structure or Mechanical Properties Measurement Using Vibration Mode

Vibration mode measurement is naturally suitable to evaluate the mechanical properties of internal structure of elastic material. If the sample is homogenous, the vibration amplitude signal should be the same on the top of sample surface. However, if there is some defects or other materials inside the sample, the subsurface structure should be able to be detected because of the vibration amplitude changes on the surface. In order to test the performance of subsurface measurement, we fabricate a PDMS coated micro electrodes chip as shown in Fig. 3.16

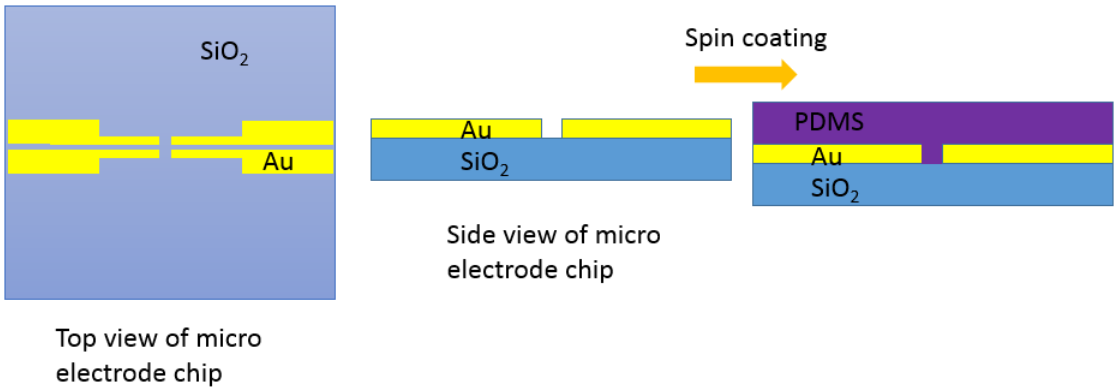

Figure 3.16 PDMS coated micro electrodes chip

We used the vibration mode to scan on the top of PDMS coated micro chip sample and obtained the topography image and vibration locked in amplitude images as shown in Fig. 3.17.

The topography image show nothing but a flat upper surface of PDMS. However, the vibration locked in channel shows a quite different image with the topography channel. The two electrodes berried by PDMS were measured and the vibration locked in amplitude image also showed the different spring constant of the electrode area and silicon dioxide area. It

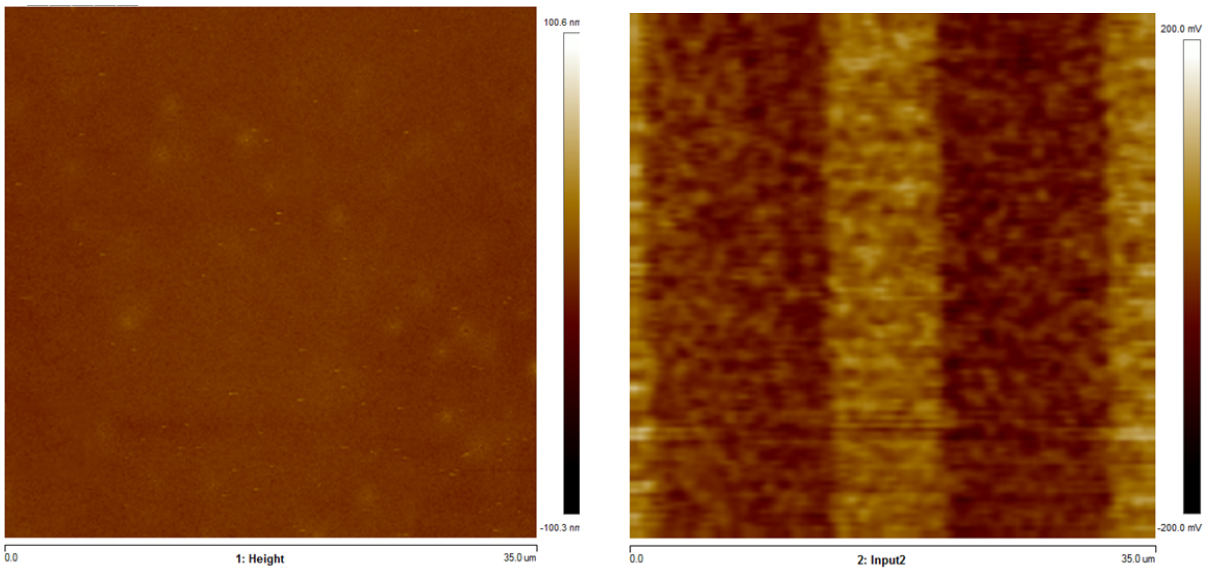

(a) (b)

Figure 3.17 Experimental results of vibration mode on PDMS coated micro chip sample (a): Topography image using conventional tapping mode, (b) Vibration amplitude image

should be noted that the difference in spring constant is not caused by the different materials such as the gold and silicon dioxide. The different locked in vibration amplitude is caused by the difference in PDMS depth. The depth of PDMS in the silicon dioxide region is thicker than the gold electrode region, and these additional PDMS contribute the difference of the vibration locked in amplitude signal. Based on these difference we are able to detect the subsurface structure of the elastic samples.

In order to further test the performance of vibration mode in the aspect of mechanical properties measurement, we designed a PDMS coating sample with different depth of the features (holes) (as shown in Fig. 3.18). The Depth of each feature are: 75 nm for up and down, 150 nm for left and right. After degas process, the PDMS fully filled inside this features with a relative flat upper surface. Both height and amplitude channels of the vibration mode were used to record the information of this sample. The height channel has no information other than a flat surface. However, the mechanical properties channel

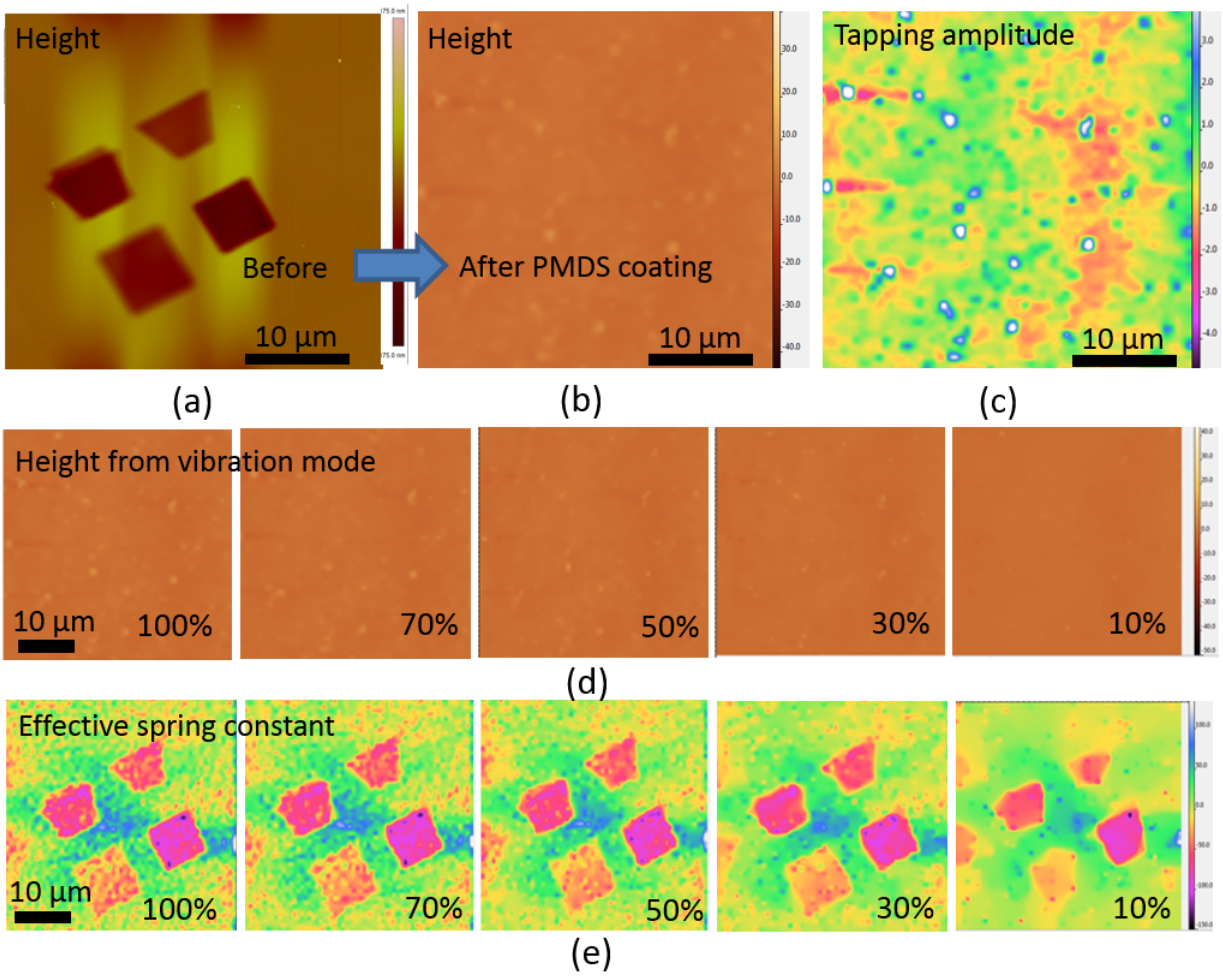

Figure 3.18 Experimental result for the mechanical properties measurement using compressive sensing based vibration mode. (a) Topography image of sample surface before PDMS coating using regular tapping mode. (b) Topography image of sample surface after PDMS coating using regular tapping mode. (c) Tapping amplitude image of sample surface after PDMS coating using regular tapping mode. (d) Topography images of sample surface after PDMS coating using compressive sensing using regular tapping mode. (e) Mechanical properties images of sample surface after PDMS coating using compressive sensing based vibration mode

indicated that, there are for features with different mechanical properties. Fig. 3.18)(e) shows the spring constant of each feature is proportional to its depth which is the same as we expected. In addition, the compressive sensing based compressive scan was also used in this experiment. The experimental results (Fig. 3.18)(e)) shows that 30% of scan rate is enough to distinguish this difference in mechanical properties.

Other than PDMS coating sample, live cells (HacaT) were also used as a testing sample for vibration mode. The result (Fig. 3.19) from vibration mode shows both the spring constant distribution information as well as the height information simultaneously.

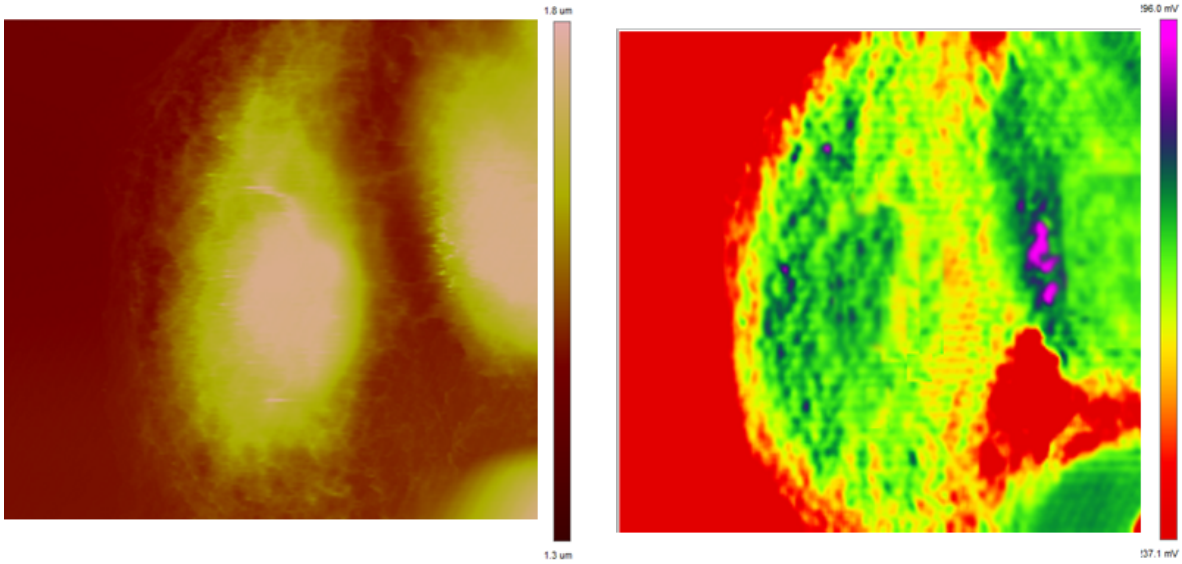

(a) (b)

Figure 3.19 Experimental result for the mechanical properties measurement of live HacaT cell using vibration mode. (a) Topography image of live HacaT cell using regular tapping mode. (b) Vibration amplitude image of live HacaT cell using vibration mode

3.6 Conclusions

In this study, we utilized established and novel noninvasive AFM measurement method, called "vibration mode", to visualize sample and map its stiffness distribution at the nanoscale,

and to determine detailed nanostructural and nano mechanical properties. Our experimental results show that, compared with conventional AFM based imaging and measurements, vibration mode can provide faster imaging speed, and multi-channel information from non-invasive biological properties measurements.

Chapter 4

Video Rate Imaging in Biological Environment

4.1 Introduction

Atomic Force Microscopy (AFM), as an imaging device, has been successfully applied in investigations of nano scale in various areas [69][70][71]. AFM is naturally suitable for imaging in liquid with high spatial resolution. However, its imaging speed is too slow to capture the relative movement between cellulase and celllulose nano crystal. To date, imaging the process of enzymatic hydrolysis is still a challenging work and only a few attempts have been made [72]. In this paper, we propose an approach for a fast imaging AFM, based on a new scan strategy, compressive scan to dynamically observe the interaction between cellulase and cellulose. In this methodology, partial topography information is collected instead of scanning the entire area, and compressive sensing is involved to increase the efficiency of scanning and reconstruct the images using partial information.

Compressive sensing realizes compressing in sampling step. Instead of sampling original signal point by point, compressive sensing only samples a sum of random projections from original signal to a projection matrix (measurement matrix). After a few measurements which are fewer than traditional sampling method, the original signal can be reconstructed by signal reconstruction algorithm [65]. Because the number of measurements is fewer than

the dimension of original signal, if the signal is sparse and the measurement matrix has been well selected, the compressive sensing could reconstruct the exact original signal with overwhelming probability. The AFM based compressive scan, can largely decrease the time spent on scanning, and the reconstructed image is obtained after image reconstruction process. In addition, in order to obtain a better reconstructed image with even fewer measurements, and realize AFM based dynamic observation, a special compressive scan based on prior knowledge is proposed in this paper. It can merge the information obtained by previous frame image and the compressive data obtained by current frame. This approach can largely increase the AFM imaging rate, enhance image quality and realize dynamic observation. In the present study, this compressive scan strategy is used to dynamically observe the interaction between *TrCel7A* and cellulose nano crystal nanofibrils.

Cellulose, a structural component of the cell wall of plants, has been widely considered as a renewable lignocellulosic biomass from waste agricultural products [73][74][75][76]. However, the low efficiency of the enzymatic hydrolysis of cellulose has been seemed as the bottleneck in biorefining industry. The rigid and complexity structure (β-1,4-glycosidic linkages and intra and inter molecular hydrogen bonds) of cellulose increases its resistance to enzymatic hydrolysis and results in a sluggish rate of hydrolytic breakdown of cellulose [77].

Although various methods have been developed to increase the efficiency of the enzymatic hydrolysis of cellulose, such as pretreating the raw cellulose material and assembling cellulase "cocktail", there is still no breakthrough to significantly increase the sluggish interaction between the cellulose and cellulolytic enzymes. Therefore, the cellulose hydrolysis process is not well studied due to the insufficient understanding of the mechanisms underlying enzyme actions [78][79]. The enzymatic hydrolysis of cellulose involves of three different enzymes: cellulases, cellobiohydrolases, and β-glucosidases. In the present study, we focused on the

enzyme of cellulase-*TrCel7A*. The *TrCel7A* is an endo-acting enzyme that can break the glycosidic cellulose chains to generate a new chain end, which can be used for cellobiohydrolase action [80].

4.2 Video Rate AFM Imaging of Cellulose and Cellulase (*TrCel7A*) Interaction

Introducing compressive sensing into AFM imaging system is a convenient and efficient way to reduce the time spent on scanning. The goal is to decrease the scan trajectory, which samples fewer than conventional measurements. Consider an unknown signal (image) x, $x \in \mathbb{R}^N$, $y \in \mathbb{R}^M$ is the measurement results of $y = \Phi x$, and Φ is the measurement matrix. If $M \ll N$, fewer measurements might be enough for sampling and reconstructing the original signal. There are three major sections in compressive sensing: signal sparse representation, measurement matrix design and signal reconstruction algorithms. The details of signal sparse representation and reconstruction algorithms can be found in our previous research [81]. In this research, the measurement matrix design is different from the previous one. The new measurement matrix also takes the information of the previous frame into account, and integrates it with the information of the current frame to assure that, the original image can be accurately reconstructed.

The main difficulty in comprehending the mechanism of the interaction between cellulolytic enzymes and cellulose is the absence of quantitative analytical methods. *In situ* visualization is possible to be an alternative method to study the mechanism of the interaction between cellulolytic enzymes and cellulose nano crystal nanofibrils. *In situ* images can provide spatial resolution in nano scale, and are able to capture the single cellulase bound

on surface of cellose crystal nanofibrils.

The recent introduction of high-speed AFM breaks the limitation and can visualize the behavior of single molecules of *TrCel7A* during hydrolysis of cellulose without enzyme labeling or substrate modification [82] [83]. High resolution AFM imaging at video-rate can help directly visualize the active single *TrCel7A* molecule on cellulose II surface with enough temporal resolution to track its movement. *TrCel7A* is a major component of Trichoderma reesei cellulolytic system, which produces cellobioese from the reducing end of cellulose [84], [85]. The *TrCel7A* molecule contains an active site which resides in a 40-50 angstrom long tunnel and binding sites for 10 glucose units [86]. *TrCel7A* is known to hydrolyze the crystalline cellulose chain in a processive manner, making consecutive cuts of cellulose chain through the tunnel-shaped active sites [82] [87].

4.3 Experimental Setup and Results

4.3.1 Preparation of Cellulose Crystal Nanofibrils and *TrCel7A* for AFM Imaging

Preparation of cellulose solution The cellulose solution (0.01 mg/ml) was prepared by dissolving cellulose in urea solution (12% wt urea, 7% wt NaOH). The solution was stored in -20 °C fridges for 1 hour with stirring from time to time [88][89]. *Anchoring mica substrate* Fresh clave mica was cut into 0.6 cm × 0.6 cm pieces. Mica substrates were washed by immersing in 10% NaOH solution, followed by rinsed with DI-water, dried with nitrogen gas, and placed in a UV/ozone oven for 15 min. 3-Aminopropyltrimethoxysilane (APTS) was adsorbed onto the silica substrates in order to improve the coverage of the nanofibrils.

Washed silica substrates were immersed into 1% v/v APTS/toluene solution for 40 min, rinsed with toluene and dried in an oven at 60 °C for 30 min.

Preparation of cellulose nanofibrils Add one drop of cellulose solution on mica substrates. After 20 min, raised by DI-water and dried with nitrogen gas.

Preparation of TrCel7A The *TrCel7A* was a gift from Dr. Jun Xi's group at Drexel University. For the preparation of appropriate dilutions, the *TrCel7A* was diluted to 50 μM enzyme solution.

4.3.2 *In Situ* Visualization and Image Analysis

AFM *in situ* imaging was conducted using a commercial AFM (Multi-Mode, Bruker Nano, CA) with a signal access and control box, which was developed by our group to control the AFM probe. Silicon nitride probes (SNL-10, Bruker Nano, CA) were used to image the cellulose nano crystal nanofibrils and *TrCel7A* in imaging buffer. The cellulose sample was initially observed without *TrCel7A* in 80 μl of imaging buffer (50 mM sodium acetate buffer with pH 5.0), followed by the addition 5 μl of 50 μM enzyme solution. A specially designed scan trajectory was used to perform a continuous random sampling, and the prior knowledge based compressive sensing was used to dynamically observe the sample surface change. At the beginning of each experiment, an AFM image was obtained by conventional raster scan as the first frame. After that, prior knowledge scan strategy started to take over the imaging work of all the rest frames. Stationary cross section analysis was conducted by AFM image processing software (Nanoscope Analysis, Bruker Nano, CA).

4.4 Results and Discussion

4.4.1 Size and Shape of Cellulose Nano Crystal Nanofibrils and *TrCel7A*

The cross-section analysis was conducted by conventional AFM. We chose an area with a number of cellulose nano crystal nanofibrils, and used AFM to image the height and amplitude channels. Fig. 4.1(a) is the amplitude image of cellulose surface. Fig. 4.1(b) and 4.1(c) are the zoomed in image in the same location. Fig. 4.1(d) is the cross-section profiles of single cellulose nano crystal nanofibrils. Through these images, the shape and contours of each cellulose nano crystal nanofibrils could be found. The size of typical cellulose nano crystal nanofibrils we observed is 250 nm (width) $\times$ 60 nm (height), and the length in the measurement is various form one to tens of micrometers with the most frequency of $3\mu m$. According to the size of cellulose, the sample looks like a small bundle of cellulose nano crystal nanofibrils. The reason for these presented cellulose nano crystal bundles is because the procedure of our cellulose nanofibrils preparation process.

After addition of *TrCel7A* enzyme, individual *TrCel7A* bound with cellulose nano crystal nanofibrils was imaged by conventional tapping mode AFM in imaging buffer. The single *TrCel7A* bound on cellulose surface was capture as Fig. 4.2. Fig. 4.2(a) and 4.2(b) are the amplitude images of single *TrCel7A* on the cellulose surface, the scale bar is 70 nm. Cross-sectional analysis was performed to quantify the *TrCel7A*, which has a height of 4 nm and is 25 nm$\times$ 15 nm in length and width, respectively. According to published results on structures of the *TrCel7A* in the catalytic domain (approximately 6 nm $\times$5 nm $\times$ 4 nm), and the projection of a bound *TrCel7A* molecule away from the cellulose surface may be

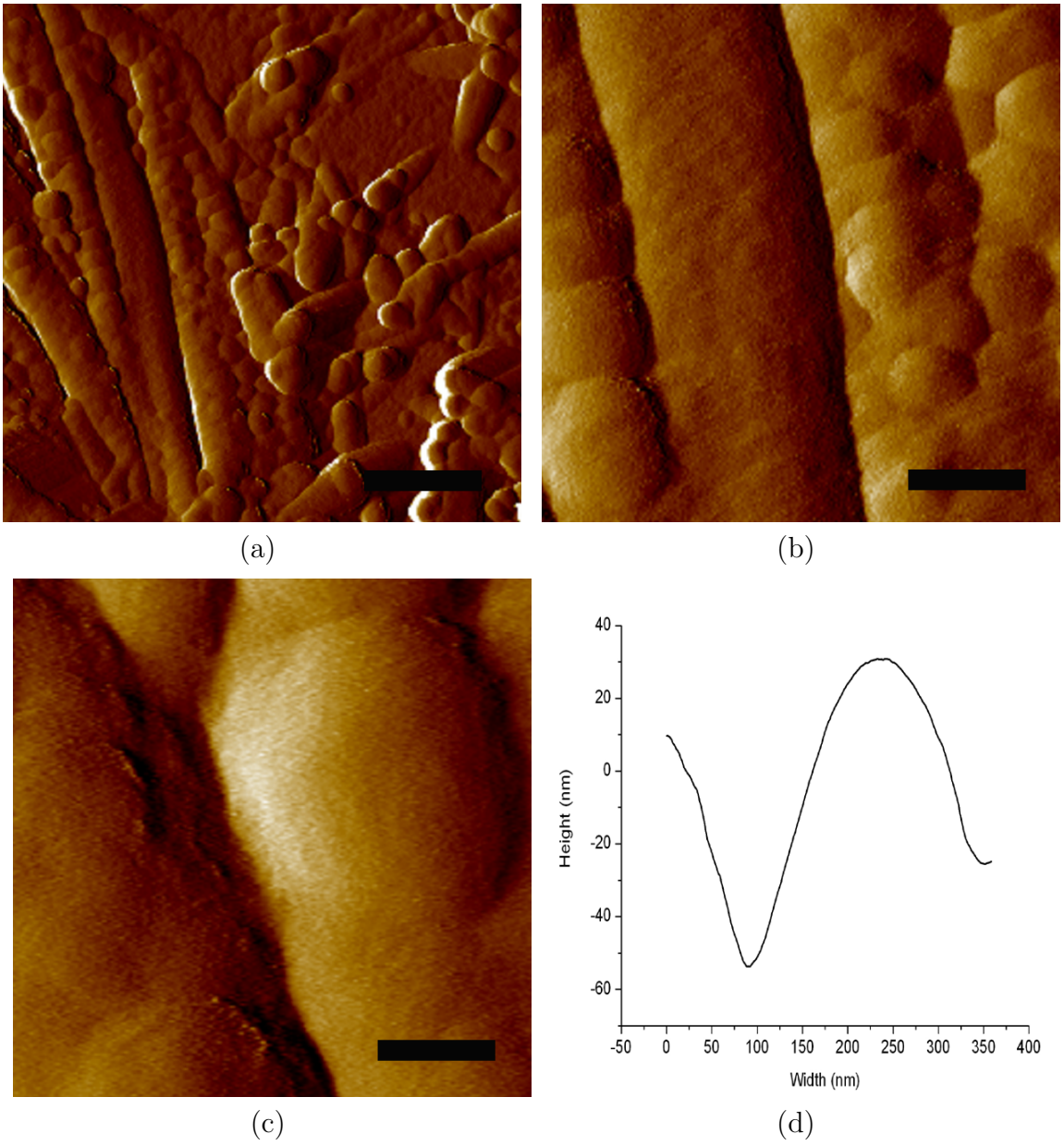

Figure 4.1 Visualization of cellulose nano crystal nanofibrils. (a) Amplitude image of cellulose nano crystal nanofibrils (scan bar: 800 nm), (b) Zoomed in amplitude image of cellulose nano crystal nanofibrils (scan bar: 220 nm), (c) Zoomed in amplitude image of cellulose nano crystal nanofibrils (scan bar: 100 nm), (d) Height analysis of cellulose nano crystal nanofibrils

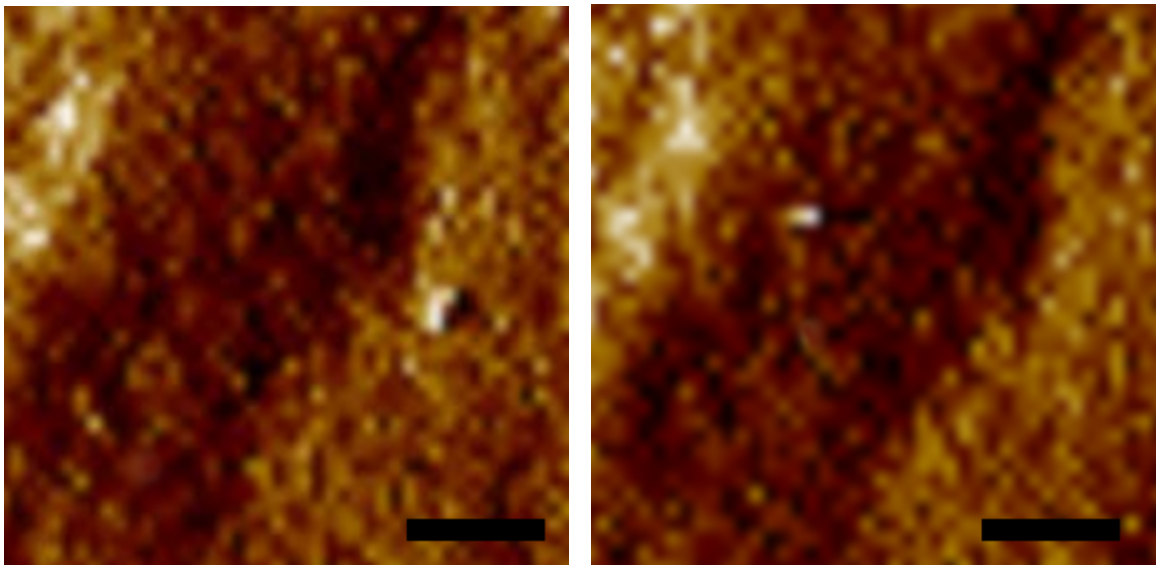

(a) (b)

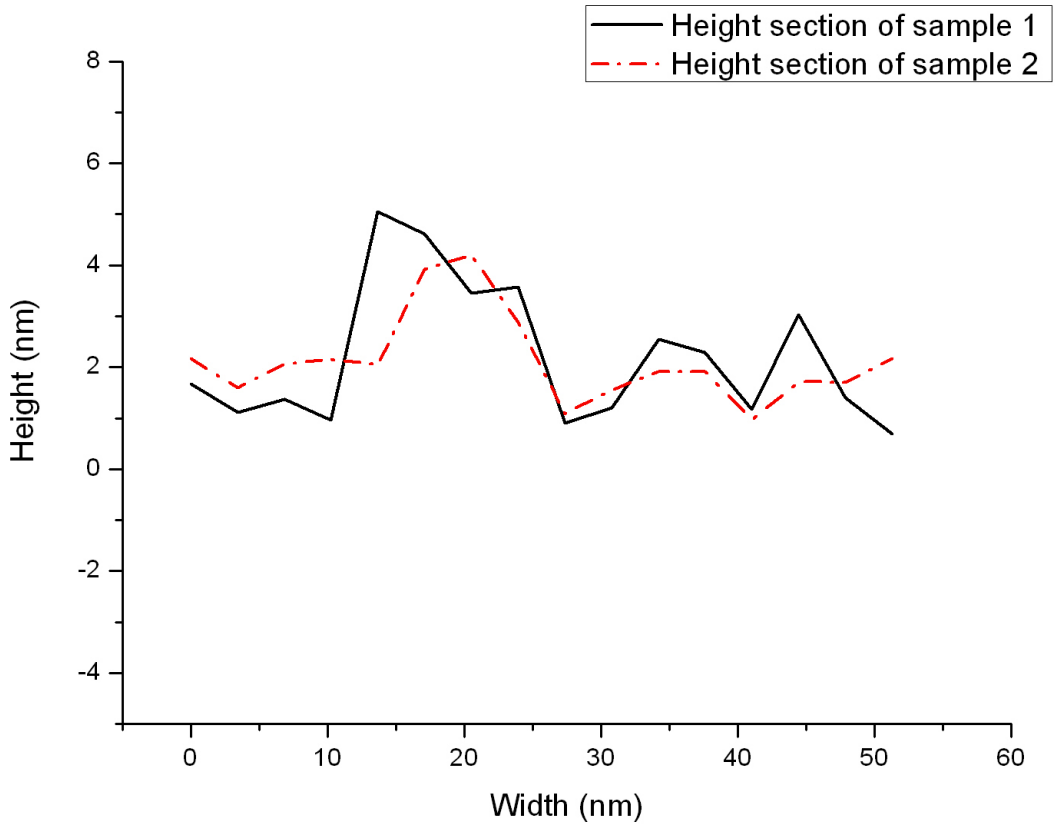

(c)

Figure 4.2 Visualization of *TrCel7A* enzyme. (a) and (b) AFM amplitude image of *TrCel7A* on cellulose nano crystal nanofibrils surface (scan bar: 70 nm), (b) Amplitude image of cellulose nano crystal nanofibrils (scan size: 2.2μm), (c) Height analysis of cellulose nano crystal nanofibrils, black curve for *TrCel7A* in image (a), red curve for *TrCel7A* in image (b)

inferred to be between 5 and 10 nm [90], the nanoparticles we observed are most likely to be the *TrCel7A*.

4.4.2 *TrCel7A* Binds to Cellulose and Moves

In the present study, we performed *in situ* AFM imaging of *TrCel7A* bound on cellulose nano crystal nanofibrils, and dynamically observed the relative movements of these two nano structures. The enzymatic hydrolysis of cellulose nano crystal nanofibrils was studied using cellulose films deposited on fresh cleaved mica substrates in 50 mM sodium acetate buffer with pH 5.0 at room temperature, 21 ± 1°C. *TrCel7A* was added to the AFM fluid cell to study the enzymatic hydrolysis of cellulose sample. Fig. 4.3 shows the progression of the movement of *TrCel7A* on the cellulose nanofibrils observed over a period of 15 seconds. Fig. 4.3(a) is the amplitude image with the scan size of 180 nm $\times$500 nm obtained by our prior knowledge based fast imaging system. In this image, it is clear to see three single *TrCel7A*s bound on the cellulose surface. Fig. 4.3(b) shows the dynamic observation of a single *TrCel7A* on the surface of the cellulose nano crystal nanofibrils with the time interval of 1.8 seconds. The images were captured and recovered by prior knowledge based fast imaging system over a period of time (15 seconds). The flat ball shape feature in each frame could be *TrCel7A* enzymes binding to the cellulose surface (in the process of enzymatic hydrolysis), according to that these moving particles were not seen in the absence of the enzyme, we conclude that they are *TrCel7A* sliding on crystalline cellulose nanofibrils.

During the observation, most of *TrCel7A* molecules were found with a similar moving velocity on the cellulose nanofibrils surface, and the average rate of movement was estimated to be 2.35 ± 1.2 nm/s (n=10). Compared with the movement velocity obtained from other research (3.5 ± 1.1 nm/s) [82], our measurement result is in the same level. The fast imaging

AFM we used in this research could reach as high as 1 frame/second, however, the time-resolution is not high enough to capture the details of *TrCel7A* enzymatic hydrolysis of cellulose, and that needs to further increase the imaging rate of AFM in the future.

4.4.3 Time-lapse of Density and Distribution of *TrCel7A* Molecules on Cellulose Substrate

The density of *TrCel7A* (Fig.2C) on substrate is also important since it indicates the effective adsorption of cellobiohydrolases and is mediated by the CBD [91]. The adsorption of the family 1 CBD on crystalline cellulose requires three aromatic amino acids, and the binding sites to cellulose crystals [92]. Due to the processive characteristics of hydrolysis, the binding of *TrCel7A* and cellulose affects the hydrolysis rate. Generally, efficient enzymatic hydrolysis requires high binding density, high moving velocity and low dissociation rate [93]. Since the hydrolysis is a dynamic process, at each moment there always exists a number of active *TrCel7A* molecules bound on cellulose surface. At that moment, some of the *TrCel7A* on the surface will detach to the solution, and some new binding activities of *TrCel7A* appears. Considering the stochastic nature of the process, we used Poisson process to estimate the mean value of the density of active *TrCel7A* (Eq.1 and Eq.2). During the observation, we set the time interval as 5 minutes. We set the AFM imaging speed as 0.6 frame/s and group every 5 frames to calculate the expected value of the number of active *TrCel7A*. We could collect approximately 36 expected values of the number of active *TrCel7A*, and use these values to statistically analyze the mean and variances of number of active *TrCel7A* within the 5 minutes period. Figure 2C shows one frame of the continuous observation with the number of active *TrCel7A*.

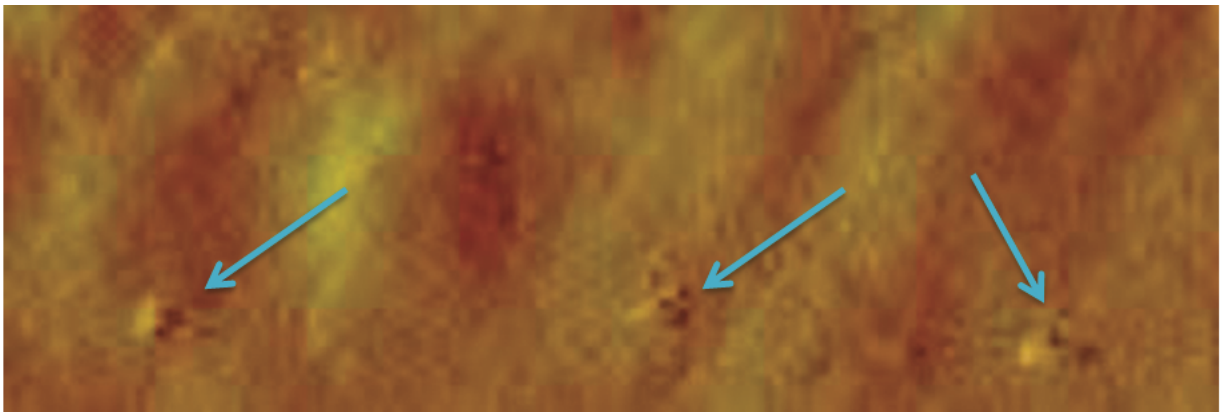

(a)

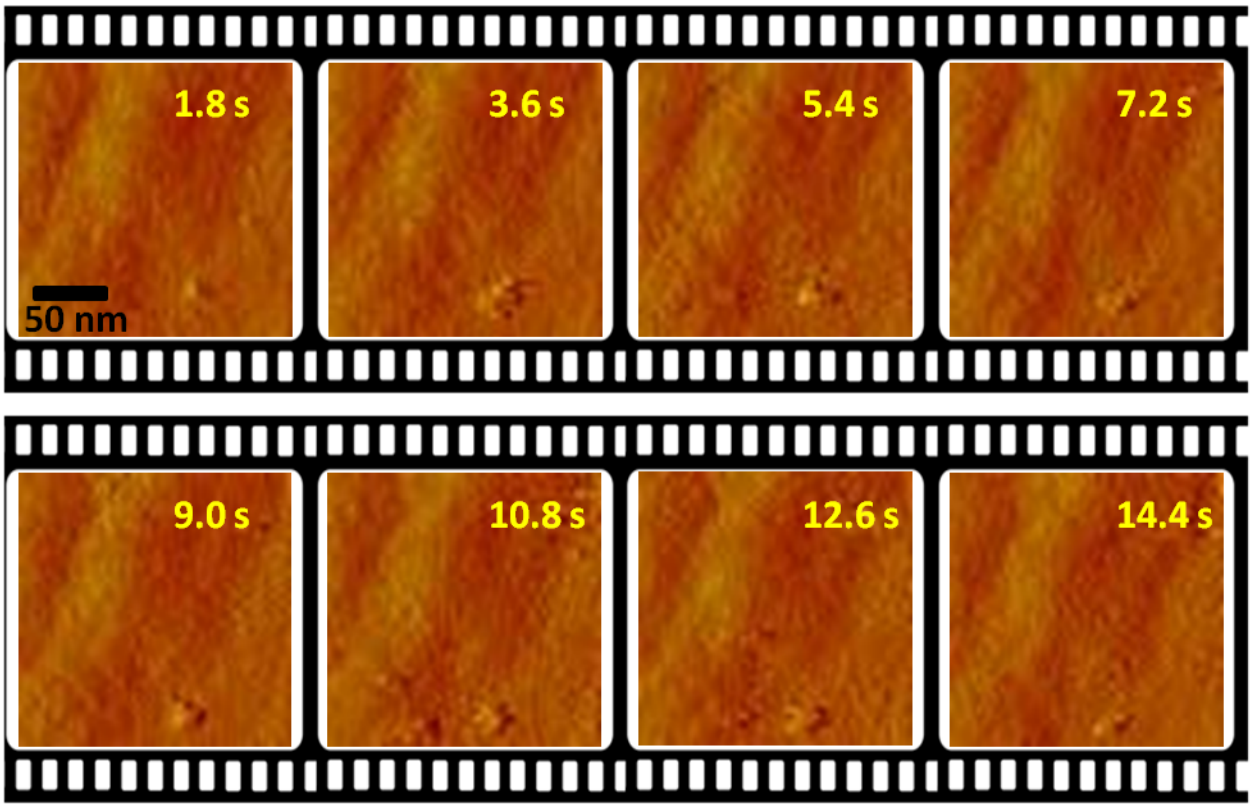

(b)

Figure 4.3 *In Situ* visualization of dynamic interactions of cellulase and cellulose molecules, (a) *TrCel7A* (labeled with arrows) bound to Cellulose (scan size: 180 nm ×500 nm), (b) Time lapse amplitude images of an individual *TrCel7A* moving on the a single cellulose nano crystal nanofibrils (scan size: 180 nm ×180 nm)

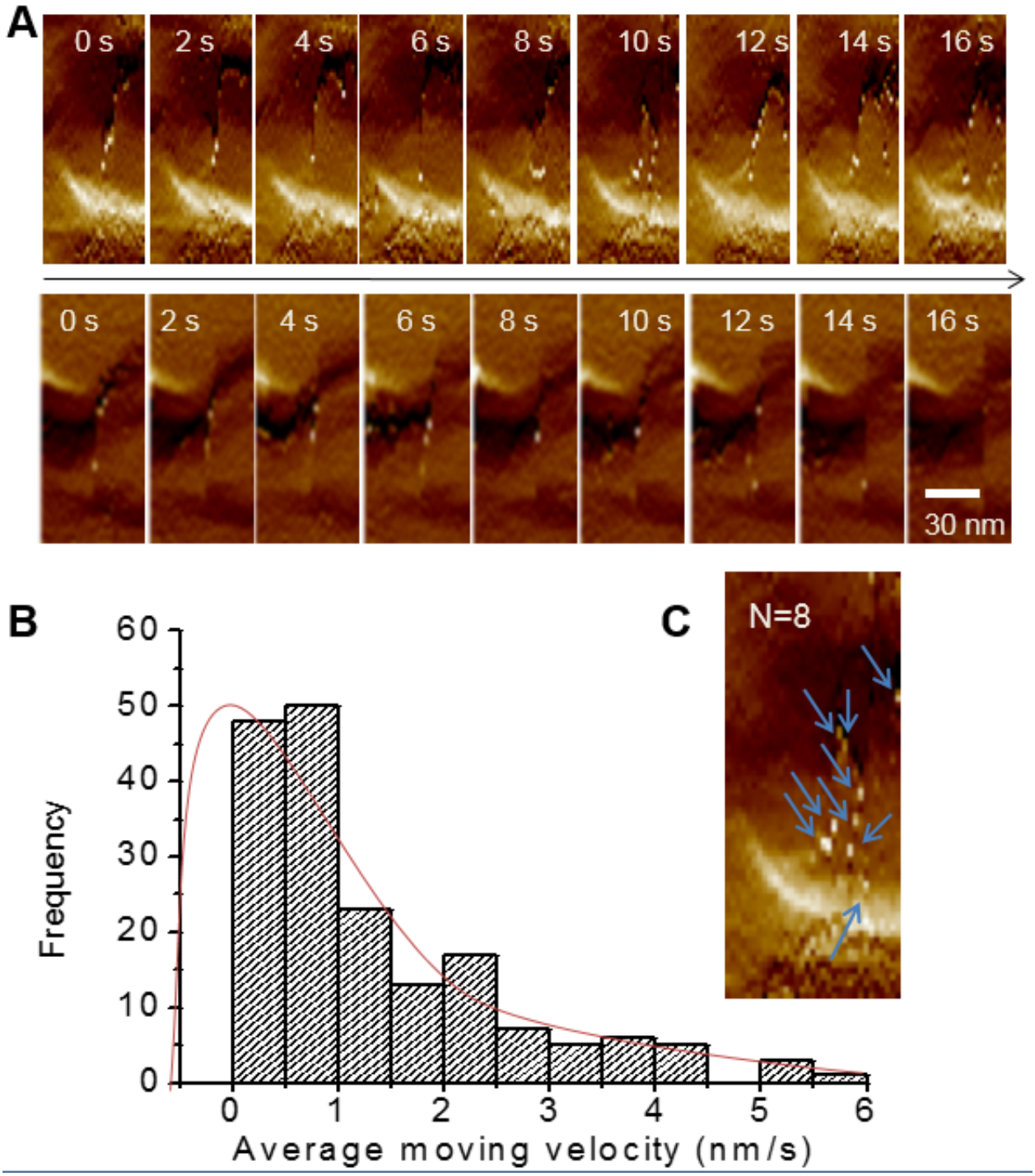

Figure 4.4 Video-rate AFM Observations of *TrCel7A* (50 μm) molecules bound on cellulose substrate. (a) Continuously captured AFM frames of moving *TrCel7A* on cellulose substrate (two different locations: (a1) and (a2)) in 50 mM sodium acetate buffer with pH 5.0. Imaging frame rate: 0.5 frames/s. (b) Histogram of average moving velocity of *TrCel7A* . The velocities were calculated by the modified Hausdorff distance and fitted by Poisson distribution (Detailed in supplemented material). (c) *TrCel7A* molecules counting based on AFM images. Positions of each *TrCel7A* molecule are labeled with arrows.

The surface density of active *TrCel7A* on cellulose surface decreases over time after they were added onto the cellulose substrate (Figure 2A). Representative frames for *TrCel7A* counting are shown at the time of the start point, 20 minutes, 45 minutes and 75 minutes (Figure 3B), respectively, after the reaction started. The surface density of active *TrCel7A* declined to 50% of initial value after 10 minutes, and 10% 40 minutes after adding *TrCel7A*. The density of active *TrCel7A* reached a steady state of 5% after 60 minutes. We used an empirical exponential decay function (Eq.3) to fit the experimental data, and the decay constant is b=0.0592. While the number of active *TrCel7A* rapidly decreases over time, the average moving speed of *TrCel7A* on cellulose substrate only decreased slightly (b=1.710-8 in Fig.3 C), which could be negligible. This reduction of active *TrCel7A* could cause hydrolytic rate declining during hydrolysis in our results (Fig. 4). From the perspective of enzymatic hydrolysis, when *TrCel7A* hydrolyze cellulose, the enzyme-cellulose complex should consist of the soluble enzyme solution and the insoluble substrate cellulose. *TrCel7A* enzymes have to act at the solid-liquid interface during hydrolyzing cellulose. The CBD of *TrCel7A* is either deactivated or attenuated in the scale of hours, which results in the percentage of active *TrCel7A* keep decreasing as the hydrolysis reaction going on. In previous studies, CBD was known for its ability to enhance the concentration of enzymes rather than its active role in cellulose hydrolysis. CBD could penetrate cellulose chains and serve to feed chain into the active site tunnel of the CD [94]. The binding of individual *TrCel7A* on cellulose surface could be classified into two categories: productive binding (binding by both CD and CBD) and non-productive binding (binding by CBD only). For the single molecular observation, both productive binding and non-productive binding were observed during the experiment. Since the *TrCel7A* belongs to the category of motor protein, and the motion energy comes from the hydrolysis of a glycosidic bond of cellulose (approximately -12.5kJ/mol) [82], the observed

TrCel7A molecules that are in motion can be considered as active enzymes or productive enzymes; while non-productive enzyme cannot move along the surface of cellulose, due to the lack of driving energy from hydrolysis [82]. Therefore, the majority of active *TrCel7A* molecules observed in our study can be considered as the productive enzymes, as they were moving along the cellulose surface. However, the active *TrCel7A* may be transformed from the productive state into non-productive state, such as enzyme jamming (Fig.S3). Surface defects could stack *TrCel7A* molecules within a short period of time, and subsequently the jamming could be broken off and non-productive *TrCel7A* molecules come back to be productive. In this study, we considered these temporal non-productive molecules as active *TrCel7A*.

Alternative methods were also used to estimate the quantity and activity of active *TrCel7A*. Ma et al. calculated the quantity of active *TrCel7A* as the difference between the masses of adsorbed and irreversible (deactivated) *TrCel7A*29. Their results indicated that the activity of active *TrCel7A* has no significant change, even as the hydrolytic rate during hydrolysis decreased. This result echoed our finding that the moving velocity of active *TrCel7A* had slowed only slightly. They also found that the number of active *TrCel7A* experienced no significant change, but we found the density of active *TrCel7A* was reduced with time. The difference between our current results and data by Ma et al. may be due to the difference in experiment design method. They used bulk solution with wash-off method, while we used single molecular observation technique, which should be more accurate.

4.4.4 Cellulose Substrate Changes Indicates Enzymatic Hydrolysis Rate

Besides capturing the movement and calculating the surface density of active *TrCel7A*, we also measured the topographic information of cellulose as an indicator of hydrolysis rate [95]. AFM imaging (well-tuned tapping amplitude) does not cause mechanical damage to cellulose surface, thus, the observed topographic changes in cellulose during enzymatic hydrolysis can be interpreted as the result of enzymatic action. The chains of cellulose II used in this study have almost perfect two-fold symmetry and are compatible with occurrence of two intermolecular hydrogen bounds between consecutive residues. The crystal structure consists of anti-parallel chains with different conformations but with the hydroxymethyl groups of both chains near the gauche-trans orientation [96]. Normally the crystalline micro-fibrils have the cross sections of 4-6 nm. However, in this study, most of the time, the micro-fibrils have been stacking together with cross sections of 0.5-5 μm. The height changes of cellulose after addition of *TrCel7A* were calculated from the topography images (Fig.4C). The average height of the fiber decreased to 50% of initial height at 20 minutes and followed by 23.5% at 40 minutes, and then leveled off for the rest of the observation (Fig. 4A). A representative of the topographic changes of selected target cellulose within 6 minutes was provided (Figure 4B) and Figure 4C represents the crosssection analysis the same position. We used the average height of the entire crosssection to plot the height changes curve. The resulted data combine the height changes with the width changes of the cellulose mirco-fibrills to generate a normalized volume changes which could be considered as the result of enzymatic hydrolysis.

Considering the small experimental error of $\pm$ 3.5 nm, our results (Fig.4 A) suggest that this decay is related with the rapid decline of enzymatic hydrolysis. The height changes

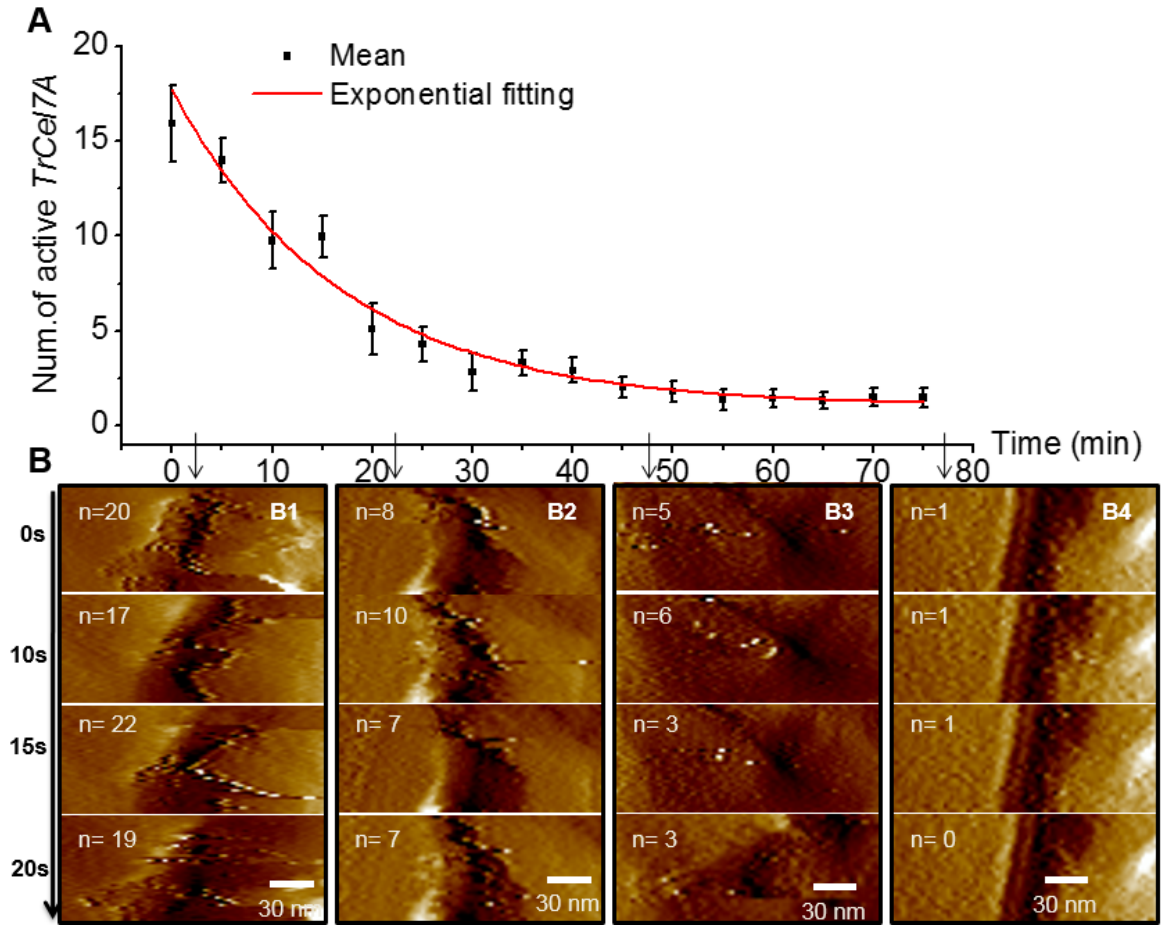

Figure 4.5 Time course of the surface density of active *TrCel7A* (50 μM) molecules bound on cellulose substrate in 50 mM sodium acetate buffer with pH 5.0 at 25 °C. The surface density of active *TrCel7A* has been calculated by a fixed observation area 150×50 nm^2.(A) Observed surface density of active *TrCel7A* declining during the continuously AFM observation and the average numbers of active *TrCel7A* were calculated as the expected value of Poisson distribution (Eq.1 and 2) . Error bars show standard deviation (SD) from the three independent measurements. The experimental data was fitted by an empirical decay function (Eq.3). (B) Example of AFM dynamic observations on different reaction time points: 3 min (B1), 23 min (B2), 46 min (B3) and 76 min (B4), respectively. The numbers of active *TrCel7A* on each AFM frame were counted manually and used as the raw data for calculate the parameter of Poisson distribution

observed in the current experiments are consistent with the previous results obtained from bulk bioanalytical assays, which measured the concentration of the hydrolysis product and suggested that the hydrolytic rate of *TrCel7A* had a rapid exponential decay in the initial binding stage, and that these enzymes become inactivate and reduced the enzymatic hydrolysis rate [83][97][98]. In fact, swelling also induces the topography changes of cellulose micro-fibrils. The swelling event is a relatively slow process as water molecules penetrate the space between adjacent cellulose chains, causing a reconfiguration of the intermolecular hydrogen-bond network and resulting in the expansion of the microfibrils. However, it is well established that the hydrolysis dominates the topography changes at the initial stage, and swelling comes in at a later stage [99]. The observation time course in the experiment runs from 90 to 120 minutes which could be considered as a period dominated by hydrolysis. In addition, *TrCel7A* (unlike Cel7B (also known as endoglucanase I (EGI) which can cleave internal bonds and create new chain ends)) is unlikely to introduce the water molecules into the exposed hydrophilic structure of the inner para-crystalline cellulose chains, which may trigger the swelling of cellulose micro-fibrils14, thus the height changes caused by swelling is negligible when only *TrCel7A* has been involved into the enzymatic reaction.

4.4.5 The Hydrolytic Rate is Dependent on the Density of *TrCel7A* Molecules on the Cellulose Substrate

This is the first time that the well documented drop of hydrolysis rate is observed at single molecular level. Via video-rate AFM, we observed that hydrolysis reaction reduces the height of cellulose molecules (Fig. 4.6A). Consistent with the drop of hydrolysis rate, the height changes of cellulose substrate get slower during the hydrolysis reaction. We used

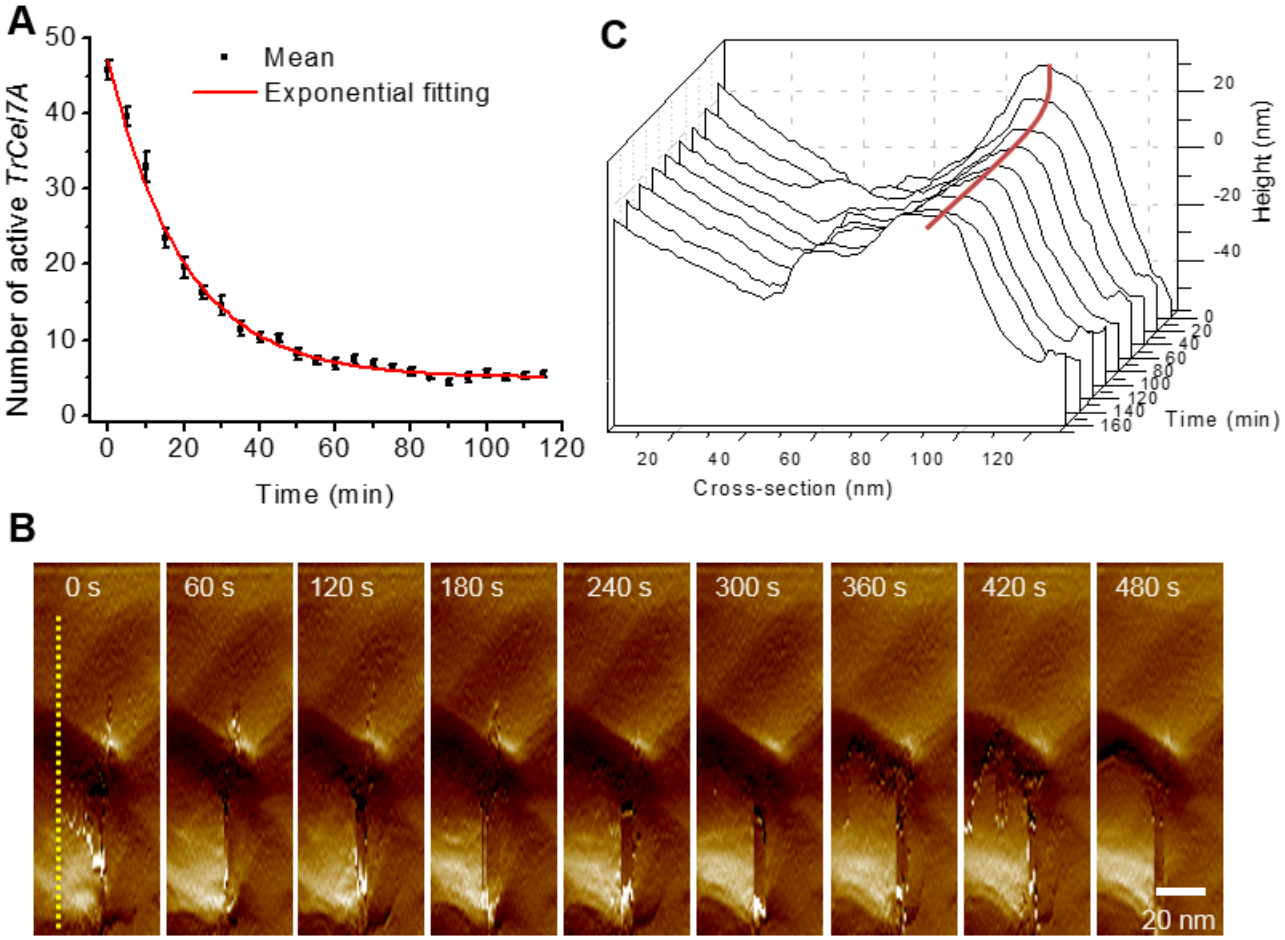

Figure 4.6 Time course of the density (number) of the topographic height changes of cellulose substrate interacted with *TrCel7A* (50 μM) in 50 mM sodium acetate buffer with pH 5.0 at 25 °C. (A) Observed height of cellulose surface declining during the continuously AFM observation. Error bars show standard deviation(SD) from the three independent measurements. (B) and (C) Example of AFM dynamic observations on cellulose surface monitoring during 480 seconds. (B) is the cross-section of (C) at various time spots. The position of cross-section is marked with dash line on (C)

an empirical exponential decay function (Eq.3) to fit the experimental data, and the decay constant is 0.0592. The density of *TrCel7A* on cellulose substrate also reduces during the hydrolysis reaction. The exponential decay constant is 0.0503, at the same scale of that of the reduction of height changes of the cellulose substrate, which indicates the hydrolysis reaction rate. We thus hypothesize that the rapid declining of enzymatic hydrolysis rate is related with the density of *TrCel7A* on the cellulose substrate, and next we will compare our results and the ones existed in literature.

(i) Inhibition of *TrCel7A* by hydrolysis product: cellobiose [100]. In order to figure out if the product inhibition is a dominating factor for hydrolysis rate declining, we designed a continuous experiment using the same substrate (cellulose) and same buffer with continuous addition of *TrCel7A*. During the observation, we added *TrCel7A* at the time points of 0 minute, 120 minute and 240 minute. The surface density of active *TrCel7A* and height changes of substrate have been measured using AFM imaging frames. After adding *TrCel7A* to the imaging buffer, the concentration of hydrolysis product increases during the entire experiment. However, the hydrolysis rate (cellulose height changes) and surface density of active *TrCel7A* remained the same trends (Fig. 4.7) as those in experiments describe in previous section. This suggests that the hydrolysis products cannot inhibit the reaction of cellulose and *TrCel7A* or at least is not a dominating factor for the rate declining. In addition, Converse et al. showed that the hydrolysis rate remained in declining trend when the products were removed during the reactions [101].

(ii) The cellobiohydrolases becoming stuck or jamming on the substrate surface due to a crystalline defect [102][103][104]. From the time course study, we did observe the *TrCel7A* molecules jamming. Since the hydrolysis rates were independent of enzyme to substrate ratio (Fig. 4.7), jamming of *TrCel7A* on cellulose surface is not a primary reason for decreasing

hydrolysis rate . In addition, jamming of enzyme molecules lasted only for a short period before it was broken down and *TrCel7A* molecules came back to free movement. These results suggested that the enzyme jamming is a locally transient state of enzymatic hydrolysis, and it is less likely to affect the overall hydrolysis rate.

(iv) Non-productive binding of adsorbed enzyme [98]. Binding of the intact *TrCel7A* only through CBD results in a non-productive binding, where the cellulose chain is not in the active site. According to the experimental results of this study, the non-productive binding *TrCel7A* molecules were also observed as immobilized enzymes. However, compared with active *TrCel7A*, it only accounted for less than 5% of the total number of observed enzyme molecules. Based on concentration analysis, Jalak and Valjamae [98] suggested that the surface density of active (productive) enzymes did not change during the hydrolysis process, and some *TrCel7A* was inactivated on a substrate surface to become non-productive binging enzymes while other active *TrCel7A* could proceed freely along the cellulose surface. However, in our results, the surface density of active *TrCel7A* molecules decreased over time. The difference between their and our results is likely due to the different observation methods. Jalak and Valjamae [98] used para-nitrophenol--D-lacto side (pNPL) as a reporter molecule to measure the concentration of non-productive *TrCel7A* molecules by binding to their active sites. However, since the pNPL molecules is also involved in the hydrolysis reaction, the measured concentration of productive/non-productive enzymes could be interfered by additional pNPL. It is not easy to rule out the possibility that pNPL may affect the hydrolysis of cellulose. Moreover, it is known that the cellobiose, the product of *TrCel7A* hydrolysis, is a strong inhibitor of the hydrolysis of pNPL [105], which makes pNPL an unstable reporter molecule during the *TrCel7A* hydrolysis process. The results proposed in this study tried to use single molecule in situ to measure directly the hydrolysis behavior of *TrCel7A* which

should be more accurate.

(v) Inactivation of enzyme through irreversible binding to cellulose [106]. The experimental results of this study support this hypothesis quite well. The time course study of the surface density of active *TrCel7A* (Fig. 4.5) and the hydrolysis rate by examining the height reduction (Fig. 4.6) suggested a temporal correlation of the declining in hydrolysis rate with the decrease of surface density of active *TrCel7A*. A detailed analysis of the density of active *TrCel7A* and hydrolysis production showed a similar time constant in the two decay curves ($b_{TrCel7A} = 0.0592 and b_height = 0.0503$).

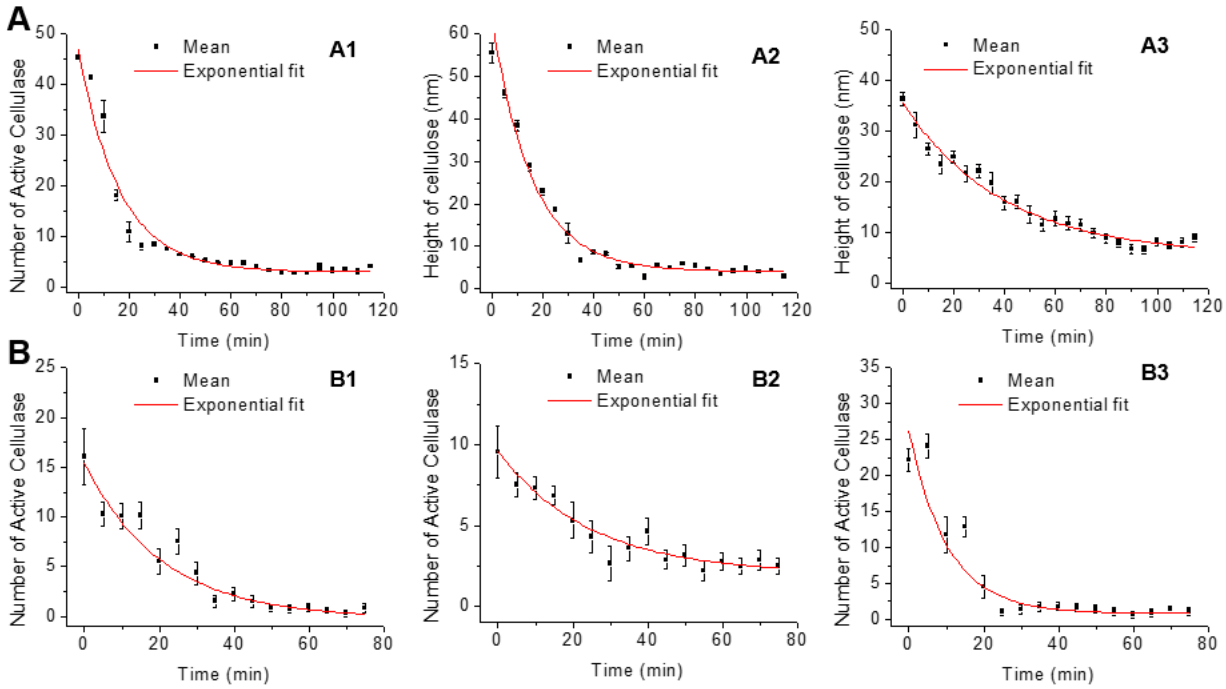

Figure 4.7 Time course comparison of the surface density of active *TrCel7A* molecules (A) and the topographic height changes of cellulose substrate (B) during the continuous addition of *TrCel7A*. 50 μM of *TrCel7A* was added at time point 0 min, 120min and 240 min. Both the cellulose substrate and imaging buffer (50 mM sodium acetate buffer with pH 5.0 at 25 °C) were stayed the same throughout the length of entire time period. The surface density of active *TrCel7A* has been calculated as the expected value of Poisson distribution (Eq.1 and 2). Error bars show standard deviation (SD) from the three independent measurements

Because the enzymatic hydrolysis involves the soluble enzyme and insoluble substrate,

each single enzyme should be able to bind and act at the solid-liquid interface. CBD is thought to enhance the hydrolysis efficiency of the insoluble substrates via increasing bound enzyme concentrations [106]. Enzyme binding reversibility has been the focus of numerous studies but the results are often controversial. In some studies full reversibility was observed [107][108], which can be the adaption of the Langmuir model; whereas others reported significant irreversibility [109][110]. However, our results suggested a time variation on the surface density of bound enzyme that occurred during the enzymatic hydrolysis which contradicts the assumption of Langmuir model of constant equilibrium and adsorption capacity. It may come out with the conclusion: for *TrCel7A*, each binding may not be equivalent and there may exist some uncertain interaction between adsorbed molecules on adjacent sites. Some other factors such as enzyme half-life period may also affect the hydrolysis rate. The half-life parameter is related to the time period that single molecular stays on the surface of cellulose surface . Although the thermal deactivation (which affect the half-life period of processive hydrolysis) also contributes the slow hydrolysis rate, the enzyme deactivation is likely to be the first order decay [104]. Compared with the density of active enzyme molecules, which has been shown as exponential decay in this study, the half-life parameter is less likely to be a dominated factor for rapid decay of hydrolysis rate. We did not observe the initial state of binding with increasing binding and activity increase simultaneously as reported in some researches [111], while our results indicated that the decline of the surface density of *TrCel7A* started right after the addition of *TrCel7A*. This result is consistent with the experimental result of Ma et al., who used a UV-spectral method to estimate the adsorption behavior of *TrCel7A*7. However, we cannot discount the suggestion of initial binding increase, since our technique is not fine enough to resolve a temporal phenomenon within several tens of seconds after the onset of reaction.

4.5 Conclusions

In this research, we studied the enzymatic hydrolysis of cellulose nano crystal nanofibrils by using an AFM to dynamically observe the enzymatic hydrolysis process. We used a scan strategy–prior knowledge based compressive scan to improve the imaging rate of AFM high enough to capture the moves of *TrCel7A* on cellulose surface. During the enzymatic hydrolysis, only the active *TrCel7A* could be considered as the "effective enzyme", based on the visualized information of time course study on single molecule *TrCel7A*, the surface density of effective enzyme significantly decreased along with the declining of hydrolysis rate, which is also independent of the concentration of cellulose and products, respectively. This suggested that the surface density of active *TrCel7A*, is the dominate factor that caused the inactivation of enzyme during the hydrolysis process. Nevertheless, we did not rule out the possibility that the declined hydrolysis rate may also be correlated with the half-life time changes of the bound enzyme. Considering the dramatical declining of the density of active enzyme, enzymatic half-life time changes is unlikely to be the main reason that caused the declined hydrolysis rate. Further improvement on AFM with faster imaging speed would be helpful to accurately estimate the moving velocity of *TrCel7A* and calculate the processive parameters such as kon, k_{off} and k_{cat}, would be helpful to have a more comprehensive understanding of enzymatic inactivation. Our results also suggest that the activation of CBD of *TrCel7A* seems to be suppressed during the hydrolysis, which may be an useful information for protein engineering study to increase the efficiency of enzymatic hydrolysis rate.

Chapter 5

Real-time Sensing of Electrical Properties in Nano Environment

5.1 Introduction

With the development of nano-materials, such as nanotubes and nanowires, the electrical characterization of these materials, attracted strong attention because of their unique electrical and thermal properties due to quantum confinement [112][113]. As a typical nano material, multiwall nanotubes (MWNTs) have intrinsic thermal and electrical properties [114], which are being considered as potential candidates for the next generation of circuit wires and nano electronic devices such as nano transistors [115][116], and sensors [26][25][29]. The carbon nanotubes can hold a current density as high as 10^9 A/cm^2 (which is more than 1000 times greater than copper) [117], and the thermal conductivities is higher than 3000 Wm^{-1}K^{-1} [118]. However, the thermal and electrical properties of the MWNTs are not fully understood, especially for the electrical breakdown.

An MWNT consists of many layers of single-wall nanotubes, and each of them has a various mechanical, electrical and thermal properties. Electrical breakdown is possible to be well controlled to peel the outer layers of MWNT or tailor its structure, in order to change the properties of MWNT [119]. The electrical breakdown determines the maximum current transport through the MWNTs circuit, and it is also considered as an approach to

fabricate high performance sensors and transistors. It is essential to understand the electronic properties of the material prior to designing a high performance nanodevice. Generally, the electrical breakdown is caused by Joule heating produced by the electron flow in the layers of MWNT [120][121]. In practice, however, the reasons for electrical breakdown become various if environmental conditions are considered, such as energy dissipation to the electrodes, heat sink effect of substrate, local heating and oxidation. Although electrical breakdown is known as an issue for the applications of interconnects, it also can be considered as an approach to change local mechanical and/or electrical properties which could be more valuable than regular MWNTs for the applications of MWNTs based sensors and transistors.

It has been widely accepted that the electrical breakdown is caused by Joule heating [122]. In words, the electrical breakdown is expected to be happened in the center of a suspended MWNT. However, some studies observed converse results: electrical breakdowns are not always happened in the center, sometime it locates apart quit a long distance to the middle [123]. In such a condition, the structural defect of MWNT (which could reduce the local conductivity) was considered as the major reason that leads to the electrical breakdown [124]. Besides structural defect, local conductance change, such as diameter variation from one end to the other, also determines the position of electrical breakdown [125].

The motivation of present research is to find the crucial factors that affect electrical breakdown, and make the electrical breakdown controllable. Controllable electrical breakdown is studied utilizing atomic force microscopy (AFM) based nano robot. The AFM based nano robot is a special and useful technological device to image the nano structures, and to conduct local manipulations on nano materials [70][69][71]. The sharp AFM tip (apex is approximately 10 nm or less) can be considered as an end effector of the nano robot, which can measure and manipulate samples in nano scale. In this research an AFM based nano robot

is used to measure the local conductivity of MWNT, and manipulate its spatial structure to control the location of the heat sink, which makes electrical breakdown controllable.

The non-vector space control comes from a general framework called mutation analysis for set evolutions, which is proposed by Aubin [126]. Mutation analysis provides a natural way to describe various physical phenomena because some objects such as shapes and images are basically sets. Since the introduction of mutation analysis, it has been investigated in both theory and applications. On the theory side, it has been recently extended to obtain the viability theorem for morphological inclusions [127] and the general morphological control problems with state constraints [128]. On the application side, it has been applied to image segmentation [129], visual servoing [130], and surveillance networks [131].

The visual servoing using mutational analysis is proposed by Doyen in [130]. Nevertheless, possibly due to its abstract nature, no further extensions are performed afterwards. In this research, we try to extend the results and apply the method to nanoscale motion control. The major extension can be summarized in three aspects. First, the general framework for the non-vector space control is established in this research which is not discussed in Doyen's work. Second, the original formulation only deals with binary images, while in this research, gray scale images are considered. Third, the controller design is performed for a system describing the nanoscale motion control. Consequently, the controller is different from the one in [130].

In order to design a system which can solve the issue: how to get accurate motion control without introducing extra noise, we do not use extra sensors for generating SPM scanner position feedback. Instead of sensors, we use the SPM images as both the input and feedback to generate a closed-loop control for tip motion control in the nanomanipulation system. In this research, we developed a novel control strategy by utilizing the feedback/compressive

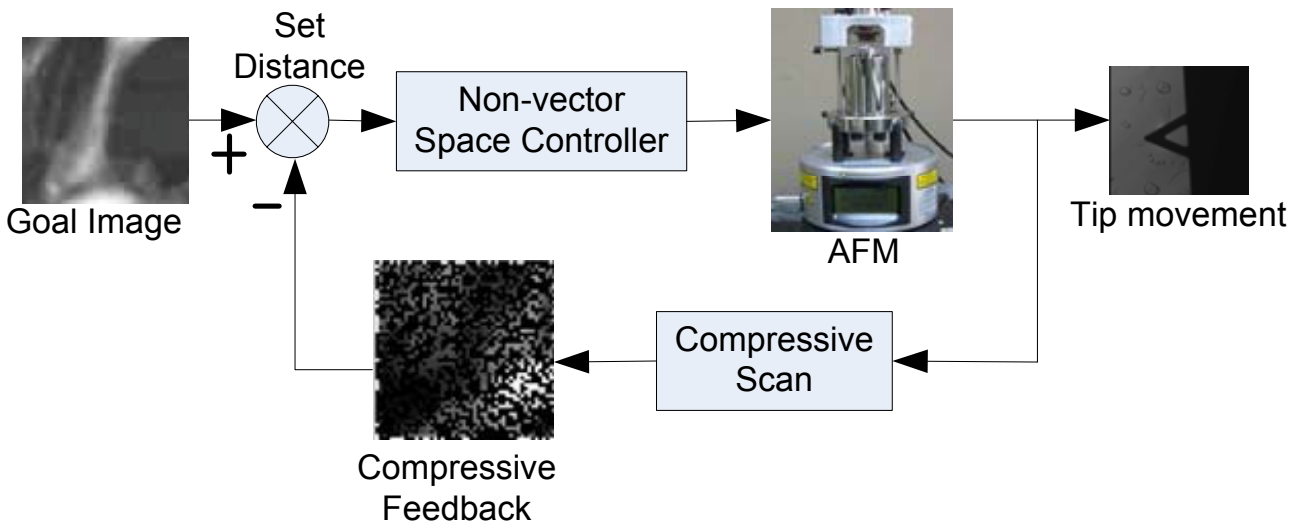

Figure 5.1 Control diagram of the non-vector space control system with compressive feedback (AFM as an example)

feedback produced by images/compressive data. Because the image or compressive feedback is a set, not a vector, from which comes the term *non-vector space control*, and in addition, the feedback can be full local image or partial image that can be considered as compressive data, from which comes the term *compressive feedback*. Inside this control system, both the controller design and feedback are based on the non-vector space for tip motion control to conduct nanomanipulation on SPM (as shown in Fig. 5.1). Three crucial steps in this strategy are as follows: (1) Design a non-vector space controller in which the local image is used directly as the feedback. (2) Using compressive scanning to compressed sample and reconstruct local image. Compressive sensing is introduced here for reducing the scanning time to increase the feedback rate. (3) Replace complete feedback (local image) with compressed data directly to generate a compressive feedback (as shown in Fig. 5.1). In this step, we designed a non-vector space controller based on compressive feedback. After compressive scanning, it is not necessary to recover the local image that costs extra time on calculation. The compressive data obtained by compressive scanning is used directly as the feedback of

this non-vector space controller. This is the challenge. In such a case the controller must ensure the stability when the compressed data is used as the feedback of closed-loop control. In this research we will use AFM as a specific example to illuminate how non-vector space controller works. In addition, an AFM based nanomanipulation applications: carbon nanotube conductivity mapping using non-vector space control will be introduced at the end of this report.

5.2 Accurate Position Control in Nano Environment

5.2.1 Non-vector Space Control based on Local Image

A non-vector space control strategy based on local image is proposed in this section. A local image is obtained by scanning locally (the local scan only samples a small area of interest and sampling time can be reduced so that an acceptable feedback rate is achievable) [49].

In the conventional visual servoing approaches, several of features are firstly extracted from the image followed by a controller which is designed to converge position error between desired and current vectors of features to zero [50]. Traditional visual servoing relies on feature extraction, and in most visual servoing literatures, several fiducial markers are used for features so that the tracking of them can be easily achieved [132].

Different from the above traditional servoing methods, we developed a featureless method that directly use the image intensity information. First, our method considers the image as a set. Second, we defined the difference between sets as the error between the desired and current image set. Finally a non-vector space controller is designed to converge the difference to zero [133]. This method is recently applied to nanomanipulations [134]. It should be noted that other featureless methods also exist, including the kernel based method [52], the sum-of-

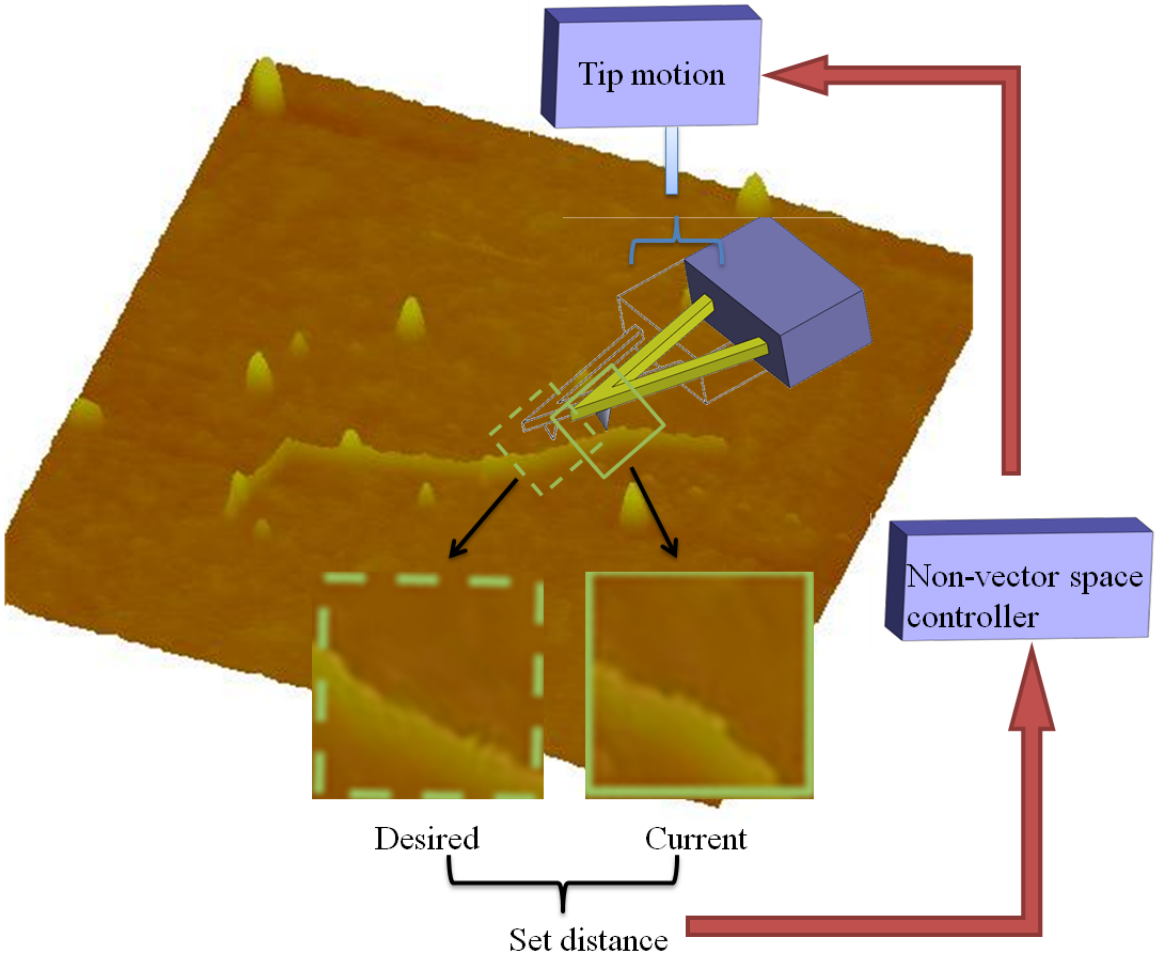

Figure 5.2 Basic working approach of non-vector space control

square-difference method [135][54], and the entropy based method [136]. But our approach is fundamentally different from them. Although the controller design in above applications was performed in non-vector space in which the linear structure in vector space does not exist, the dynamic models are still in vector space. It brought more difficulties in the theoretical analysis and design work of the control systems. In our approach, both the dynamics model and the controller design are in non-vector space.

The basic non-vector space control strategy is shown in Fig. 5.2. First, a large area of interest is scanned by SPM. Then a small image patch is chosen as the desired image (inside the large area SPM image). Then the tip starts the local scanning to obtain the

current image. Based on the two sets corresponding to the desired image and current image, the non-vector space controller calculates the moving direction for the SPM tip. Through updating current images, eventually the desired image is totally the same with current image. By this way, the tip can be steered to the desired position for manipulation. This strategy is completely different from current visual servoing methodology. This is because that although image is also used in visual servoing, image itself is neither the input nor the feedback. In visual servoing, image is used for recognizing features or landmarks which are used for locating the position. Some other methods such as optical flow [137] which could also be used in visual servoing. However, optical flow methodology works in vector space, and in other words image is a vector (not a set) to optical flow method. In this case, this kind of method also need dedicated calibration before applying, which is very difficult in nano world.

In order to design such a control system (mentioned above), two fundamental issues need to be solved: how to define a difference (distance) in non-vector space; how to build a dynamic model in the non-vector space. The non-vector space controller is based on the set, and if we want to solve the these issues, mutation analysis should be used to build the dynamics model in non-vector space [134].

5.2.1.1 Essentials of Mutation Analysis

In order to formulate the difference between two sets, the set distance should be defined. Any set distance $d(X, Y)$ between sets X and Y must satisfy following three conditions [138].

(1) Non-negative: $d(X, Y) > 0$ if X is not the same with Y; $d(X, X) = 0$;

(2) Symmetry: $d(Y, X) = d(X, Y)$;

(3) Triangular Inequality: $d(X, Z) \leq (X, Y) + d(Y, Z)$ for any other set Z.

Any set distance which satisfies these three conditions could be applied in non-vector space control system. In this research we use Hausdorff distance as an example to discuss the controller design and stabilization problem.

Given a finite set of points $P \in \mathbb{R}^n$, the set distance between the set P and a point $x \in \mathbb{R}^n$ is $d_P(x) = \min_{y \in P} ||y - x||$. The projection from x to P is denoted as $\Pi_P(x) = \{y \in P : ||y - x|| = d_P(x)\}$. The Hausdorff distance of two sets P and Q is defined as:

$$dh(P, Q) = \max \{\max_{p \in P} \min_{q \in Q} ||p - q||, \max_{q \in Q} \min_{p \in P} ||q - p||)\} \tag{5.1}$$

Follows are some extra definitions for defining the set dynamics. A tube $K(t) \subset \mathbb{R}^n$ is a mapping: $K : \mathbb{R}^+ \mapsto 2^{\mathbb{R}^n}$, where $2^{\mathbb{R}^n}$ is the powerset of $\mathbb{R}^n$. Let $\varphi : E \mapsto \mathbb{R}^n$ with $E \subset \mathbb{R}^n$ be a bounded Lipschitz function. Denote the set of all such functions as BL(E, $\mathbb{R}^n$). The transition for $\varphi \in$ BL(E, $\mathbb{R}^n$) is defined as:

$$T_\varphi(t, K_0) = \{x(t) : \dot{x} = \varphi(x), x(0) \in K_0\} \tag{5.2}$$

which can be considered as a tube evolving under the rule of φ. The derivative of the tube, based on mutation analysis, must satisfy the following condition:

$$\lim_{\Delta t \to 0^+} \frac{1}{\Delta t} dh(K(t + \Delta t), T_\varphi(\Delta t, K(t))) = 0 \tag{5.3}$$

$$\mathring{K}(t) = \{\varphi(x) \in \text{BL}(E, \mathbb{R}^n) : \text{Eq. (5.3) is satisfied}\} \tag{5.4}$$

Therefore, the set dynamics mutation equation is defined as follows:

$$\varphi(x) \in \mathring{K}(t) \tag{5.5}$$

In addition, the controlled mutation equation (let U be the set of all the possible controls u) is defined as:

$$\varphi(x(t), u(t)) \in \mathring{K}(t) \quad \text{with} \quad u(t) = \gamma(K(t)) \tag{5.6}$$

where $\varphi : E \times U \mapsto \mathrm{BL}(E, \mathbb{R}^n)$ is a mapping process from a state to a bounded Lipschitz function. $\gamma : 2^{\mathbb{R}^n} \mapsto U$ is the feedback map from current set $K(t)$ to the control input.

5.2.1.2 Mutation Analysis for Nanomanipulation

Mutation analysis is an alternative way to solve a visual servoing problem: design a controller $u(t) = \gamma(K(t))$ based on current images $\hat{K(t)}$ so that $dh(K(t), \hat{K}) \to 0$ as $t \to \infty$, where $K(0)$ and $\hat{K}$ are an initial (first current) and goal (desired) image sets respectively,

In fact, if the function φ in Eq. (5.6) is linear in $u(t)$, we have the following theorem [133, 134]: For the system described by mutation equation $L(x)u \in \mathring{K}(t)$ with $x \in \mathbb{R}^m$, $L(x) \in \mathbb{R}^{m \times n}$, $u \in \mathbb{R}^n$, and $K(t) \subset \mathbb{R}^m$, the following controller can be locally exponentially stabilized at $\hat{K}$:

$$u(t) = \gamma(K) = -\alpha A(K)^{+} V(K) \tag{5.7}$$

where $\alpha > 0$ is a gain factor. $A(K)^{+}$ is the Moore-Penrose pseudoinverse of $A(K) \in \mathbb{R}^{1 \times n}$

defined by:

$$A(K) = \int_K d^2_{\hat{K}}(x) \sum_{i=1}^{m} \frac{\partial L_i}{\partial x_i} dx + 2 \int_K [x - \Pi_{\hat{K}}(x)]^{\mathrm{T}} L(x) dx$$
$$- 2 \int_{\hat{K}} [x - \Pi_K(x)]^{\mathrm{T}} L(\Pi_K(x)) dx$$

where $L_i \, (i = 1, 2, \ldots, m)$ is the $i - th$ row vectors in matrix L. $V(K)$ is the Lyapunov function defined as:

$$V(K) = \int_K d^2_{\hat{K}}(x) dx + \int_{\hat{K}} d^2_K(x) dx \tag{5.8}$$

In nanomanipulations, the SPM can be considered as an imaging device with two translational degree-of-freedom (vertical motion is used to obtain the sample topography). If the control input is $u = [u_x, \, u_y]^{\, T}$, the mutation dynamic equation is:

$$Lu \in \mathring{K}(t) \tag{5.9}$$

where

$$L = \begin{bmatrix} -1 & 0 \\ 0 & -1 \\ 0 & 0 \end{bmatrix}$$

is a constant matrix. In this case, the controller can be obtained from Eq. (5.7):

$$u(t) = -\frac{\alpha}{2} \{ \int_K [x - \Pi_{\hat{K}}(x)]^{\mathrm{T}} L dx + \int_{\hat{K}} [x - \Pi_K(x)]^{\mathrm{T}} L dx \}^{+} V(K) \tag{5.10}$$

5.2.2 Compressive Sensing for Visual Servoing

In the non-vector space control system, SPM images are used as the input. The input image here is not the entire image which costs too much time on scanning but the local image whose dimension is much smaller than the entire image. The local scan strategy [2] we developed could make the scanner scan in a small local area and get its topography image. However, it still take several seconds (actual time depends on local image size) to obtain a local image which is too slow for providing feedback for the non-vector space controller. In order to solve the low feedback problem, compressive sensing is introduced.

Considering an unknown signal $x \in \mathbb{R}^N$, if M linear measurements are taken according to a measurement matrix Φ (as shown in Eq. (5.11), in the case of $M = N$, the original signal x could be well sampled. However, we are more interested in the condition when $M \ll N$: fewer measurements might be enough for reconstructing the original signal.

$$y = \Phi x \tag{5.11}$$

where Φ is the measurement matrix and y is the measurement results which $y \in \mathbb{R}^M$. Eq. (5.11) is an under-determine equation if $M \ll N$-impossible to find a unique solution. However, if adding some constraint such as that x is sparse and Φ has been properly designed, the optimization solution of x can be found by solving the 0-norm minimization problem [64].

$$\hat{x} = \arg\min ||x||_0 \quad \text{s.t.} \quad \Phi x = y \tag{5.12}$$

Because solving the 0-norm minimization problem is NP-hard [66, 139], 1-norm mini-

mization is used to instead of 0-norm. Then the Eq. (5.12) could be written as

$$\hat{x} = \arg\min ||x||_1 \quad \text{s.t.} \quad \Phi x = y \tag{5.13}$$

where $\hat{x}$ is the reconstructed signal.

Besides the 1-norm minimization algorithm, minimization total variation method (Eq. (5.14)) is used for signal reconstruction. It can find the sparest solution in intensity gradient level to obtain a continuous and smooth reconstructed image.

$$\hat{x} = \arg\min TV(x) \quad \text{s.t.} \quad \Phi x = y \tag{5.14}$$

where $TV(x) = \sum_{i,j} \sqrt{(x_{i+1,j} - x_{i,j})^2 + (x_{i,j+1} - x_{i,j})^2}$.

Because compressive sensing can fewer measurements, we can use it associated with our local scan strategy to increase the feedback rate by further decreasing the scanning time. How to design a proper measurement matrix is a challenge facing to the implementation of compressive sensing into SPM. Usually compressive sensing uses random measurement matrixes such as random Gaussian and Bernoulli matrixes. It is difficult to apply these random measurement matrixes to SPM due to the special working principle of SPM. The working principle of SPM is using a tip to scan on top of sample surface line by line which is a time consuming work.

The measurement matrix in compressive sensing is an essential part due to the relationship between the measurement matrix and measurement efficiency. According to the Restricted Isometry Property (RIP) [64], random matrixes usually leads to the totally reconstructed original signal.

In order to design a random measurement matrix for SPM, the physical meaning of the

measurement matrix in SPM imaging should be studied first. Measurement matrix is the SPM scanning trajectory. The tip scanning trajectory is determined by measurement matrix. However, because of the working principle of SPM, we have to find a continuous trajectory for random sampling points which can connect all the points and only visit once. This is a typical traveling salesman problem (TSP) which is a NP-hard problem. In order to find a near optimal solution for this trajectory, the Genetic Algorithm (GA) which is a paradigm based on crossover and mutation is used for solving this problem [67]. The working principle of this algorithm is that it connects each of the two points and then randomly selects the position to cut the connection between two points. Through the methods of recombination, mutation and selection, GA could search a new generation points which is better (shorter traveling distance) than the former trajectory. For example, we set the local area with 50×50 points, and after GA was applied, the trajectory is obtained as shown in Fig. 2.2. The red line denotes the trajectory of the SPM tip which visits each point once and eventually returns to the initial point with the travel distance 981.1645 (assume the distance between two neighbor points is one). It is much shorter than raster scanning the entire local area (total distance is 2500). By means of compressive sensing, we can directly save the time spent on scanning which can increase the image feedback rate.

5.2.3 Non-vector Space Control based on Compressive Feedback

Although compressive sensing decreases the time spent on scanning, it still needs extra time (approximate 0.5 second for 30×30 image) for image reconstruction. In order to further increase the feedback rate, we extended the non-vector space controller to compressive feedback case instead of complete image feedback.

The derivation is similar to the case of complete image based non-vector space control

methodology which uses regular state feedback. The only difference from the approach in section 5.2 is the type of feedback. The feedback for former controller is a complete image recovered from compressive scanning. In contrast, for compressive feedback, the compressive data obtained by compressive scanning is used directly as the feedback without recovering process. In other words, the SPM scanner only scans partial points of local area. Based on this compressive data, a controller is designed to control the SPM's tip towards the desired position which is achievable if this process is performed repeatedly. It also should be noted that instead of the process of image recovering, we directly use it for feedback without recovery. In this case, the feedback rate can be increased.

5.2.3.1 Controller Design based on Compressive Feedback

Because the mutation equation is the same and the compressive feedback (data) is also a set, the controller in section 5.2 still works and it can be slightly modified as follows:

Let K_c and $\hat{K}_c$ be the sets obtained by random scanning/sampling from the current image and the desired image sets K, $\hat{K}$, respectively. Following controller can locally exponentially stabilize K_c at $\hat{K}_c$.

$$u(t) = -\frac{\alpha}{2}\{\int_{K_c}[x - \Pi_{\hat{K}_c}(x)]^{\mathrm{T}} L dx + \int_{\hat{K}_c}[x - \Pi_K(x)]^{\mathrm{T}} L dx\}^{+} V(K_c) \tag{5.15}$$

where $V(K_c) = \int_{K_c} d^2_{\hat{K}_c}(x)dx + \int_{\hat{K}_c} d^2_{K_c}(x)dx$, and the other variables are the same as previous section.

This controller might not meet the goal of $dh(K, \hat{K}) \to 0$ as $t \to \infty$. It possibly exists another set $\widetilde{K}$ where $\hat{K}_c \subset \widetilde{K}$, if the cardinality of $\hat{K}_c$ is much fewer than that of $\hat{K}$. To prevent such condition, we have to prove that when $dh(K_c, \hat{K}_c) \to 0$, $dh(K, \hat{K}) \to 0$, if

K_c satisfy some certain constrains. These constrains come from the compressive sensing technique. Intuitively, there should be a unique K given a randomly sub-sampled $K_c \subset K$. Assume that the image is S sparse in the frequency domain (Fourier domain in this research, the number of nonzero coefficients is S). If we sample the image pixel intensity in uniform random, the image can be exactly reconstructed by l_1 minimization algorithm if the number of samples is at the order of $O(S \log n)$.

5.2.3.2 Stability Analysis

Assume that the elements of set K is obtained in order from the image. For example, for an $n \times n$ image, the first n elements in K are the first row (or column) of the image. Let x_k be the k-th pixel of all the intensities of image set K, and the elements in x_k are obtained using the same order in K. Similarly, let $\hat{x}_k$, x_{k_c}, and $\hat{x}_{k_c}$ be the vector of all the intensities of $\hat{K}$, K_c, and $\hat{K}_c$, respectively. The following lemma is used to prove the stability of the controller.

Lemma 1 *$dh(K, \hat{K}) \to 0$ if and only if $||x_k - \hat{x}_k|| \to 0$*

(1) First of all, let's show $dh(K, \hat{K}) \to 0 \Rightarrow ||x_k - \hat{x}_k|| \to 0$. By the definition of hausdorff distance, if $dh(K, \hat{K}) \to 0$, then for any $p = [p_1, p_2, p_3]^{\mathrm{T}}$ in set K, we have $\min_{q \in \hat{K}} ||p - q|| \to 0$. Let $q = [q_1, q_2, q_3]^{\mathrm{T}}$ be the element in $\hat{K}$ when the minimum is achieved, then $(p_1 - q_1)^2 + (p_2 - q_2)^2 + (p_3 - q_3)^2 \to 0$. Because the first two coordinates in p and q are the pixel indices, $(p_1 - q_1)^2 + (p_2 - q_2)^2$ cannot approach zero if the indices are different. Therefore, $p_1 = q_1$ and $p_2 = q_2$ which means the order of p and q are the same in K and $\hat{K}$, respectively. Moreover, we have $(p_3 - q_3)^2 \to 0$. Consequently, we have $||x_k - \hat{x}_k|| \to 0$ since $||x_k - \hat{x}_k||^2$ is the sum of all the square of intensity differences for the same pixel indices such as $(p_3 - q_3)^2$.

(2) Second, let's show $||x_k - \hat{x}_k|| \to 0 \Rightarrow dh(K, \hat{K}) \to 0$. Let $p = [p_1, p_2, p_3]^{\mathrm{T}}$ in set K and $q = [q_1, q_2, q_3]^{\mathrm{T}}$ in set $\hat{K}$ be two arbitrarily elements with the same pixel indices, i.e., $p_1 = q_1$ and $p_2 = q_2$. Since $||x_k - \hat{x}_k|| \to 0$, we have $(p_3 - q_3)^2 \to 0$. Then for $p \in K$, we have $\min_{q' \in \hat{K}} ||p - q'|| \leq ||p - q|| \to 0$. For any other elements in K, we also have similar arguments. Therefore, $\max_{p' \in K} \min_{q' \in \hat{K}} ||p' - q'|| \to 0$. Similarly, we have $\max_{q' \in \hat{K}} \min_{p' \in K} ||q' - p'|| \to 0$. Therefore, $dh(K, \hat{K}) \to 0$.

Besides the lemma, another equation (RIP) from the compressive sensing literature is used to establish our result. First of all, we introduce the RIP condition for a matrix formally.

Definition 1 *A matrix $A \in \mathbb{R}^{m \times n}$ satisfies the RIP condition of order S if there exists a $\delta_S \in (0, 1)$ such that:*

$$(1 - \delta_S)||x||_2^2 \leq ||Ax||_2^2 \leq (1 + \delta_S)||x||_2^2 \tag{5.16}$$

for all the S sparse vectors $x \in \mathbb{R}^n$.

To test a matrix whether satisfies RIP condition is a exponential computational complexity problem. But random matrices have shown to satisfy the RIP condition with very high probability. In fact, we have the following lemma:

Lemma 2 *[140] Let $\Phi \in \mathbb{R}^{n \times n}$ be the spike basis and $\Psi \in \mathbb{R}^{n \times n}$ be the Fourier basis. Then the matrix $A = R\Phi\Psi^{-1}$ where $R \in \mathbb{R}^{m \times n}$ extracts m rows in $\Phi\Psi^{-1}$ uniformly in random. Then A satisfy the RIP condition of order S with very high probability if $m \geq C \cdot S \cdot \log^4 n$, where C is a constant.*

Based on the two lemmas, we can have the following proposition which verifies the correctness of using compressive feedback.

Proposition 1 *Assume $x_k \in \mathbb{R}^n$ and $\hat{x}_k \in \mathbb{R}^n$ are S sparse in the frequency domain, $x_{k_c} \in \mathbb{R}^m$ and $\hat{x}_{k_c} \in \mathbb{R}^m$ be obtained uniformly at random from the image set K and $\hat{K}$. If $m \geq 2 \cdot C \cdot S \cdot \log^4 n$, where C is a constant. Then with high probability, we can have $dh(K, \hat{K}) \to 0$ if $dh(K_c, \hat{K}_c) \to 0$.*

From the random sampling, we have $x_{k_c} = Ax_k$ and $\hat{x}_{k_c} = A\hat{x}_k$. It is noted that based on the assumption, the random sampling matrix is the same as Lemma 2. Therefore, from Lemma 2, $A \in \mathbb{R}^{m \times n}$ satisfies the RIP condition with order $2S$. Let the RIP constant be δ_{2S}.

Using lemma 1, we have $||x_{k_c} - \hat{x}_{k_c}|| \to 0$ from $dh(K_c, \hat{K}_c) \to 0$. Form the RIP condition, we have $||x_{k_c} - \hat{x}_{k_c}||_2^2 = ||Ax_k - A\hat{x}_k||_2^2 \geq (1 - \delta_{2S})||x_k - \hat{x}_k||_2^2$. Since $1 - \delta_{2S} > 0$, we have $||x_k - \hat{x}_k|| \to 0$. Based on Lemma 1 again, we have $dh(K, \hat{K}) \to 0$.

This propositions show that if certain conditions are satisfied, the same controller in Eq. (5.15) can be used under the the compressive feedback.

5.3 Experimental Implementation and Setup

5.3.1 Experimental Implementation on AFM

In order to validate the non-vector space controller design and test the performance of this control system, we implemented it into our AFM based nanomanipulation system (as shown in Fig. 2.3). An AFM (Multimode, Bruker-nano,CA) is used in this experiment. A computer with a haptic device, a real-time Linux system and DAQ cards are used in this nanomanipulation system. In addition, a signal access and control box is developed for acquiring the signal of topography information and inputting the control signal into the

AFM controller.

5.3.2 Experiment on Non-vector Space Control with Complete Image as Feedback

In this experiment, we validate the non-vector space controller with complete image as feedback using nanomanipulation system. In this experiment, a conventional AFM was used to obtain an image of 1024×1024 pixels on single wall carbon nanotube (SWNT) sample (scan size is $1.6 \times 1.6\ \mu m^2$). This is the working area of the non-vector space controller. We name this AFM image with "original image". Then AFM scanned locally to get a small pitch image of current position. After that, a position close to current position (approximate 56 nm away) was chosen as the desired position. The desired image can be easily selected in the original image. After calculations the non-vector space controller provides the translational velocity u_x and u_y. The current and desired images, with size of 30×30 pixels, are labeled in original image in Fig. 5.3(a).

Results are shown in Fig. 5.3(b), where the iteration means the steps that AFM tip travels to the destination. At approximate 50 steps the AFM tip eventually reached the desired position when the distance approached zero. Another thing should be noted here is that the error in steady state. Theoretically, the error should converge to zero as time going to infinite, however, in AFM application because the thermal drift and noise, the non-vector space control has to minimize the error provided by thermal drift and noise. This is the reason for why steady state error does not approach zero both in x and y directions.

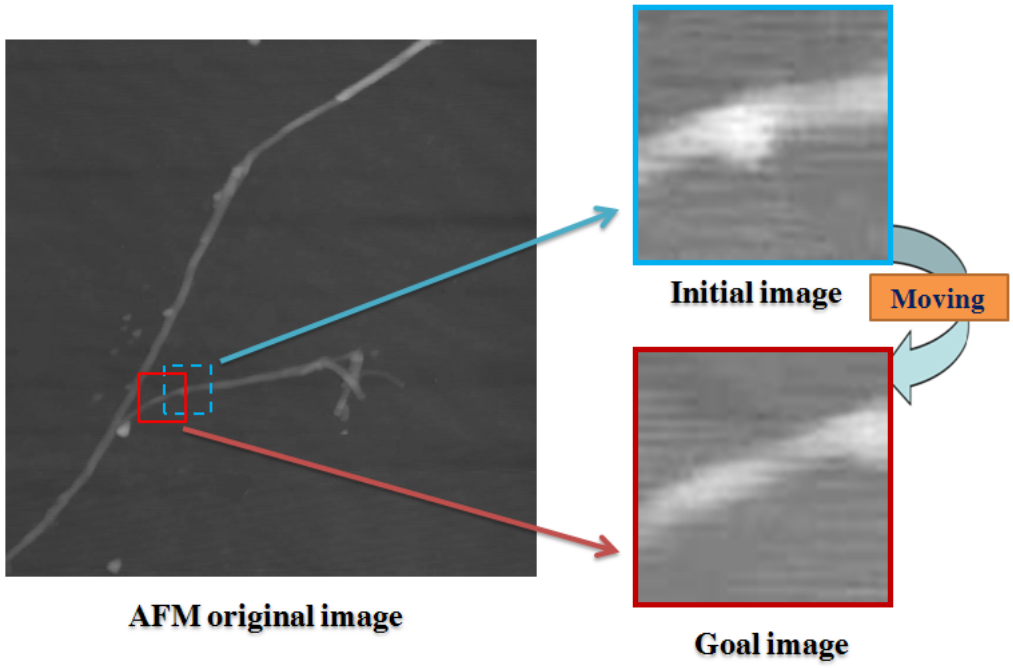

(a)

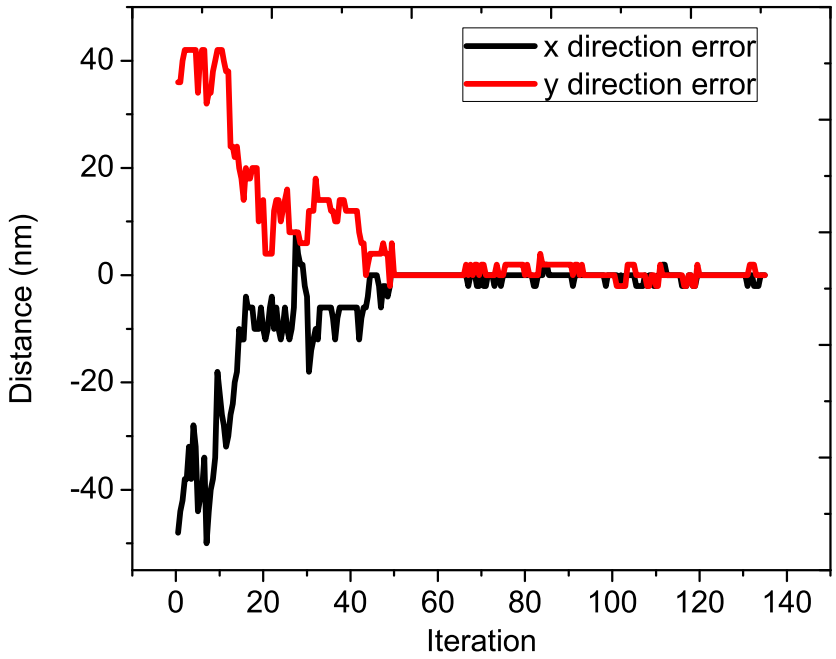

(b)

Figure 5.3 Experiment setup and results of non-vector space control based on compressive feedback (a): Experimental setup for the non-vector space control (b): Experiment results of non-vector space control with image as feedback: Error in x and y directions

5.3.3 Experiment on Compressive Sensing with Random Sampling

In the previous experiment, non-vector space control system obtained the image feedback by scanning the entire local area which spent much time. In order to reach a higher sampling rate, imaging speed must be geared up. That is the reason why compressive sensing is involved. The experiment results of compressive scanning and image reconstruction are shown in Fig. 5.4

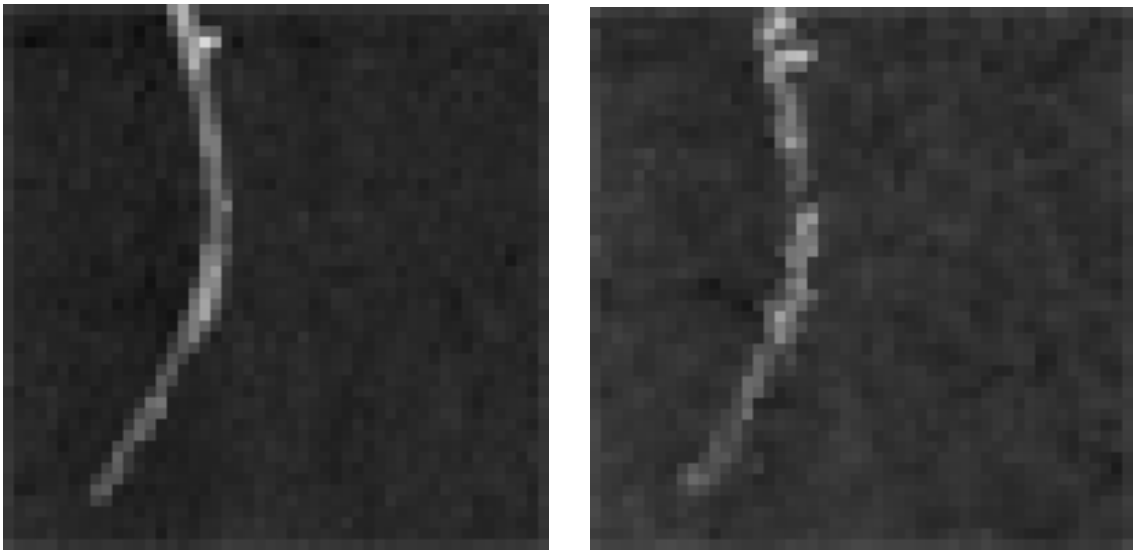

(a) (b)

Figure 5.4 Experiment results of AFM images reconstruction based on compressive sensing (a): Original AFM image of 50×50 pixels (b): Reconstructed image obtained by compressive sensing

These two images in Fig. 5.4 are 50×50 pixels and the scan size in each image is $1\times 1\ \mu m^2$ of DNA sample. After compressive sensing was applied, the scanning time decreased into 1.25 second (compared with 6.98 seconds in conventional raster scan). Compressive sensing can largely decreases the time spent on scanning. However, for compressive sensing, it still consumes time (approximate 1 seconds according to TV-norm reconstruction method)

to reconstruct the original image. In order to solve this new issue, we get rid of image reconstruction step, and use the compressive sampling data as the feedback to non-vector space controller directly.

5.3.4 Experiment on Compressive Feedback Non-vector Space Controller

From the previous experiment, it is shown that compressive sensing could increase the sampling rate without losing important data information. However, its disadvantage is also obvious: compressive sensing has to reconstruct the original image. A challenge comes out-whether we can directly use the compressive data which is not an image but a set of random chosen data (compressive data) to serve as the feedback. In Section IV, we showed the theoretical proof of this application. In this section, an experiment was setup for testing the performance of this control system. The experimental procedure is similar to the experiment with complete image as feedback. The only difference between these two experiments is that in this experiment we uses the compressive data obtained by compressive scanning instead of complete local image as the feedback. We used the same initial and desired locations with the first experiment. The distance between current position and desired position is 40 nm in vertical direction and -41 nm in horizontal direction.The feedback used in this experiment is a set of 350 elements (the ones inside 30×30 pixels as shown in Fig. 5.3(a)). The experiment result is shown in Fig. 5.5(b). In this experiment, initial and desired positions are just the same as the first experiment,but the calculation time spent on compressive feedback controller (0.152 s) is much smaller than the one use complete image as the feedback (0.322 s) in each step. That means the non-vector space controller based on compressive feedback

can largely reduce the time spent on both scanning and calculating.

5.3.5 Experiment on Tracking SWNT based on Compressive Feedback Non-vector Space Controller

The goal of this example is using AFM tip to track along SWNT. Before we started the AFM tip motion control, first a high resolution AFM image in the area of interest had been scanned as the original image (as shown in Fig. 5.6(a)) The scan size of image is $1.25 \times 1.25\ \mu m^2$ and the resolution is 1024×1024 pixels. Once the high resolution image was obtained, the path planner modules started working. The operator could select either automatically identify the SWNT and generate the tip path or manually design the arbitrary path. In this example the path was selected manually by using the haptic device, and the tracking path is shown in Fig. 5.6(b). Once the path was selected, the system automatically generated a sequence of images about the interim steps between start and end points (shown in Fig. 5.6(c)). With the guidance of non-vector space controller the AFM tip tracks the SWCNT and eventually reaches the goal position. In addition, the position error is shown in Fig. 5.6(d). The error is highly related to the image scan size and resolution. Generally, the smaller scan size with higher resolution, the less position error. In order to achieve ultra high accuracy position and motion control, we want to make the scan size as small as possible. However, this is a challenge when the scan size decrease into hundreds nanometers, especially for the local image or compressed data used for feedback. In this case the noise in image might influence the performance of controller. Typical Hausdorff distance is very sensitive to the noise; therefore, in this application, we use modified Hausdorff distance instead. The modified Hausdorff distance is defined as follows.

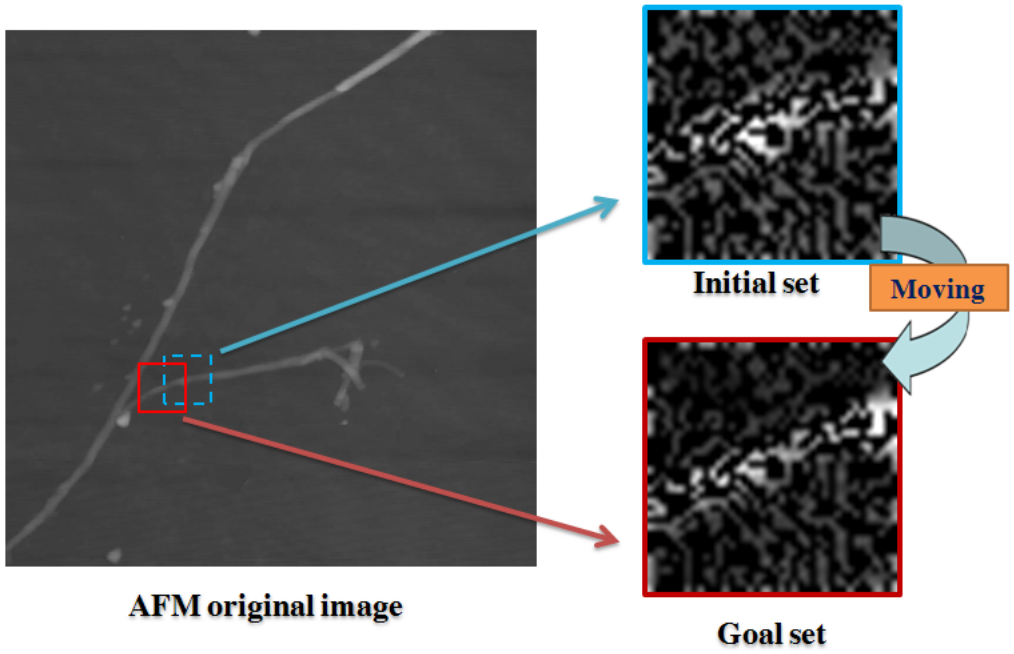

(a)

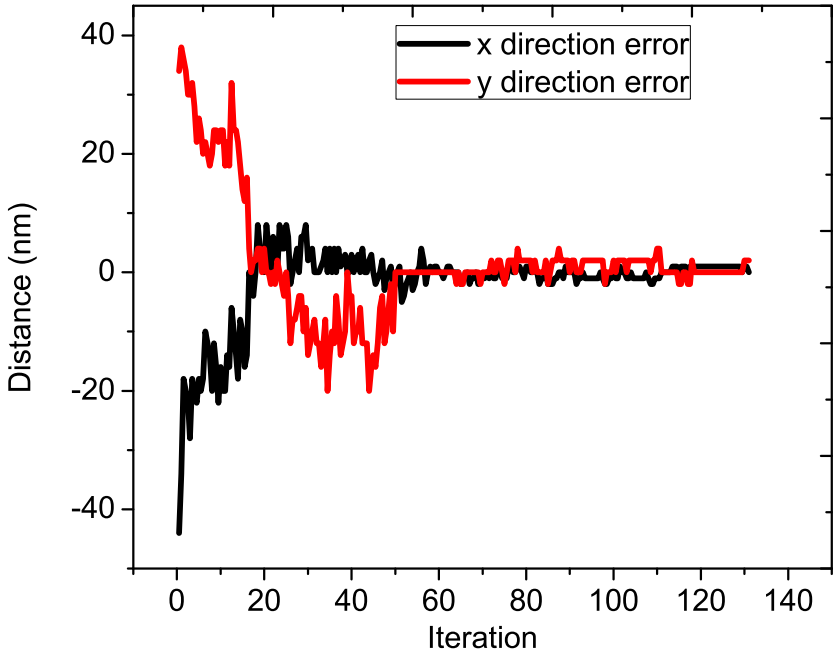

(b)

Figure 5.5 Experiment setup and results of non-vector space control based on compressive feedback (a): Experimental setup for the non-vector space control based on compressive feedback (b): Experiment results of non-vector space control with compressive feedback: Error in x and y directions

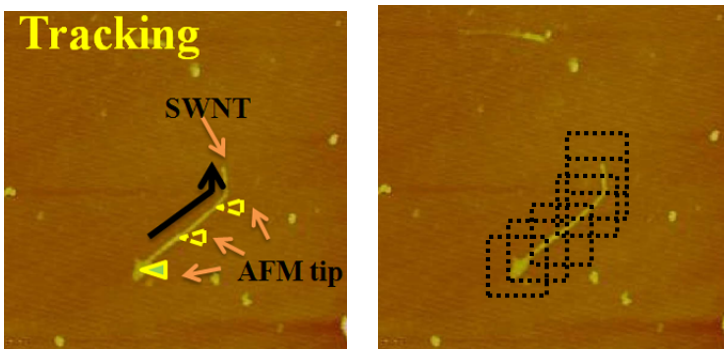

(a) (b)

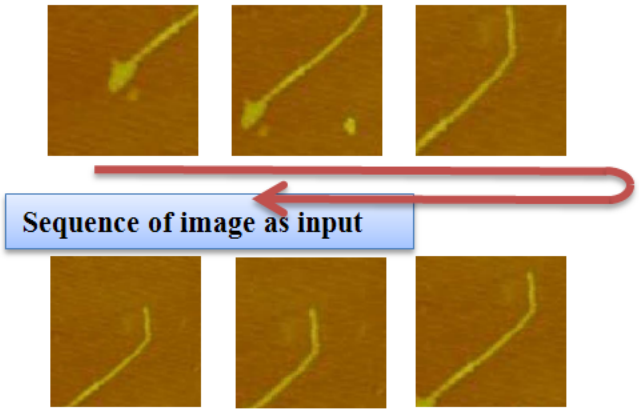

(c)

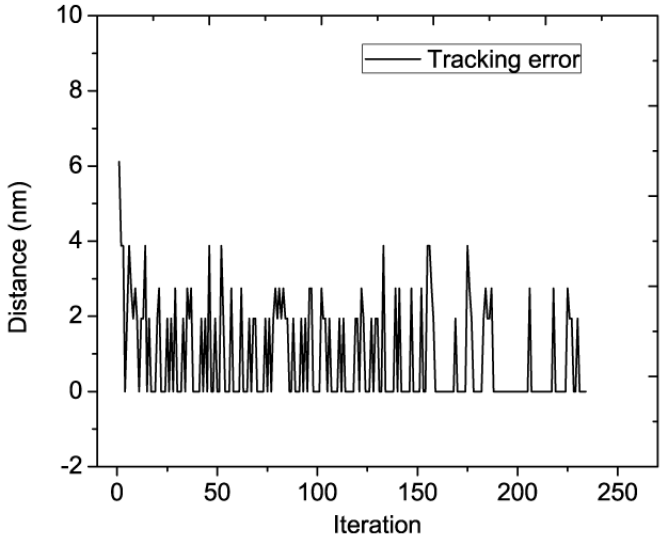

(d)

Figure 5.6 Experiment results of tracking SWCNT using non-vector space controller, (a): Original AFM image of 1024×1024 pixels, (b): Tracking path, (c): A sequence of image feedback, (d): Position error during tracking

Given a finite set of points $P \in \mathbb{R}^n$, the distance between a point $x \in \mathbb{R}^n$ and the set is $d_P(x) = \min_{y \in P} ||y - x||$. The projection from x to P is the set of points denoted as $\Pi_P(x) = \{y \in P : ||y - x|| = d_P(x)\}$. Consider two set P and Q, the Modified Hausdorff Distance (MHD) is defined as:

$$dh(P, Q) = \frac{1}{m} \sum \{\max_{p \in P} \min_{q \in Q} ||p - q||, \max_{q \in Q} \min_{p \in P} ||q - p||)\} \tag{5.17}$$

The MHD is robust to the noise, which is suitable in this example. After MHD was applied into the non-vector space controller, the error range was controlled within 4 nm. The method to verify position error in all experiments is the off-line template matching. Because there is no position or displacement sensor in this open-loop AFM scanner, the way to calculate absolute error is using each current local image as a template to match with accurate position in original image. This is the method to verify error but not the one we used in non-vector space control strategy which used MHD to define the error between current and desired images.

5.3.6 Performance Analysis of Non-vector Space Controllers

Currently, there are two different types of non-vector space controller-image feedback and compressive feedback. From the experimental result it shows that the steady state error of complete image feedback controller approaches to zero (error is approximate ± 1 nm) in both in x and y directions which proves that $dh(K(t), \hat{K}) \to 0$ as $t \to \infty$. However, in the case of compressive feedback, the error is not always converging to zero. This is because of following Proposition in compressive feedback controller.

Proposition 2 *Suppose both x and $\hat{x}$ obey the power law decay. Without loss of generality,*

assume we use the largest $S = \lceil n/2 \rceil$ *elements to approximate the original signals, where* $\lceil \cdot \rceil$ *is the ceil operator. If matrix A satisfies RIP condition with order* $2S$ *and constant* σ_{2S}*, then we have* $dh(K, \hat{K}) \leq 2R(\sqrt{1+\sigma_{2S}} + \sqrt{1-\sigma_{2S}})/\sqrt{S(1-\sigma_{2S})}$ *if* $dh(K_c, \hat{K}_c) \to 0$.

This proposition indicates that if $dh(K_c, \hat{K}_c) \to 0$, the set distance between the two compressive sets can be bounded. Therefore, instead of asymptotical stability, only the stability can be guaranteed (the detailed proof can be found in [141]). In other words there exists an steady state error in the compressive feedback controller. As shown in Fig. 5.5(b) the steady state error is approximate $\pm$2nm. Although steady stead error exists in compressive feedback controller, its advantage is still obvious which is less calculation time and high feedback rate which is useful for realtime control. It is noted that the accuracy of this non-vector space controller depends on the original image resolution and scan size which is used for visual servoing. If a 1024$\times$1024 pixels AFM image with the scan size of 600 nm is used, the accuracy of this non-vector space control system will reach as high as 1 nm according to this experiment result.

5.4 Carbon Nanotube Local Electrical Property Characterization

For nanomanipulations, one of the most essential parts is the high accuracy motion control. With the help of non-vector space controller, it enables the nanomanipulation system to have the ability to conduct delicate and complicated nano particles manipulation and nano surgery. In this research, an examples of the nanomanipulation: carbon nanotube local electrical property characterization based on non-vector space motion control are provided

to illustrate the application of this control strategy.

Carbon nanotube is a quasi-one-dimensional material which has been frequently used for building nanodevices. It is essenstial to understand the electronic properties of this kind of building blocks before design nanodevices. All several methods can be used for studying the properties of carbon nanotube, employing a conductive SPM probe as a movable electrode to conduct local conductivity measurements is a most efficient and direct approach [30][31][32][21]. Using SPM conductive probe to measure the conductivity can be considered as measuring transport properties as a function of channel length. Despite this measurement technique is suitable for studying electron transport property, only a few attempts ave been made in practices. The reason for that is the difficulty in accurate probe motion control during the measurement. There is no suitable way to accurate control conductive probe motion until the non-vector space control strategy has been proposed. In this section, we use AFM as a example to illustrate the application of using non-vector space to map multi-wall carbon nanotube local conductivity.

In this example, a MWNT located on two electrodes was used as the sample. The sample was fabricated using optical lithography. Here, a metal electrode consisting of Ti 30 nm/Au 50 nm layers was deposited on top of an In2O3 nanowire using an electron beam evaporator, followed by a lift-off process.

The MWNTs, are purchased from Bucky USA in powdery form. These MWNTs have diameters ranging from 20 to 200 nm, and lengthes from 0.5 to 10 μm. The SWCNTs powder was put into ethanol alcohol to form SWCNTs suspension after 10-20 minutes ultrasonication [142][143]. A single SWCNT was deposited to desired locations using dielectrophoresis (DEP) deposition system: a droplet of SWCNTs suspension in ethanol alcohol was dispersed between pre-fabricated electrodes, and an AC voltage of 1 Vpp and 10 kHz frequency was

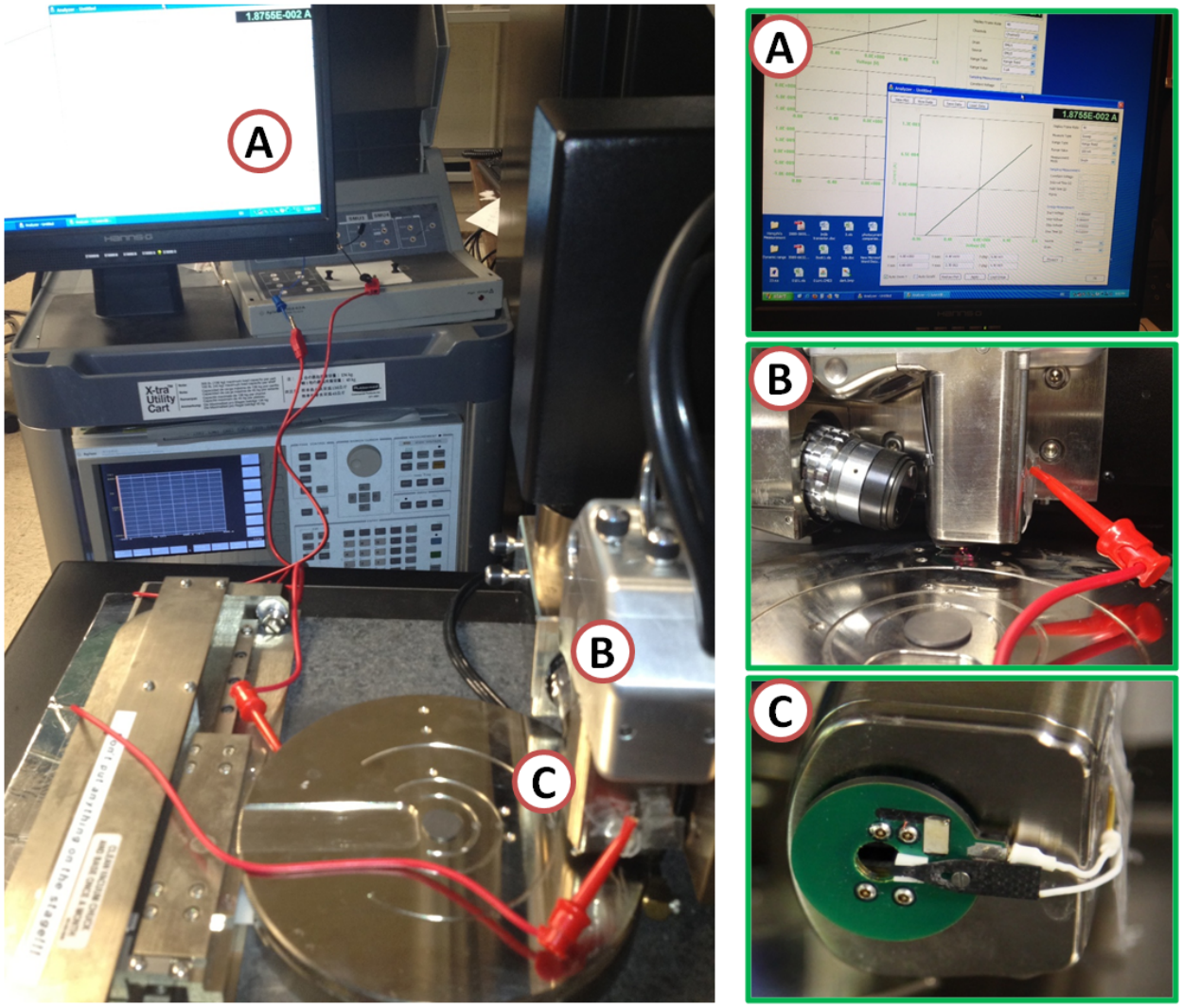

Figure 5.7 Testing platform (A): I-V curve obtain by curve tracer (B):Dimension 3100 AFM (C): Conductive probe

applied to attract the SWCNTs to the vicinity of the Au electrodes. The A symmetric Au-MWNT-Au sample was used in this example as a kind of nano wire whose diameter is small enough for testing the performance of non-vector space motion control.

Before conductivity mapping, a metallic I-V characteristic was observed (as shown in Fig. 5.9(a)). The total resistance of this MWNT is 11.0 $k\Omega$. In order to locally characterize the electrical properties, the samples are placed in an AFM (Dimension 3100, Bruker nano, CA) based nanomanipulation system operating at room temperature (as shown in Fig. 5.9. A

diamond-coated conductive probe (DDESP-FM-10, Bruker nano, CA) was used as a movable drain electrode when it was physically contacted with the MWNT (as shown in Fig. 5.7). The channel length L is the distance from the conductive tip to the source electrode. We begin by using the conductive tip as a source current contact. In this experiment we measured the current transfer through the channel with 20 nm interval evenly by placing the tip above the MWNT at specific location through non-vector space controller and then lowered until the physical contact was confirmed between tip and MWNT. Then the current flows from the conductive tip to the drain electrode is record by curve tracer. The resistance has plot as a function of channel length (as shown schematically in Fig. 5.9(b)).

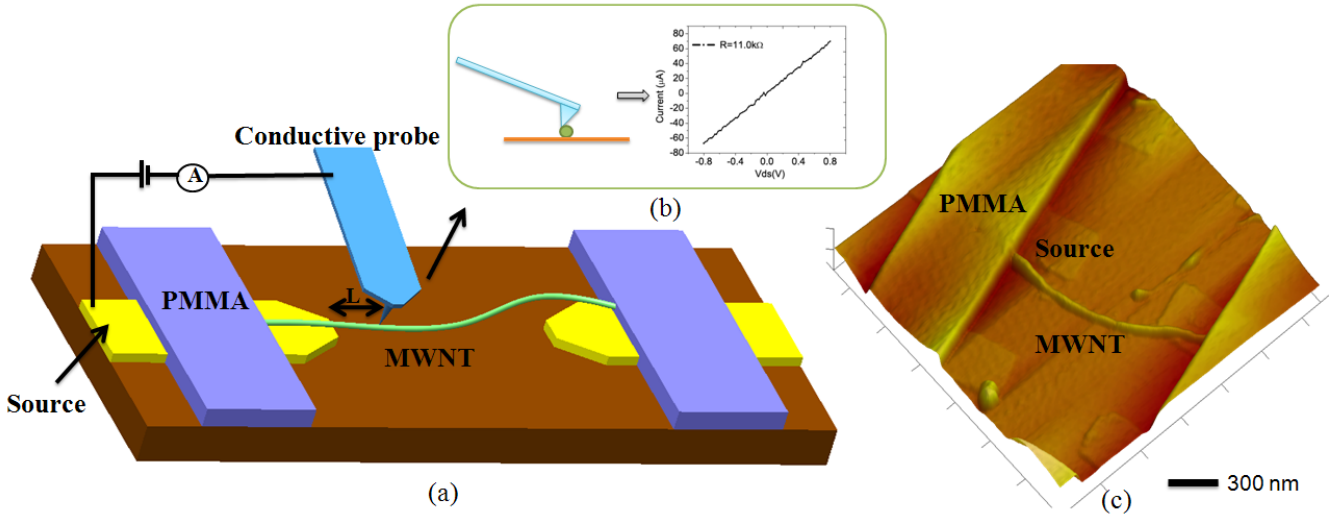

Figure 5.8 Schematic diagram of experimental setup for characterizing local conductivity (a): experimental setup (b): Using conductive tip to probe local conductance (c): AFM image of testing sample

5.5 Measurement Results and Analysis

In this application, we use non-vector space control method to probe accurate position of conductive tip as a movable electrode to investigate the scaling and electron transport

properties. These results are essential for uses of MWNT in transistor applications. Besides MWNT, other kinds of nanowire can be also used as samples. Non-vector space control method is a efficient way to accurate control SPM tip motion during nanomanipulations.

5.6 Controllable Electrical Breakdown of Multiwall Carbon Nanotubes

5.6.1 Introduction

With the development of nano-materials, such as nanotubes and nanowires, the electrical characterization of these materials, attracted strong attention because of their unique electrical and thermal properties due to quantum confinement [112][113]. As a typical nano material, multiwall nanotubes (MWNTs) have intrinsic thermal and electrical properties [114], which are being considered as potential candidates for the next generation of circuit wires and nano electronic devices such as nano transistors [115][116], and sensors [26][25][29]. The carbon nanotubes can hold a current density as high as 10^9 A/cm^2 (which is more than 1000 times greater than copper) [117], and the thermal conductivities is higher than 3000 Wm^{-1}K^{-1} [118]. However, the thermal and electrical properties of the MWNTs are not fully understood, especially for the electrical breakdown.

An MWNT consists of many layers of single-wall nanotubes, and each of them has a various mechanical, electrical and thermal properties. Electrical breakdown is possible to be well controlled to peel the outer layers of MWNT or tailor its structure, in order to change the properties of MWNT [119]. The electrical breakdown determines the maximum current transport through the MWNTs circuit, and it is also considered as an approach to

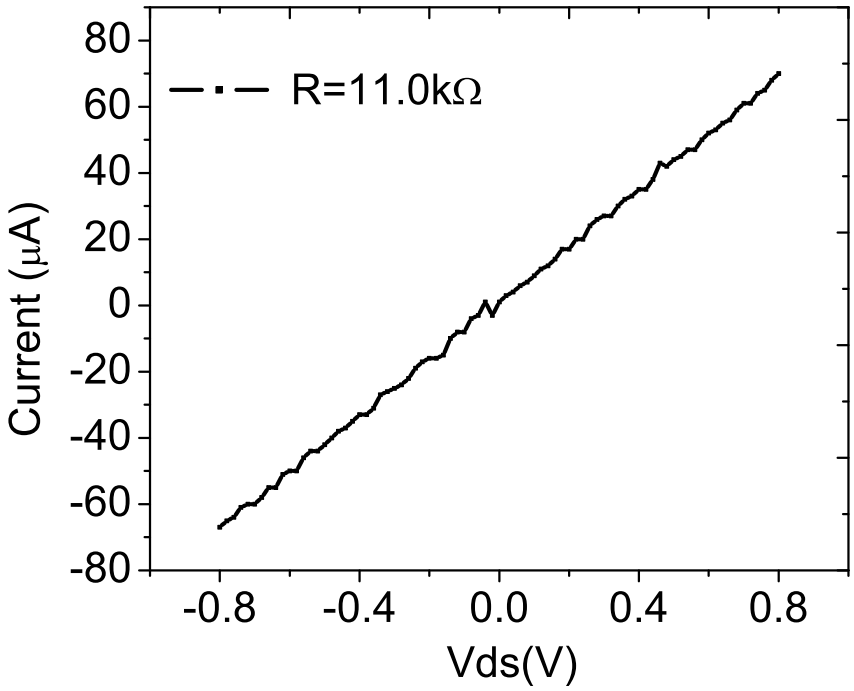

(a)

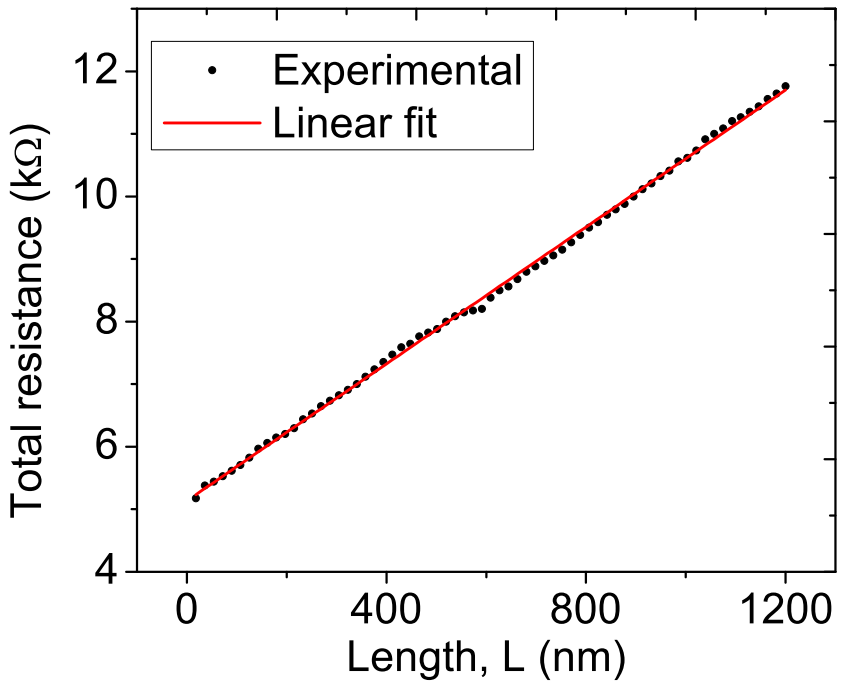

(b)

Figure 5.9 MWNT electric property characteristics (a): I-V characteristics from source to drain electrodes (b): Total resistance as a function of channel length

fabricate high performance sensors and transistors. It is essential to understand the electronic properties of the material prior to designing a high performance nanodevice. Generally, the electrical breakdown is caused by Joule heating produced by the electron flow in the layers of MWNT [120][121]. In practice, however, the reasons for electrical breakdown become various if environmental conditions are considered, such as energy dissipation to the electrodes, heat sink effect of substrate, local heating and oxidation. Although electrical breakdown is known as an issue for the applications of interconnects, it also can be considered as an approach to change local mechanical and/or electrical properties which could be more valuable than regular MWNTs for the applications of MWNTs based sensors and transistors.

It has been widely accepted that the electrical breakdown is caused by Joule heating [122]. In words, the electrical breakdown is expected to be happened in the center of a suspended MWNT. However, some studies observed converse results: electrical breakdowns are not always happened in the center, sometime it locates apart quit a long distance to the middle [123]. In such a condition, the structural defect of MWNT (which could reduce the local conductivity) was considered as the major reason that leads to the electrical breakdown [124]. Besides structural defect, local conductance change, such as diameter variation from one end to the other, also determines the position of electrical breakdown [125].

The motivation of present research is to find the crucial factors that affect electrical breakdown, and make the electrical breakdown controllable. Controllable electrical breakdown is studied utilizing atomic force microscopy (AFM) based nano robot. The AFM based nano robot is a special and useful technological device to image the nano structures, and to conduct local manipulations on nano materials [70][69][71]. The sharp AFM tip (apex is approximately 10 nm or less) can be considered as an end effector of the nano robot, which can measure and manipulate samples in nano scale. In this research an AFM based nano robot

is used to measure the local conductivity of MWNT, and manipulate its spatial structure to control the location of the heat sink, which makes electrical breakdown controllable.

5.6.2 Joule Heating and Thermal Dissipation of MWNT based Circuit

In this paper, first we study the determinants which control the position of electrical breakdown. After high bias voltage applied on both end of MWNT, it can be broken down by oxidation caused by Joule heating. To date, much attention has been paid on sustainable maximum current densities in nanotube, however, electrical breakdown is a much complicated phenomenon because of the nonuniform heat distribution. Joule heat is generated by the current and the dissipated by heat exchange from MWNT to the air, electrodes and substrate. The temperature (T) distribution of MWNT can be described as following one dimensional (along x axis) heat transport equation [144].

$$-\kappa\frac{d^2T}{dx^2} + \gamma T = q \tag{5.18}$$

where κ is the thermal conductivity of the MWNT, γ is the thermal coupling with substrate and environment respect to position, and q is the generated heat per unit volume [145]. Assumed that the power is homogeneously generated along the MWNT,

$$q = jF \tag{5.19}$$

where $j = I/A$ is current density through the effective cross section A, and F is the electrical field.

From Eq. (5.18) and (5.19), it can be found that, the local temperature is determined by MWNT thermal conductivity, thermal coupling with substrate and the generated heat. In order to illustrate that, we take the MWNT on electrodes as an example (as shown in Fig. 5.10). Considered a suspended MWNT with uniform resistance distribution (uniform diameter and no defect in structure), according to the heat transport equation, the highest temperature locates in the center of MWNT (as shown in Fig. 5.10(a)). However, in practice, for the MWNT based circuit and sensors, we have to take substrate effect and nonhomogeneous MWNT structure into account. Therefore, the temperature distribution is determined by the local conductivity of MWNT and local contact condition between MWNT and substrate.

In present research, we reveal that if MWNTs have a uniform and firm contact with substrate, local resistance distribution is the dominant factor for electrical breakdown. In such condition, if the MWNT has a uniform conductance distribution (as shown in Fig. 5.10(b)), the breakdown could be happened randomly at any location along the MWNT surface. Beyond the uniform conductance distribution, electrical breakdown happens at the position which has a sudden change of local resistance (as shown in Fig. 5.10(c)). This is because the heat generated in this area is bigger than the other parts of MWNT. However, if the MWNT does not have the uniform contact with the substrate, the resistance distribution of MWNT is no longer considered as the crucial of electrical breakdown compared with heat exchange effect. In this condition, the heat exchange is the determinate for the electrical breakdown. Since the substrate can be considered as a large heat sink, the Joule heat can be rapidly dissipated to the substrate at the contact area, while in other area the heat is slowly dissipated to the air. Therefore, electrical breakdown is most likely happened at the position without substrate contact. In order to verify our electrical breakdown theory, we used

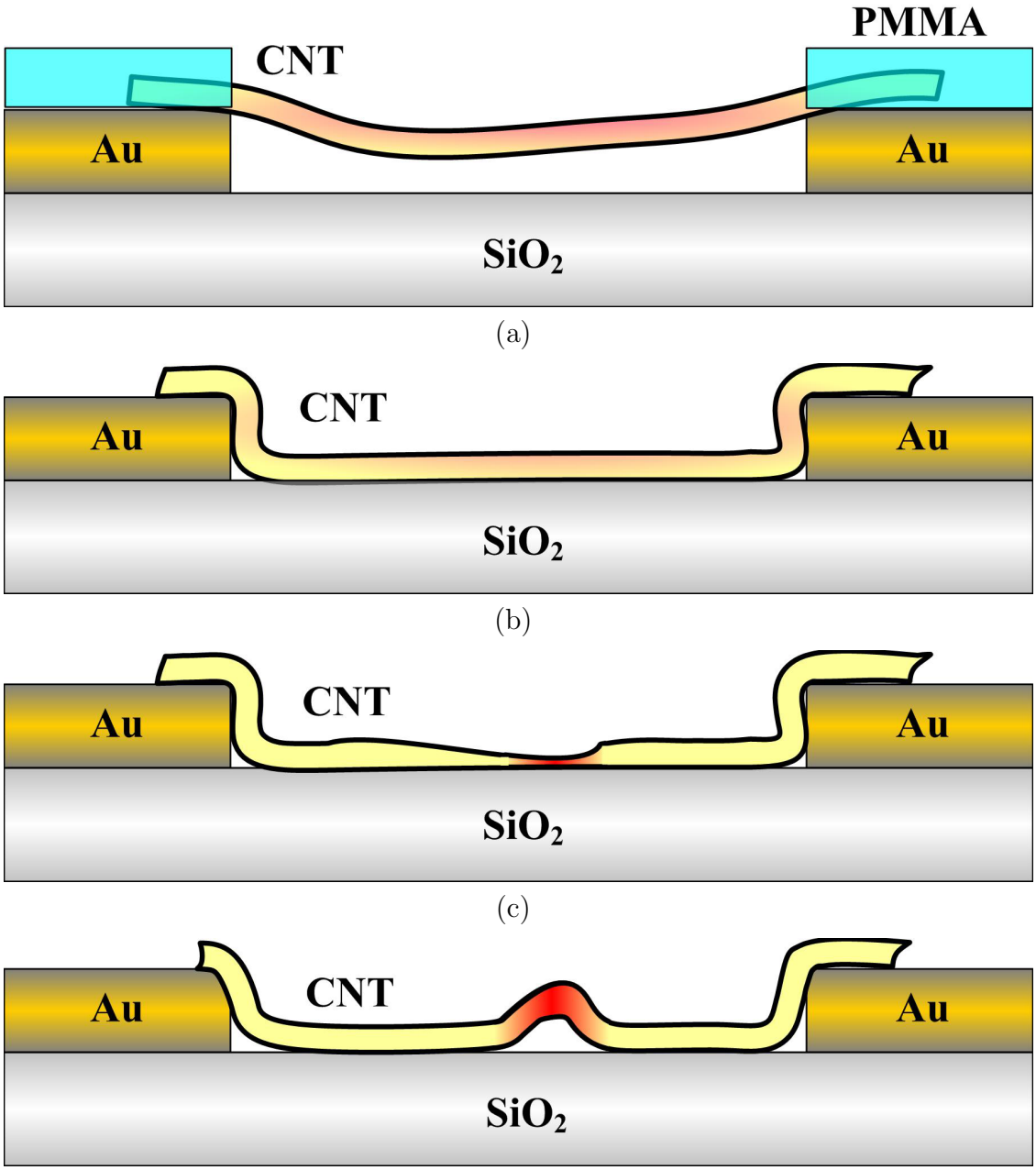

Figure 5.10 Diagram of thermal distribution of MWNT in different conditions, (a) A suspended MWNT, (b) An MWNT with firm and uniform contact with substrate, (c) An MWNT with defect contacted firmly and uniformly with substrate, (d) An MWNT with nonuniform contact with substrate

an AFM based nano robot to measure the local conductivity distribution and mechanically change the contact between MWNT and substrate.

5.6.3 Experimental Details

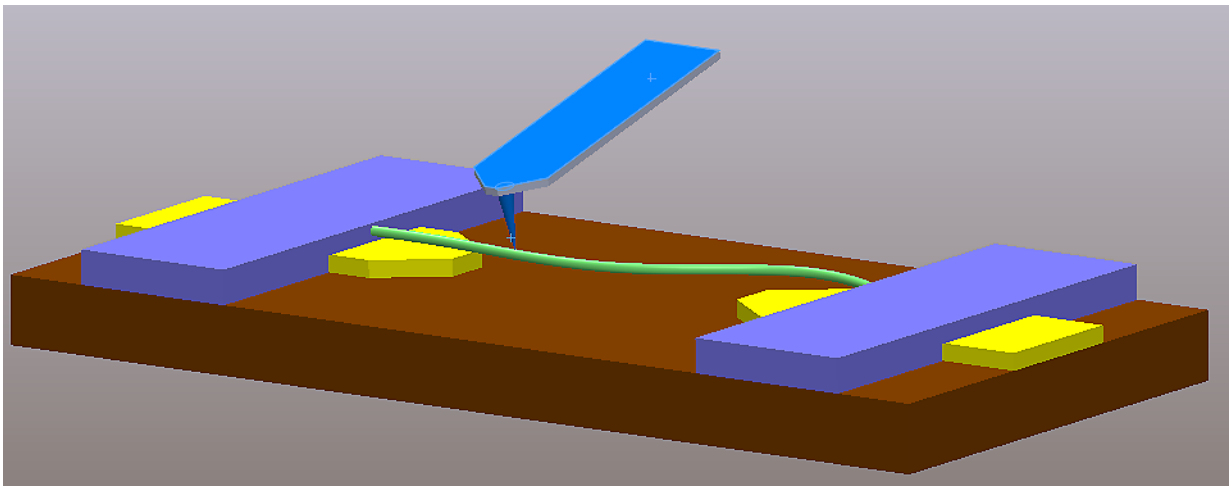

Figure 5.11 Experimental setup: MWNT on electrodes and moveable AFM probe for conductance characterization

In order to compare the influence of the determined breakdown factors, and find which the definitive one is, we design a serial of comparison experiments of local conductivity and thermal dissipation. The fabrication process of the testing device (as shown in Fig.5.11) started from fabricating two Au electrodes on the substrate through photolithography, thermal evaporation, and lift-off. After that, a single MWNT was deposited in the center to bridge two electrodes using dielectrophoresis (DEP) deposition system: MWNT powder, purchased from Bucky USA, was immersed into ethanol and ultrasonicated 10-20 minutes to form MWNT suspension; a droplet of the suspension was dispersed between the electrodes, and an AC voltage of 1 Vpp and 10 kHz frequency was applied to attract an MWNT to bridge the electrodes. A uniform PMMA layer was spin-coated on top of the device. The PMMA between two electrodes was removed after electron beam exposure and photoresist

development, and two strips of the PMMA at the contacts was left to pin an MWNT on the substrate.

Before conducting local conductance measurement, the global I-V characteristics of the devices were measured by applying biases between the electrodes, and the current was measured using a semiconductor parameter analyzer (4156c, Agilent Technologies, CA). A computer with a haptic device, a real-time Linux system and DAQ cards are used in this nanomanipulation system. In addition, a signal access and control box is developed to acquire the signal of topography information and input the control signal into the AFM controller. In order to locally characterize their electrical properties, samples were placed in an AFM (Dimension 3100, Bruker nano, CA) based compressive feedback based non-vector space nanomanipulation system integrating with an electrical measurement system. A diamond-coated conductive probe (DDESP-FM-10, Bruker nano, CA) was used as a movable drain electrode (as shown in Fig.5.11). The channel length L is the distance from the conductive tip to the source electrode.

5.6.4 Results and Discussion

The resistance distribution of MWNT, which is a key parameter of electrical breakdown, was accurately measured by an AFM based nano robot and a non-vector space control strategy were used, and the position error in the measurement was controlled within several nanometers. In the experiment, the length dependent local conductance of the MWNT was measured with a length increment of 20 nm. The conductive tip of the nano robot was firstly positioned above the MWNT at a specific location, and followed by lowering the tip to contact with the MWNT. The current flows from the conductive tip to the electrode were recorded, and the total resistance was plotted as a function of channel length.

In the first experiment, we used an MWNT with uniform conductance distribution (which was pre-selected according to the resistance distribution) as shown in Fig. 5.12(a). From the resistance map (Fig. 5.12(b)), it can be found that, the resistance increases gradually and continuously with the incensement of the length of MWNT, and that means the conductance of this MWNT has a uniform distribution. After that, we used the nano robot to make MWNT and substrate have a firm contact (Fig. 5.12(a)). The contact was double checked by using AFM topography image. The MWNTs we used in this experiment has been carefully examined by scanning electron microscopy (SEM), to make sure each one has the uniform diameter distribution.

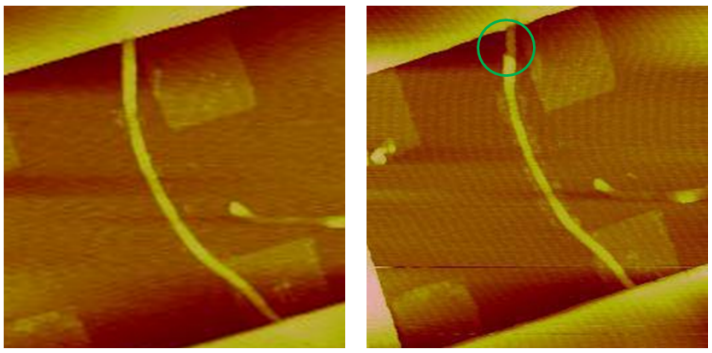

(a)

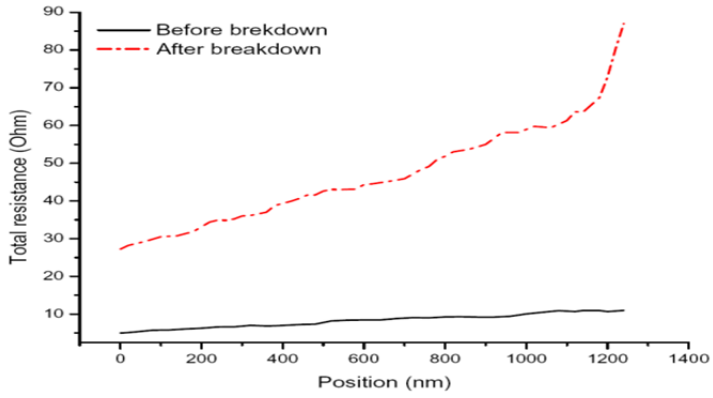

(b)

Figure 5.12 Electrical breakdown of an MWNT with uniform conductance distribution, (a) The AFM images before (left) and after (right) the electrical breakdown, (b) The total resistance respect to the channel length before and after the electrical breakdown, measuring direction: from the bottom end to the upper end of the MWNT in (a)

In such a condition, after bridged on two electrodes, topography changes reflect the three dimensional structure of MWNT. The location with higher position in vertical direction (respect to the plane of substrate) means that, at this point, MWNT is apart from the substrate. For the MWNT in the first experiment, because the topography has no significant change, the firm contact between MWNT and substrate was established. In this condition, the breakdown could happen at any location randomly, and as a result, the breakdown happened at the location of the upper position of the MWNT (circled with green color in Fig. 5.12(a) (right)).

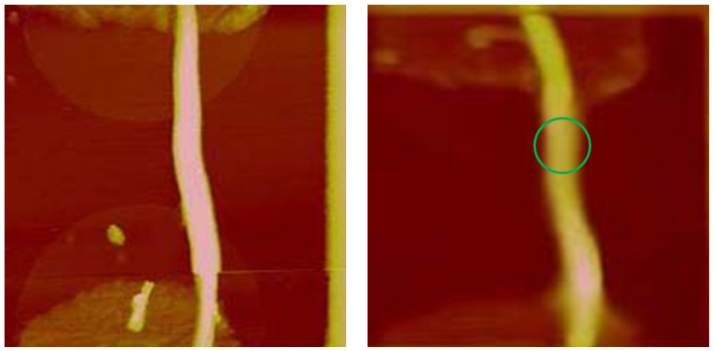

(a)

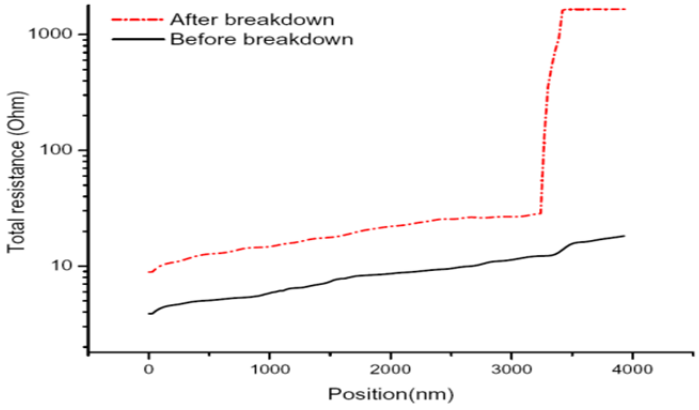

(b)

Figure 5.13 Electrical breakdown of an MWNT with nonuniform conductance distribution, (a) The AFM images before (left) and after (right) the electrical breakdown, (b) The total resistance respect to the channel length before and after the electrical breakdown, measuring direction: from the bottom end to the upper end of the MWNT in (a)

In the next experiment, we chose an MWNT with defect, which means the local conductance could have a sudden jump at a specific position. We found this sudden jump position after carefully measuring the resistance distribution using our AFM system (the resistance distribution is shown in Fig. 5.13(b)). According to Eq. (5.18) and (5.19), in this case, the generated heat has a nonuniform distribution: the maximum temperature locates at the position with a sudden jump of conductance, where the biggest local resistance was found. We predicted that, the breakdown would happen at the position where the biggest local resistance was found. This is supported by the experimental results (the location of breakdown is labeled by green circle in the right image of Fig. 5.13(a), which is the position with a sudden jump of resistance).

From the analysis above, we may concluded that, from the view of heat generation, local resistance distribution is the key parameter for the electrical breakdown, if the thermal dissipation is not taken into account. However, in practice of MWNT based circuit wire or transistor system, the thermal dissipation is a more essential parameter compared with the local conductance distribution.

In order to find the evidence which can support the theory above, in the last experiment, we chose an MWNT with nonuniform conductance distribution (as shown in Fig. 5.14(b)). After measuring the resistance distribution of this MWNT, we used the AFM probe to push one end of this MWNT (the other end is fixed by a thin layer of PMMA) to make some parts of this MWNT apart from the substrate. After that, we covered the pushing end of this MWNT with PMMA to maintain its three dimension structure, and a topography image was obtained using AFM (as shown in Fig. 5.14(a) left).

From the topography map, we predicted that electrical breakdown is very likely to be happened at the highest position (the place has the maximum vertical distance from the

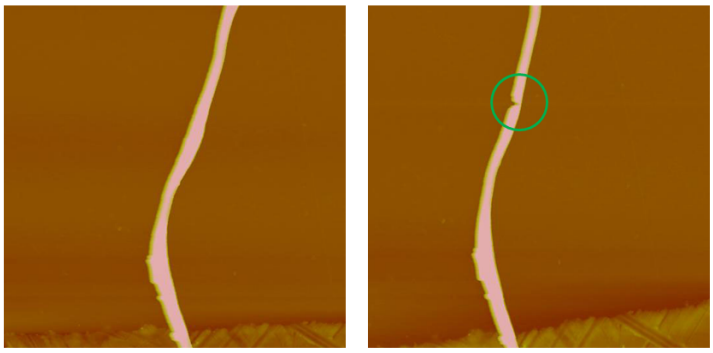

(a)

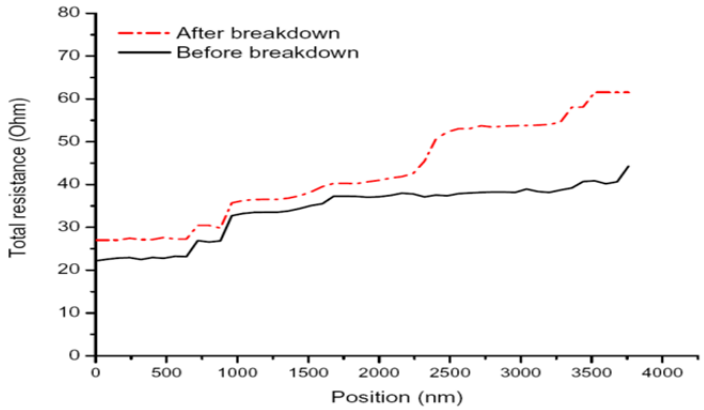

(b)

Figure 5.14 Electrical breakdown of an MWNT with nonuniform conductance distribution and contact consition, (a) The AFM images before (left) and after (right) the electrical breakdown, (b) The total resistance respect to the channel length before and after the electrical breakdown, measuring direction: from the bottom end to the upper end of the MWNT in (a)

substrate). The prediction is made according to Eq. (5.18) and (5.19), the temperature is determined by both the conductivity distribution and the nonuniform thermal dissipation. From the experimental results, the breakdown is most likely to be happened at the position which has a furthest distance apart from the substrate (labeled by green circle in Fig. 5.14(a) right) with the minimum thermal dissipation. From the resistance measuring and breakdown results we can find that: although the maximum conductance change located in the lower part of this MWNT, the electrical breakdown happened in the upper part of the MWNT, where the MWNT has the minimum thermal dissipation.

We may conclude that, the thermal dissipation is the dominate parameter for MWNT based circuit wire. Although in Eq. (5.18) and (5.19), conductance change is also a parameter regrading to thermal generating, since the conductance distribution in MWNT is unlikely to have such a significant change that generating enough thermal energy for breakdown. Therefore, compared with conductance distribution, thermal dissipation (the contact condition between MWNT and substrate) is the most important parameter for electrical breakdown. In general, from the view of nanocircuit, firm contact between MWNT and substrate can assure a rapid thermal dissipation from MWNT to the substrate, which works as a heat sink. In such a condition, the MWNT can hold larger electron density and reduce the probability that electrical breakdown happened. From the perspective of MWNT engineering, the electrical breakdown is controllable by means of controlling the contact condition between MWNT and its substrate. This is an alternative way to tailor the MWNT and change its local mechanical and electrical properties to fabricate high performance transistors and sensors.

5.7 Conclusions

From a fundamental perspective, the non-vector space control method has the ability to make high accurate SPM based nanomanipulations easier, and simultaneously the compressive feedback can make a real-time nanomanipulation possible. The integrating of these two approaches can achieve a high accuracy and high speed motion control for SPM based nanomanipulation. Furthermore, the theory developed in this research can be applied to nano assembly, nano imaging, nanomanipulation and so forth which are the area we will consider in the future. As an application research, we studied the parameters which control the location where the electrical breakdown of MWNT happened. The contact condition was firstly took into consideration as a dominate parameter towards electrical breakdown. We conclude that compared with thermal accumulation (for suspended MWNT), resistance distribution (the structural defect), the thermal dissipation: the contact condition between MWNT and substrate, contributes more in thermal dynamics in the process of electrical breakdown. The experimental results well support this conclusion. The electrical breakdown could be mechanically controlled by an additional heat sink, which could be the substrate of MWNT device. Therefore, the electrical breakdown process is controllable through controlling Joule heating and thermal dissipation. Manipulating the three dimensional structure of MWNT to change the position of heat sink is an alternative way to control the location that electrical breakdown happened. Moreover, the conclusion of this research also provides a suggestion for the fabrication of nanocircuit, firm contact between MWNT and substrate assures that the MWNT can hold larger electron density and reduce the probability that electrical breakdown happened.

Chapter 6

Conclusions and Future Work

6.1 Conclusions

In this study, we proposed a systematic multimodal sensing approach in the nano/bio environment. We first used compressive sensing technique to increase the imaging rate of SPM/AFM to make it suitable to dynamically observe the sample surface in real-time. A followed up application study shows that, this fast imaging technique can lead better understanding of enzymatic hydrolysis process. Our experimental result and analysis suggest that the surface density of active *TrCel7A*, is the dominate factor that caused the inactivation of enzyme during the hydrolysis process, which may be an useful information for protein engineering study to increase the efficiency of enzymatic hydrolysis rate.

We also proposed a brand new mechanical properties measurement method called "vibration mode". Different with conventional point and shooting signal measurement, vibration measurement is a more efficiency method to evaluate the mechanical properties of internal structure of elastic material. The basic idea of this method is to vibrate vertically and the additional vibration amplitude on the upper surface of sample, other than the driving vibration can be considered as the sample deformation which depends on the mechanical properties. Our experimental results show that, vibration mode can provide faster imaging speed, and multi-channel information from noninvasive biological properties measurements than conventional AFM based imaging and measurements.

Other than improving the performance of SPM imaging and measurement, we also proposed a new control method called "non-vector space control" to increase the positioning accuracy of SPM based manipulation and measurement. It has the ability to realize high accurate SPM based nanomanipulations and simultaneously the compressive feedback can make a real-time nanomanipulation possible. Furthermore, the theory developed in this research can be applied to nano assembly, nano imaging, nanomanipulation and so forth. In a followup application research, we studied the parameters which control the location where the electrical breakdown of MWNT happened. The contact condition was firstly took into consideration as a dominate parameter towards electrical breakdown. We conclude that compared with thermal accumulation (for suspended MWNT), resistance distribution (the structural defect), the thermal dissipation: the contact condition between MWNT and substrate, contributes more in thermal dynamics in the process of electrical breakdown.

6.2 Future Work

6.2.1 Quantitatively Analyze *TrCel7A* Molecules Involved Enzymatic Hydrolysis Process

The density of *TrCel7A* on substrate is an important since it indicates the effective adsorption of cellobiohydrolases and is mediated by the CBD. The adsorption of the family 1 CBD on crystalline cellulose requires three aromatic amino acids, and the binding sites to cellulose crystals. Due to the processive characteristics of hydrolysis, the binding of *TrCel7A* and cellulose affects the hydrolysis rate. Generally, efficient enzymatic hydrolysis requires high binding density, high moving velocity and low dissociation rate. In the future, we plan to

use raman microscopy and HPLC to quantitatively analyze the parameters of enzymatic hydrolysis process, such as the concentration of substrate, enzyme and the product, and associated with our previous single molecule experimental result to build a kinematic model to better the understanding the slow rate of hydrolysis.

6.2.2 Subsurface Structure or Mechanical Properties Measurement Using Vibration Mode for Cell Migration Study

Vibration mode measurement is naturally suitable to evaluate the mechanical properties of internal structure of elastic material. Previous section illustrates the idea of substructure mechanical properties measurement working principle. In the future we will use our vibration mode to study the mechanical properties changes during the cell migration.

Cell monolayer migration is an important physiological phenomenon involved in embryo development, wound healing, and cancer invasion, but its governing principle is a still mystery. The monolayer migration dynamics is related with substrate viscosity, stiffness, topography, cellular traction force, free space and cell damage and the geometry of cell monolayer. At individual cell level, cellular stiffness strongly impacts cellular invasion and integrity in keratinocytes. Thus, there is a critical need to establish the role of cellular stiffness in collective cell monolayer migration. Without this knowledge, the governing principle of collective cell migration may be misunderstood, thus hinder developing new therapies for wound healing and cancer metastasis. In such a condition, our vibration mode mechanical properties measurement system will be a perfect candidate to study the mechanical properties changes during the cell migration, and use the experimental data to build a physical model of cell migration which will bridge the gap of the understanding of basic migration

mechanism and could direct the development of drug for faster wood healing.

REFERENCES

REFERENCES

[1] R. Yang, N. Xi, K. C. M. Fung, K. W. C. Lai, Seiffert-Sinha, and A. A. Sinha, "Analysis of keratinocytes stiffness after desmosome disruption using atomic force microscopy based nanomanipulation," in *Proc. IEEE Int. Conf. Nanotechnology*, Genoa, Italy, 2009, pp. 640–643.

[2] B. Song, N. Xi, R. Yang, K. W. C. Lai, and C. Qu, "On-line sensing and visual feedback for atomic force microscopy (afm) based nano-manipulations," in *Proc. IEEE Int. Conf. Nanotechnology Materials and Devices (NMDC)*, Monterey, California, USA, 2010, pp. 71–74.

[3] G. Li, N. Xi, and D. H. Wang, "In situ sensing and manipulation of molecules in biological samples using a nano robotic system," *Nanomedicine*, vol. 1, no. 1, pp. 31–40, 2005.

[4] G. Li, N. Xi, M. Yu, and W.-K. Fung, "Development of augmented reality system for afm-based nanomanipulation," *Mechatronics, IEEE/ASME Transactions on Mechatronics*, vol. 4, no. 9, pp. 358–365, 2004.

[5] M. Lastella, M. Lasalvia, G. Perna, P. Biagi, and V. Capozzi, "Atomic force microscopy study on human keratinocytes treated with hgcl2," *Journal of Phisics conference series*, vol. 61, 2007.

[6] R. Yang, N. Xi, C. Fung, C. Qu, and J. Xi, "Comparative studies of atomic force microscopy (afm) and quartz crystal microbalance with dissipation (qcm-d) for real-time identification of signaling pathway," *IEEE Conference on Nanotechnology*, 2010.

[7] N. A. Burnham, R. J. Colton, and H. M. Pollock, "Interpretation issues in force microscopy," *Journal of Vacuum Science & Technology A*, vol. 9, no. 4, pp. 2548–2556, 1991.

[8] A. Rosa-Zeiser, E. Weilandt, S. Hild, and O. Marti, "The simultaneous measurement of elastic, electrostatic and adhesive properties by scanning force microscopy: pulsed-force mode operation," *Measurement Science and Technology*, vol. 8, no. 11, p. 1333, 1997.

[9] Z. Parlak and F. Degertekin, "Combined quantitative ultrasonic and time-resolved interaction force afm imaging," *Review of Scientific Instruments*, vol. 82, no. 1, p. 013703, 2011.

[10] H. Chen, N. Xi, K. Lai, C. Fung, and R. Yang, "Development of infrared detectors using single carbon-nanotube-based field-effect transistors," *Nanotechnology, IEEE Transactions on*, vol. 9, no. 5, pp. 582 –589, 2010.

[11] H. Chen, N. Xi, K. Lai, C. Fung, L. Chen, and J. Lou, "Analysis and design of carbon nanotube based field effect transistors for nano infrared sensors," in *Proc. IEEE Int. Conf. Nanotechnology Materials and Devices (NMDC)*, Monterey, California, USA, 2010, pp. 164–168.

[12] H. Chen, N. Xi, K. Lai, C. Fung, and R. Yang, "Analysis and design of carbon nanotube based field effect transistors for nano infrared sensors," in *Proc. IEEE Int. Conf. Nanotechnology Materials and Devices (NMDC)*, Traverse City, Michigan, USA, 2009, pp. 91–95.

[13] B. Song, N. Xi, R. Yang, K. W. C. Lai, and C. Qu, "Video rate atomic force microscopy imaging," in *Proc. ANS EPRRSD - 13th Robotics and remote Systems for Hazardous Environments and 11th Emergency Preparedness and Response*, Knoxville, TN, USA, 2011, p. To Appear.

[14] H.-J. Butt, P. Siedle, K. Seifert, K. Fendler, T. Seeger, E. Bamberg, A. Weisenhorn, K. Goldie, and A. Engel, "Scan speed limit in atomic force microscopy," *Journal of microscopy*, vol. 169, no. 1, pp. 75–84, 1993.

[15] D. Walters, J. Cleveland, N. Thomson, P. Hansma, M. Wendman, G. Gurley, and V. Elings, "Short cantilevers for atomic force microscopy," *Review of Scientific Instruments*, vol. 67, no. 10, pp. 3583–3590, 1996.

[16] M. B. Viani, L. I. Pietrasanta, J. B. Thompson, A. Chand, I. C. Gebeshuber, J. H. Kindt, M. Richter, H. G. Hansma, and P. K. Hansma, "Probing protein–protein interactions in real time," *Nature Structural & Molecular Biology*, vol. 7, no. 8, pp. 644–647, 2000.

[17] T. Ando, N. Kodera, D. Maruyama, E. Takai, K. Saito, and A. Toda, "A high-speed atomic force microscope for studying biological macromolecules in action," *Japanese Journal of Applied Physics*, vol. 41, no. 7S, p. 4851, 2002.

[18] T. Ando, N. Kodera, E. Takai, D. Maruyama, K. Saito, and A. Toda, "A high-speed atomic force microscope for studying biological macromolecules," *Proceedings of the National Academy of Sciences*, vol. 98, no. 22, pp. 12 468–12 472, 2001.

[19] J. H. Kindt, G. E. Fantner, J. A. Cutroni, and P. K. Hansma, "Rigid design of fast scanning probe microscopes using finite element analysis," *Ultramicroscopy*, vol. 100, no. 3, pp. 259–265, 2004.

[20] T. Ando, T. Uchihashi, N. Kodera, A. Miyagi, R. Nakakita, H. Yamashita, and M. Sakashita, "High-speed atomic force microscopy for studying the dynamic behavior of protein molecules at work," *Japanese journal of applied physics*, vol. 45, no. 3S, p. 1897, 2006.

[21] Z. Fan and J. G. Lu, "Electrical properties of zno nanowire field effect transistors characterized with scanning probes," *Applied Physics Letters*, vol. 86, no. 3, p. 032111, 2005.

[22] S. Desbief, N. Hergue, O. Douheret, M. Surin, P. Dubois, Y. Geerts, R. Lazzaroni, and P. Leclere, "Nanoscale investigation of the electrical properties in semiconductor polymer-carbon nanotube hybrid materials," *Nanoscale*, vol. 4, pp. 2705–2712, 2012.

[23] X. Michalet, F. Pinaud, L. Bentolila, J. Tsay, S. Doose, J. Li, G. Sundaresan, A. Wu, S. Gambhir, and S. Weiss, "Quantum dots for live cells, in vivo imaging, and diagnostics," *Science*, vol. 307, no. 5709, pp. 538–544, 2005.

[24] S. J. Tans, A. R. M. Verschueren, and C. Dekker, "Room-temperature transistor based on a single carbon nanotube," *Nature*, vol. 393, no. 6680, pp. 49–52, 1998.

[25] H. Z. Chen, N. Xi, K. W. C. Lai, L. L. Chen, R. G. Yang, and B. Song, "Gate dependent photo-responses of carbon nanotube field effect phototransistors," *Nanotechnology*, vol. 23, no. 38, p. 385203.

[26] H. Chen, N. Xi, B. Song, L. Chen, J. Zhao, K. W. C. Lai, and R. Yang, "Infrared camera using a single nano-photodetector," *Sensors Journal, IEEE*, vol. 13, no. 3, pp. 949–958, March.

[27] Y.-J. Choi, I.-S. Hwang, J.-G. Park, K. J. Choi, J.-H. Park, and J.-H. Lee, "Novel fabrication of an sno 2 nanowire gas sensor with high sensitivity," *Nanotechnology*, vol. 19, no. 9, p. 095508, 2008.

[28] H. Chen, N. Xi, K. Lai, L. Chen, C. Fung, and J. Lou, "Plasmonic-resonant bowtie antenna for carbon nanotube photodetectors," *International Journal of Optics*, vol. 2012, p. 1, 2012.

[29] H. Chen, N. Xi, K. Lai, C. Fung, and R. Yang, "Development of infrared detectors using single carbon-nanotube-based field-effect transistors," *Nanotechnology, IEEE Transactions on*, vol. 9, no. 5, pp. 582 –589, 2010.

[30] T. K. Ghanem, E. D. Williams, and M. S. Fuhrer, "Characterization of the electrical contact between a conductive atomic force microscope cantilever and a carbon nanotube," *Journal of Applied Physics*, vol. 110, no. 5, p. 054305, 2011.

[31] G. Jo, J. Maeng, T.-W. Kim, W.-K. Hong, B.-S. Choi, and T. Lee, "Channel-length and gate-bias dependence of contact resistance and mobility for in2o3 nanowire field effect transistors," *Journal of Applied Physics*, vol. 102, no. 8, p. 084508, 2007.

[32] X. Zhou, S. A. Dayeh, D. Aplin, D. Wang, and E. T. Yu, "Direct observation of ballistic and drift carrier transport regimes in inas nanowires," *Applied Physics Letters*, vol. 89, no. 5, p. 053113, 2006.

[33] S. M. Salapaka and M. V. Salapaka, "Scanning probe microscopy," *IEEE Control System Magazine*, vol. 28, no. 2, pp. 65–83, 2008.

[34] B. Mokaberi and A. A. G. Requicha, "Compensation of scanner creep and hysteresis for AFM nanomanipulation," *IEEE Trans. on Automation Science and Engineering*, vol. 5, no. 2, pp. 197–206, 2008.

[35] D. Croft, G. Shed, and S. Devasia, "Creep, hysteresis, and vibration compensation for piezoactuators: Atomic force microscopy application," *ASME Journal of Dynamic Systems, Measurement, and Control*, vol. 123, no. 1, pp. 35–43, 2001.

[36] S. Devasia and E. E. S. O. R. Moheimani, "A survey of control issues in nanopositioning," *IEEE Transactions on Control System Technology*, vol. 15, no. 5, pp. 802–823, 2007.

[37] H. Chen, N. Xi, K. Lai, C. Fung, and R. Yang, "Cnt infrared detectors using schottky barriers and p-n junctions based fets," in *IEEE Nanotechnology Materials and Devices Conference*, Traverse City, Michigan, USA, 2009, pp. 91–95.

[38] H. Chen, N. Xi, K. W. C. Lai, L. Chen, C. K. M. Fung, and J. Lou, "Plasmonic-resonant bowtie antenna for carbon nanotube photodetectors," *International Journal of Optics*, vol. 2012, pp. 582–589, 2012.

[39] H. Chen, N. Xi, K. W. C. Lai, L. Chen, R. Yang, and B. Song, "Gate dependent photoresponses of carbon nanotube field effect phototransistors," *Nanotechnology*, vol. 23, no. 38, p. 385203 (8 pages), 2012.

[40] R. V. Lapshin., "Analytical model for the approximation of hysteresis loop and its application to the scanning tunneling microscope," *Review of Scientific Instruments*, vol. 66, no. 9, pp. 4718–4730, 1995.

[41] K. Kuhnen and H. Janocha, "Inverse feedforward controller for complex hysteretic nonlinearities in smart-material systems," *Control Intelligence system*, vol. 29, no. 3, pp. 74–83, 2001.

[42] P. Krejci and K. Kuhnen, "Inverse control of systems with hysteresis and creep," *IEE Proceedings - Control Theory and Applications*, vol. 148, no. 3, pp. 185–192, 2001.

[43] P.-L. Yen, M.-T. Yan, and Y. Chen, "Hysteresis compensation and adaptive controller design for a piezoceramic actuator system in atomic force microscopy," *Asian Journal of Control*, vol. 14, no. 4, pp. 1012–1027, 2012.

[44] H. Habibullah, H. Pota, I. Petersen, and M. Rana, "Creep, hysteresis, and cross-coupling reduction in the high-precision positioning of the piezoelectric scanner stage of an atomic force microscope," *Nanotechnology, IEEE Transactions on*, vol. PP, no. 99, pp. 1–1, 2013.

[45] A. J. Fleming and K. K. Leang, "Integrated strain and force feedback for high-performance control of piezoelectric actuators," *Sensors and Actuators A-Physical*, vol. 161, no. 1-2, pp. 256–265, 2010.

[46] Y. Zhu, S. O. R. Moheimani, and M. R. Yuce, "Simultaneous capacitive and electrothermal position sensing in a micromachined nanopositioner," *IEEE Electron Device Letters*, vol. 32, no. 8, pp. 1146–1148, 2011.

[47] S. Gonda, T. Doi, T. Kurosawa, Y. Tanimura, N. Hisata, T. Yamagishi, H. Fujimoto, and H. Yukawa, "Real-time, interferometrically measuring atomic force microscope for direct calibration of standards," *Review of scientific instruments*, vol. 70, no. 8, pp. 3362–3368, 1999.

[48] M. Rakotondrabe, "Bouc–wen modeling and inverse multiplicative structure to compensate hysteresis nonlinearity in piezoelectric actuators," *Automation Science and Engineering, IEEE Transactions on*, vol. 8, no. 2, pp. 428–431, 2011.

[49] L. Liu, Y. Luo, N. Xi, Y. Wang, J. Zhang, and G. Li, "Sensor referenced real-time videolization of atomic force microscopy for nanomanipulations," *IEEE/ASME Trans. Mechatronics*, vol. 13, no. 1, pp. 76–85, 2008.

[50] F. Chaumette and S. Hutchinson, "Visual servo control part I: Basic approaches," *IEEE Robot. Autom. Mag.*, vol. 13, no. 4, pp. 82–90, 2006.

[51] E. Marchand and F. Chaumette, "Feature tracking for visual servoing purposes," *Robot. Auton. Syst.*, vol. 52, no. 1, pp. 53–70, 2005.

[52] V. Kallem, M. Dewan, J. P. Swensen, G. D. Hager, and N. J. Cowan, "Kernel-based visual servoing," in *Proc. IEEE/RSJ Int. Conf. Intell. Robots Syst.*, San Diego, CA, USA, 2007, pp. 1975–1980.

[53] C. Collewet and E. Marchand, "Photometric visual servoing," *IEEE Transactions on Robotics*, vol. 27, no. 4, pp. 828–834, 2011.

[54] S. Han, A. Censi, A. D. Straw, and R. M. Murray, "A bio-plausible design for visual pose stabilization," in *Proc. IEEE/RSJ Int. Conf. Intell. Robots Syst.*, Taipei, Taiwan, 2010, pp. 5679–5686.

[55] A. Dame and E. Marchand, "Mutual information-based visual servoing," *IEEE Transactions on Robotics*, vol. 27, no. 5, pp. 1–12, 2011.

[56] G. Li, N. Xi, H. Chen, C. Pomeroy, and M. Prokos, ""videolized" atomic force microscopy for interactive nanomanipulation and nanoassembly," *Nanotechnology, IEEE Transactions on*, vol. 4, no. 5, pp. 605–615, 2005.

[57] F. Dinelli, H. Assender, N. Takeda, G. Briggs, and O. Kolosov, "Elastic mapping of heterogeneous nanostructures with ultrasonic force microscopy (ufm)," *Surface and interface analysis*, vol. 27, no. 5-6, pp. 562–567, 1999.

[58] O. V. Kolosov, M. R. Castell, C. D. Marsh, G. A. D. Briggs, T. Kamins, and R. S. Williams, "Imaging the elastic nanostructure of ge islands by ultrasonic force microscopy," *Physical review letters*, vol. 81, no. 5, p. 1046, 1998.

[59] F. Dinelli, C. Albonetti, and O. V. Kolosov, "Ultrasonic force microscopy: Detection and imaging of ultra-thin molecular domains," *Ultramicroscopy*, vol. 111, no. 4, pp. 267–272, 2011.

[60] G. Sauerbrey, "Verwendung von schwingquarzen zur wägung dünner schichten und zur mikrowägung," *Zeitschrift für Physik*, vol. 155, no. 2, pp. 206–222, 1959.

[61] G. Binning, C. F. Quate, and C. Gerber, "Atomic force microscope," *Physical Review Letters*, vol. 56, no. 9, pp. 930–933, 1986.

[62] R. Yang, N. Xi, K. W. Lai, B. Zhong, C. K. Fung, C. Qu, and D. H. Wang, "Nanomechanical analysis of insulinoma cells by atomic force microscopy after glucose and capsaicin stimulation," *Acta Pharmacologica Sinica.*, vol. 32, no. 6, pp. 853–860, 2011.

[63] C. K. Fung, K. Seiffert-Sinha, K. W. Lai, R. Yang, D. Panyard, J. Zhang, N. Xi, and A. A. Sinha, "Investigation of human keratinocyte cell adhesion using atomic force microscopy (afm),," *INanomedicine: Nanotechnology, Biology, and Medicine.*, vol. 6, no. 1, pp. 191–200, 2009.

[64] E. Candes, J. Romberg, and T. Tao, "Robust uncertainty principles: exact signal reconstruction from highly incomplete frequency information," *IEEE Transactions on Information Theory*, vol. 52, no. 2, pp. 489–509, 2006.

[65] D. L. Donoho and Y. Tsaig, "Extensions of compressed sensing," *Signal Processing*, vol. 86, no. 3, pp. 533–548, 2006.

[66] D. L. Donoho, "For most large underdetermined systems of linear equations, the minimal l1 norm solution is also the sparsest solution," *Communications on Pure and Applied Mathematics*, vol. 59, no. 6, pp. 797–829, 2006.

[67] S. V. Ann, S. V. Ann, C. J. Yong, and C. J. Kiat, "Evolutionary algorithms for solving multi-objective travelling salesman problem," *Flexibile Services and Manufacturing Journal*, vol. 23, no. 2, pp. 207–241, 2011.

[68] O. Kolosov and K. Yamanaka, "Nonlinear detection of ultrasonic vibrations in an atomic force microscope," *Japanese journal of applied physics*, vol. 32, no. 8A, p. L1095, 1993.

[69] B. Song, R. Yang, N. Xi, K. C. Patterson, C. Qu, and K. W. C. Lai, "Cellular-level surgery using nano robots," *Journal of Laboratory Automation*, vol. 17, no. 6, pp. 425–434, 2012.

[70] B. Song, J. Zhao, N. Xi, H. Chen, K. W. C. Lai, R. Yang, and L. Chen, "Compressive feedback-based motion control for nanomanipulation:theory and applications," *Robotics, IEEE Transactions on*, vol. 30, no. 1, pp. 103–114, Feb 2014.

[71] N. Xi, B. Song, R. Yang, K. W. C. Lai, H. Chen, C. Qu, and L. Chen, "Video rate atomic force microscopy: Use of compressive scanning for nanoscale video imaging," *Nanotechnology Magazine, IEEE*, vol. 7, no. 1, pp. 4–8, March 2013.

[72] K. Igarashi, T. Uchihashi, A. Koivula, M. Wada, S. Kimura, T. Okamoto, M. Penttilä, T. Ando, and M. Samejima, "Traffic jams reduce hydrolytic efficiency of cellulase on cellulose surface," *Science*, vol. 333, no. 6047, pp. 1279–1282, 2011.

[73] L. R. Lynd, M. S. Laser, D. Bransby, B. E. Dale, B. Davison, R. Hamilton, M. Himmel, M. Keller, J. D. McMillan, J. Sheehan *et al.*, "How biotech can transform biofuels." *Nature biotechnology*, vol. 26, no. 2, 2008.

[74] M. E. Himmel, S.-Y. Ding, D. K. Johnson, W. S. Adney, M. R. Nimlos, J. W. Brady, and T. D. Foust, "Biomass recalcitrance: engineering plants and enzymes for biofuels production," *science*, vol. 315, no. 5813, pp. 804–807, 2007.

[75] V. Arantes, J. N. Saddler *et al.*, "Access to cellulose limits the efficiency of enzymatic hydrolysis: the role of amorphogenesis," *Biotechnol Biofuels*, vol. 3, no. 4, 2010.

[76] B. D. Solomon, J. R. Barnes, and K. E. Halvorsen, "Grain and cellulosic ethanol: History, economics, and energy policy," *Biomass and Bioenergy*, vol. 31, no. 6, pp. 416–425, 2007.

[77] R. Wolfenden and Y. Yuan, "Rates of spontaneous cleavage of glucose, fructose, sucrose, and trehalose in water, and the catalytic proficiencies of invertase and trehalas," *Journal of the American Chemical Society*, vol. 130, no. 24, pp. 7548–7549, 2008.

[78] P. Bubner, J. Dohr, H. Plank, C. Mayrhofer, and B. Nidetzky, "Cellulases dig deep in situ observation of the mesoscopic structural dynamics of enzymatic cellulose degradation," *Journal of Biological Chemistry*, vol. 287, no. 4, pp. 2759–2765, 2012.

[79] S.-Y. Ding, Q. Xu, M. Crowley, Y. Zeng, M. Nimlos, R. Lamed, E. A. Bayer, and M. E. Himmel, "A biophysical perspective on the cellulosome: new opportunities for biomass conversion," *Current Opinion in Biotechnology*, vol. 19, no. 3, pp. 218–227, 2008.

[80] J. Wang, A. Quirk, J. Lipkowski, J. R. Dutcher, C. Hill, A. Mark, and A. J. Clarke, "Real-time observation of the swelling and hydrolysis of a single crystalline cellulose fiber catalyzed by cellulase 7b from trichoderma reesei," *Langmuir*, vol. 28, no. 25, pp. 9664–9672, 2012.

[81] B. Song, N. Xi, R. Yang, K. W. C. Lai, and C. Qu, "Video rate atomic force microscopy (afm) imaging using compressive sensing," in *Nanotechnology (IEEE-NANO), 2011 11th IEEE Conference on.* IEEE, 2011, pp. 1056–1059.

[82] K. Igarashi, A. Koivula, M. Wada, S. Kimura, M. Penttilä, and M. Samejima, "High speed atomic force microscopy visualizes processive movement of trichoderma reesei cellobiohydrolase i on crystalline cellulose," *Journal of biological chemistry*, vol. 284, no. 52, pp. 36 186–36 190, 2009.

[83] A. Nakamura, H. Watanabe, T. Ishida, T. Uchihashi, M. Wada, T. Ando, K. Igarashi, and M. Samejima, "Trade-off between processivity and hydrolytic velocity of cellobiohydrolases at the surface of crystalline cellulose," *Journal of the American Chemical Society*, vol. 136, no. 12, pp. 4584–4592, 2014.

[84] T. T. Teeri, "Crystalline cellulose degradation: new insight into the function of cellobiohydrolases," *Trends in Biotechnology*, vol. 15, no. 5, pp. 160–167, 1997.

[85] B. K. Barr, Y.-L. Hsieh, B. Ganem, and D. B. Wilson, "Identification of two functionally different classes of exocellulases," *Biochemistry*, vol. 35, no. 2, pp. 586–592, 1996.

[86] C. Divne, J. Stahlberg, T. Reinikainen, L. Ruohonen, G. Pettersson, J. Knowles, T. T. Teeri, and T. A. Jones, "The three-dimensional crystal structure of the catalytic core of cellobiohydrolase i from trichoderma reesei," *Science*, vol. 265, no. 5171, pp. 524–528, 1994.

[87] K. Kipper, P. Väljamäe, and G. Johansson, "Processive action of cellobiohydrolase cel7a from trichoderma reesei is revealed as a," *Biochemical Journal*, vol. 385, pp. 1–9, 2005.

[88] S. Ahola, X. Turon, M. Osterberg, J. Laine, and O. Rojas, "Enzymatic hydrolysis of native cellulose nanofibrils and other cellulose model films: effect of surface structure," *Langmuir*, vol. 24, no. 20, pp. 11 592–11 599, 2008.

[89] S. Ahola, J. Salmi, L.-S. Johansson, J. Laine, and M. Österberg, "Model films from native cellulose nanofibrils. preparation, swelling, and surface interactions," *Biomacromolecules*, vol. 9, no. 4, pp. 1273–1282, 2008.

[90] Y.-S. Liu, J. O. Baker, Y. Zeng, M. E. Himmel, T. Haas, and S.-Y. Ding, "Cellobiohydrolase hydrolyzes crystalline cellulose on hydrophobic faces," *Journal of Biological Chemistry*, vol. 286, no. 13, pp. 11 195–11 201, 2011.

[91] N. Sugimoto, K. Igarashi, M. Wada, and M. Samejima, "Adsorption characteristics of fungal family 1 cellulose-binding domain from trichoderma reesei cellobiohydrolase i on crystalline cellulose: Negative cooperative adsorption via a steric exclusion effect," *Langmuir*, vol. 28, no. 40, pp. 14 323–14 329, 2012.

[92] J. Lehtiö, J. Sugiyama, M. Gustavsson, L. Fransson, M. Linder, and T. T. Teeri, "The binding specificity and affinity determinants of family 1 and family 3 cellulose binding modules," *Proceedings of the National Academy of Sciences*, vol. 100, no. 2, pp. 484–489, 2003.

[93] J. Jung, A. Sethi, T. Gaiotto, J. J. Han, T. Jeoh, S. Gnanakaran, and P. M. Goodwin, "Binding and movement of individual cel7a cellobiohydrolases on crystalline cellulose surfaces revealed by single-molecule fluorescence imaging," *Journal of Biological Chemistry*, vol. 288, no. 33, pp. 24 164–24 172, 2013.

[94] C. Mulakala and P. J. Reilly, "Hypocrea jecorina (trichoderma reesei) cel7a as a molecular machine: A docking study," *Proteins: Structure, Function, and Bioinformatics*, vol. 60, no. 4, pp. 598–605, 2005.

[95] A. Quirk, J. Lipkowski, C. Vandenende, D. Cockburn, A. J. Clarke, J. R. Dutcher, and S. G. Roscoe, "Direct visualization of the enzymatic digestion of a single fiber of native cellulose in an aqueous environment by atomic force microscopy," *Langmuir*, vol. 26, no. 7, pp. 5007–5013, 2010.

[96] S. Pérez and K. Mazeau, "Conformations, structures, and morphologies of celluloses," *Polysaccharides: Structural diversity and functional versatility*, vol. 2, 2004.

[97] T. Eriksson, J. Karlsson, and F. Tjerneld, "A model explaining declining rate in hydrolysis of lignocellulose substrates with cellobiohydrolase i (cel7a) and endoglucanase i (cel7b) of trichoderma reesei," *Applied biochemistry and biotechnology*, vol. 101, no. 1, pp. 41–60, 2002.

[98] J. Jalak and P. Väljamäe, "Mechanism of initial rapid rate retardation in cellobiohydrolase catalyzed cellulose hydrolysis," *Biotechnology and bioengineering*, vol. 106, no. 6, pp. 871–883, 2010.

[99] S. G. Allen, M. Tanchak, A. Quirk, A. N. Raegen, K. Reiter, R. Whitney, A. J. Clarke, J. Lipkowski, and J. R. Dutcher, "Surface plasmon resonance imaging of the enzymatic degradation of cellulose microfibrils," *Analytical Methods*, vol. 4, no. 10, pp. 3238–3245, 2012.

[100] A. V. Gusakov and A. P. Sinitsyn, "A theoretical analysis of cellulase product inhibition: Effect of cellulase binding constant, enzyme/substrate ratio, and β-glucosidase activity on the inhibition pattern," *Biotechnology and bioengineering*, vol. 40, no. 6, pp. 663–671, 1992.

[101] A. O. Converse, R. Matsuno, M. Tanaka, and M. Taniguchi, "A model of enzyme adsorption and hydrolysis of microcrystalline cellulose with slow deactivation of the adsorbed enzyme," *Biotechnology and Bioengineering*, vol. 32, no. 1, pp. 38–45, 1988.

[102] F. Xu and H. Ding, "A new kinetic model for heterogeneous (or spatially confined) enzymatic catalysis: contributions from the fractal and jamming (overcrowding) effects," *Applied Catalysis A: General*, vol. 317, no. 1, pp. 70–81, 2007.

[103] P. Väljamäe, V. Sild, A. Nutt, G. Pettersson, and G. Johansson, "Acid hydrolysis of bacterial cellulose reveals different modes of synergistic action between cellobiohydrolase i and endoglucanase i," *European Journal of Biochemistry*, vol. 266, no. 2, pp. 327–334, 1999.

[104] S. E. Levine, J. M. Fox, H. W. Blanch, and D. S. Clark, "A mechanistic model of the enzymatic hydrolysis of cellulose," *Biotechnology and bioengineering*, vol. 107, no. 1, pp. 37–51, 2010.

[105] N. Cruys-Bagger, H. Tatsumi, K. Borch, and P. Westh, "A graphene screen-printed carbon electrode for real-time measurements of unoccupied active sites in a cellulase," *Analytical biochemistry*, 2014.

[106] H. Guo, A. Ma, G. Zhao, J. Yun, X. Liu, H. Zhang, and G. Zhuang, "Effect of farnesol on penicillium decumbenss morphology and cellulase production," *BioResources*, vol. 6, no. 3, pp. 3252–3259, 2011.

[107] M. Linder and T. T. Teeri, "The cellulose-binding domain of the major cellobiohydrolase of trichoderma reesei exhibits true reversibility and a high exchange rate on crystalline cellulose," *Proceedings of the National Academy of Sciences*, vol. 93, no. 22, pp. 12 251–12 255, 1996.

[108] H. Palonen, M. Tenkanen, and M. Linder, "Dynamic interaction of trichoderma reesei cellobiohydrolases cel6a and cel7a and cellulose at equilibrium and during hydrolysis," *Applied and environmental microbiology*, vol. 65, no. 12, pp. 5229–5233, 1999.

[109] A. Ma, Q. Hu, Y. Qu, Z. Bai, W. Liu, and G. Zhuang, "The enzymatic hydrolysis rate of cellulose decreases with irreversible adsorption of cellobiohydrolase i," *Enzyme and Microbial Technology*, vol. 42, no. 7, pp. 543–547, 2008.

[110] A. Kyriacou, R. J. Neufeld, and C. R. MacKenzie, "Reversibility and competition in the adsorption of trichoderma reesei cellulase components," *Biotechnology and bioengineering*, vol. 33, no. 5, pp. 631–637, 1989.

[111] W. Sattler, H. Esterbauer, O. Glatter, and W. Steiner, "The effect of enzyme concentration on the rate of the hydrolysis of cellulose," *Biotechnology and bioengineering*, vol. 33, no. 10, pp. 1221–1234, 1989.

[112] Z. Yao, C. L. Kane, and C. Dekker, "High-field electrical transport in single-wall carbon nanotubes," *Physical Review Letters*, vol. 84, no. 13, p. 2941, 2000.

[113] D. Yang, S. Wang, Q. Zhang, P. Sellin, and G. Chen, "Thermal and electrical transport in multi-walled carbon nanotubes," *Physics Letters A*, vol. 329, no. 3, pp. 207–213, 2004.

[114] Y.-H. Lee, J.-H. Lee, S. Chung, S. Lee, and B. Ju, "Carrier carrying capacity of one-step grown suspended carbon nanotube bridge with carbon nanotube contact electrodes: For practical one-dimensional electronics," *Applied physics letters*, vol. 89, no. 7, p. 073109, 2006.

[115] S. J. Tans, A. R. Verschueren, and C. Dekker, "Room-temperature transistor based on a single carbon nanotube," *Nature*, vol. 393, no. 6680, pp. 49–52, 1998.

[116] M.-S. Wang, D. Golberg, and Y. Bando, "Interface dynamic behavior between a carbon nanotube and metal electrode," *Advanced Materials*, vol. 22, no. 1, pp. 93–98, 2010.

[117] S. Hong and S. Myung, "A flexible approach to mobility," *Nature Nanotech*, vol. 2, pp. 207–208, 2007.

[118] P. Kim, L. Shi, A. Majumdar, and P. McEuen, "Thermal transport measurements of individual multiwalled nanotubes," *Physical review letters*, vol. 87, no. 21, p. 215502, 2001.

[119] C. Santini, P. Vereecken, A. Volodin, G. Groeseneken, S. De Gendt, and C. Van Haesendonck, "A study of joule heating-induced breakdown of carbon nanotube interconnects," *Nanotechnology*, vol. 22, no. 39, p. 395202, 2011.

[120] K. Mølhave, S. B. Gudnason, A. T. Pedersen, C. H. Clausen, A. Horsewell, and P. Bøggild, "Transmission electron microscopy study of individual carbon nanotube breakdown caused by joule heating in air," *Nano letters*, vol. 6, no. 8, pp. 1663–1668, 2006.

[121] M. Tsutsui, Y.-k. Taninouchi, S. Kurokawa, and A. Sakai, "Electrical breakdown of short multiwalled carbon nanotubes," *Journal of applied physics*, vol. 100, no. 9, p. 094302, 2006.

[122] A. Javey, J. Guo, M. Paulsson, Q. Wang, D. Mann, M. Lundstrom, and H. Dai, "High-field quasiballistic transport in short carbon nanotubes," *Physical Review Letters*, vol. 92, no. 10, p. 106804, 2004.

[123] Y. Wei, K. Jiang, L. Liu, Z. Chen, and S. Fan, "Vacuum-breakdown-induced needle-shaped ends of multiwalled carbon nanotube yarns and their field emission applications," *Nano Letters*, vol. 7, no. 12, pp. 3792–3797, 2007.

[124] J. Huang, S. Chen, S. Jo, Z. Wang, D. Han, G. Chen, M. Dresselhaus, and Z. Ren, "Atomic-scale imaging of wall-by-wall breakdown and concurrent transport measurements in multiwall carbon nanotubes," *Physical review letters*, vol. 94, no. 23, p. 236802, 2005.

[125] G. K. Goswami and K. K. Nanda, "Electrical breakdown of carbon nanotube devices and the predictability of breakdown position," *AIP Advances*, vol. 2, no. 2, p. 022129, 2012.

[126] J. P. Aubin, *Mutational and Morphological Analysis: Tools for Shape Evolution and Morphogenesis*. Birkhäuser, 1998.

[127] T. Lorenz, "A viability theorem for morphological inclusions," *SIAM J. Control Optim.*, vol. 47, no. 3, pp. 1591–1614, 2008.

[128] ——, "Morphological control problems with state constraints," *SIAM J. Control Optim.*, vol. 48, no. 8, pp. 5510–5546, 2010.

[129] ——, "Set-valued maps for image segmentation," *Comput Visual Sci*, vol. 4, no. 1, pp. 41–57, 2001.

[130] L. Doyen, "Mutational equations for shapes and vision-based control," *Journal of Mathematical Imaging and Vision*, vol. 5, no. 2, pp. 99–109, 1995.

[131] A. Goradia, N. Xi, Z. Cen, and M. W. Mutka, "Modeling and design of mobile surveillance networks using a mutational analysis approach," in *Proc. IEEE/RSJ Int. Conf. Intell. Robots Syst.*, Alberta, Canada, 2005, pp. 3003–3008.

[132] E. Marchand and F. Chaumette, "Feature tracking for visual servoing purposes," *Robot. Auton. Syst.*, vol. 52, no. 1, pp. 53–70, 2005.

[133] L. Doyen, "Mutational equations for shapes and vision-based control," *Journal of Mathematical Imaging and Vision*, vol. 5, no. 2, pp. 99–109, 1995.

[134] J. Zhao, B. Song, N. Xi, and K. W. C. Lai, "Mutation analysis models for visual servoing in nanomanipulations," in *Proc. IEEE Int. Conf. Control Decision*, Orlando, Florida, USA, 2011, p. To Appear.

[135] C. Collewet, E. Marchand, and F. Chaumette, "Visual servoing set free from image processing," in *Proc. IEEE Int. Conf. Robot. Autom.*, Pasadena, CA, USA, 2008, pp. 81–86.

[136] A. Dame and E. Marchand, "Improving mutual information-based visual servoing," in *Proc. IEEE Int. Conf. Robot. Autom.*, Anchorage, Alaska, USA, 2010, pp. 5531–5536.

[137] J. L. Barron, D. J. Fleet, and S. S. Beauchemin, "Performance of optical-flow techniques," *International Journal of Computer Vision*, vol. 12, no. 1, pp. 43–77, 1994.

[138] W. Rudin, *Principles of Mathematical Analysis, Third Edition.* New York City, U.S: McGraw-Hill Science/Engineering/Math, 1976.

[139] C. Hegde and R. G. Baraniuk, "Sampling and recovery of pulse streams," *IEEE Transactions on Signal Processing*, vol. 59, no. 4, pp. 1505–1517, 2010.

[140] E. J. Candes and J. Romberg., "Sparsity and incoherence in compressive sampling," *Inverse Problems*, vol. 23, no. 3, pp. 969–985, 2007.

[141] J. Zhao, N. Xi, L. Sun, and B. Song, "Stability analysis of non-vector space control via compressive feedbacks," in *2012 IEEE 51st Annual Conference on Decision and Control (CDC).* IEEE, 2012, pp. 5685–5690.

[142] H. Chen, N. Xi, K. Lai, C. Fung, and R. Yang, "Development of infrared detectors using single carbon-nanotube-based field-effect transistors," *Nanotechnology, IEEE Transactions on*, vol. 9, no. 5, pp. 582–589, 2010.

[143] K. W. C. Lai, N. Xi, C. K. M. Fung, jiangbo Zhang, H. Chen, Y. Luo, and U. C.Wejinya, "Automated nanomanufacturing system to assemble carbon nanotube based devices," *International Journal of Robotics Research*, vol. 28, no. 4, pp. 523–536, 2009.

[144] M. A. Kuroda, A. Cangellaris, and J.-P. Leburton, "Nonlinear transport and heat dissipation in metallic carbon nanotubes," *Phys. Rev. Lett.*, vol. 95, p. 266803, Dec 2005.

[145] M. Suzuki, Y. Ominami, Q. Ngo, C. Y. Yang, A. M. Cassell, and J. Li, "Current-induced breakdown of carbon nanofibers," *Journal of Applied Physics*, vol. 101, no. 11, pp. 173 110–173 110, 2007.